Representation of African Easterly Waves and associated rainfall in two versions of ECMWF Integrated Forecasting System

Master's Thesis in
Meteorology and Climate Physics
by

Chun Cheong Nicolas Lo

March 2024

Advisor: Prof. Dr. Andreas H. Fink
Co-advisor: Prof. Dr. Peter Knippertz

Abstract

This project aims at investigating the representation of African Easterly Waves (AEWs) and associated rainfall in two versions of ECMWF Integrated Forecasting System (IFS). It has been observed that there is a coupling between AEW and precipitation over the tropical Africa and Atlantic (Duvel, 1990; Gu et al., 2004). There is a certain extent of Squall Lines (SL) or Mesoscale Convective Systems (MCS) found being AEW-driven (Fink and Reiner, 2003). The location of the convective activities matters to the growth of AEW throughout its lifetime, which propagates westward from the African continent to the Atlantic. Tropical rainfall is known to have a low persistence (Roehrig et al., 2013), while synoptic wave disturbances have a better predictability thanks to a better known wavelength and period. The development of AEW depends on the upstream trigger and barotropic-baroclinic growth from African Easterly Jet (AEJ) (Berry and Thorncroft, 2005).

In view of the recent development of the ECMWF IFS, the moist physics upgrade to IFS Cycle 47r3 since October 2021 is suggested to improve subgrid-scale parameterization and better coupled deep convection to the dynamics (Bechtold et al., 2020). This thesis is constructed to analyze the changes of the ECMWF IFS in representing the coupling between AEW and rainfall between the summer seasons of 2021 and 2022.

The wave trough (WT) dataset which is used to represent AEW, is identified and tracked based on the method by Belanger et al. (2016) with slight modifications. A composite analysis has been performed to investigate the distributive curves of the precipitation rate field from ECMWF IFS along the relative longitude from the AEW trough axes derived from ERA5 reanalysis wind field. To compare such a performance, the satellite-derived rainfall product GPM-IMERG was also used. This analysis has always been used to meteorological parameters from ECMWF IFS related to the moisture fields and the dynamics.

It is observed that there is an improvement in simulating the precipitation field with respect to WT axis in 2022 starting from the initial condition. The result agrees well with the AEW dynamics that occur during different phases depicted by previous studies (Kiladis et al., 2006; Cornforth et al., 2017). Precipitation over land WT is usually located ahead of WT axis which would aid WT propagation westward, while precipitation over ocean WT is usually located close to the WT axis, which would increase its intensity (Duvel, 1990; Berry and Thorncroft, 2005). From the result, stronger WT category is linked to stronger modulations to precipitation and other meteorological parameters that depict its environmental conditions. This coupling pattern between precipitation and WT from the composite is no longer observed at the lead time interface between 3 to 4 days. The result has showed that there is a remarkable change in moisture convergence and organization of AEW between the two years, which the revision of moist physics is believed to be the main driver for these observable changes. Future study can be further extended towards the predictability of AEW-precipitation phase relationship based on the possibly identified WT features in both deterministic and probabilistic forecast datasets.

Contents

1 Introduction

The tropical West Africa is inhabited with a large population and their livelihood highly depends on the weather conditions. The climatic patterns influence the region closely, including the aspects of agriculture, energy production and infrastructure. It is known that the tropical West Africa has a large climatic variability on precipitation patterns which could be attributed to the various temporal-scale and spatial-scale wave patterns (Schlueter et al., 2019). In such case, there is a high difficulty to witness any persistence in the underlying weather patterns over the region (Roehrig et al., 2013) and thus doing a prediction of it has been a great challenge.

One of the approaches is to observe the relevant synoptic-scale forcings towards the regional weather, while one of the prominent forcings is namely the African Easterly Waves (AEWs). AEW is associated with the baroclinically-formed African Easterly Jet (AEJ) (Parker et al., 2005). These patterns are pronounced during the West African summer monsoon season. Since AEW is known to have a certain extent of practical predictability due to its known characteristics, it could aid to explain a certain extent of variance in the regional weather behaviours such as precipitation and other environmental conditions (Davis et al., 2013).

To assist in AEW identification and tracking, a proposed algorithm by (Belanger et al., 2016) has focused on locating and tracking the easterly wave trough, by analyzing the advection of curvature vorticity anomaly which is derived from horizontal winds, and identifying regions where it is equal to 0 s^{-2}.

Previous research has suggested that the development of AEW is linked to barotropic and baroclinic energy conversion with an initially convective upstream triggers (Berry and Thorncroft, 2005; Thorncroft and Hoskins, 1994). It has been found that there is a coupling relationship between the AEW activities and the rainfall patterns over tropical Africa and this area is well known for a vigorous growth and dominance of mesoscale convective systems (MCS) (Maranan et al., 2018). Over tropical Africa, MCS are very active and they mostly propagate in the direction with AEJ and AEW. It might be difficult to observe the direct connection between AEW troughs and these convective systems but they vary across different locations and life stages.

In view of the latest development on the ensemble prediction system (EPS) of numerical weather prediction (NWP) models in the European Centre for Medium-range Weather Forecast (ECMWF), the recent moist physics upgrade to the latest cycle IFS Cycle 47r3, is suggested to bring significant improvements to the parameterization of clouds, convection, turbulent mixing, and microphysics (Bechtold et al., 2020). This enhancement would lead to a better representation of the structure and

organization of storms. A notable addition is the new term, namely the total advective moisture tendency, which is added into the mass flux closure, so as to enhance the coupling of convective parameterization to the dynamics, particularly vital in high-resolution simulations. The inclusion of this term results in smaller and more realistic rain areas, aligning closely with the observed probability distribution function (PDF) of precipitation rates. Despite the improvements, scale-aware parametrization remains crucial as it outperforms explicitly resolving everything with a 5km resolution model. The upgrade is expected to enhance the organization of moisture convergence.

Regarding predictability, the moisture field remains poorly constrained, making rainfall prediction challenging, especially in tropical West Africa (Vogel et al., 2018). However, there is some predictability associated with African Easterly Waves (AEW) due to the well-defined vorticity pattern. The moist physics improvement is anticipated to enhance the AEW prediction. In addition, the ECMWF ensemble forecast helps in obtaining the average structure of rainfall, although rainfall itself is not assimilated into the model.

This project utilizes the ECMWF ensemble forecast datasets, namely AEW trough data with a tracking algorithm similar to Belanger et al. (2016) and precipitation. The goal is to investigate the predictability of AEW and associated rainfall after the moist physics upgrade. To proceed to the investigation, the precipitation is aligned to the wave trough of AEW and observe any difference in the pattern between 2021 and 2022.

This project intends to study how the representation of AEW and associated rainfall changes after the moist physics upgrade. Through utilizing AEW trough and vortex datasets as to represent AEW-related dynamic features, a composite analysis has been performed to evaluate the interaction between these dynamic features and precipitation field. This project is designed to investigate changes in the coupling of AEW and precipitation field, by inspecting any remarkable patterns through the magnitude, structure and organization of AEW.

In Chapter 2, in relation to the previous studies, further description on the current state of research will be illustrated. Chapter 3 will provide a research statement, highlighting the research questions of this thesis. Followed by Chapter 4, the datasets and methodology adopted in this project will be presented. Chapter 5 presents the result of the study. Chapter 6 provides interpretation of the results and discuss the findings in relation to the research questions. Subsequently, it concludes the whole thesis and some future directions will be suggested.

2 Literature Review

Tropical wave activities, in specific African Easterly Waves (AEW), are one of the most researched areas for the purpose of evaluating tropical African climatic variability, given their pivotal role in modulating the regional synoptic patterns. In this chapter, fundamental concepts and the current state of research in this topic will be elaborated and this section aims at serving as the theoretical background for discussion in later sections.

2.1 West African Monsoon

The West African Monsoon (WAM) is characterized by a seasonal shift to certain areas of the continent in their prevailing wind directions, from northeasterly winds in winter to southwesterly winds in summer. This annual transition significantly impacts weather patterns, ecosystems, and livelihoods in the region (Fink et al., 2017). It is driven by the thermodynamic differences between the hot and dry conditions in the Sahara Desert at the north and the cool and moist Atlantic Ocean at the south and west from the African continent. This leads to a surface pressure gradient between these two distinctive air masses. WAM plays a key role in shaping the precipitation patterns and climate in tropical Africa. For instance, during summer, the southwest monsoon brings moisture inland from the Atlantic Ocean across the Guinea Coast, resulting in precipitation across the continent. African Easterly Waves (AEWs) are one of the notable features observed during this season which will be discussed more detailedly in the later sections. The following displays the map of West Africa (Figure 2.1)

The movement of the surface convergence of trade winds shifts accordingly with the annual oscillation of the Sun between the two hemispheres, creating distinct wet and dry seasons over tropical Africa, between latitudes 9° to 20°N (Fink et al., 2017). A Hovmöller diagram (Figure 2.2) demonstrates the northward migration of maximum precipitation zone in the summer months, which is caused by the moisture transport from the West African summer monsoon. Especially during July to September, the Soudano-Sahelian zone is therefore observed with a considerable amount of rainfall.

In contrast to oceanic regions of the Intertropical Convergence Zone (ITCZ) which yield a band of precipitating clouds along the tropics, the region where opposing wind direction from the hemispheres meeting over the African continent, namely area of confluence, does not directly yield maximum rainfall, due to dry northern air and subsidence aloft, making the ITCZ term somewhat ambiguous to use in the description over tropical Africa (Nicholson, 2018).
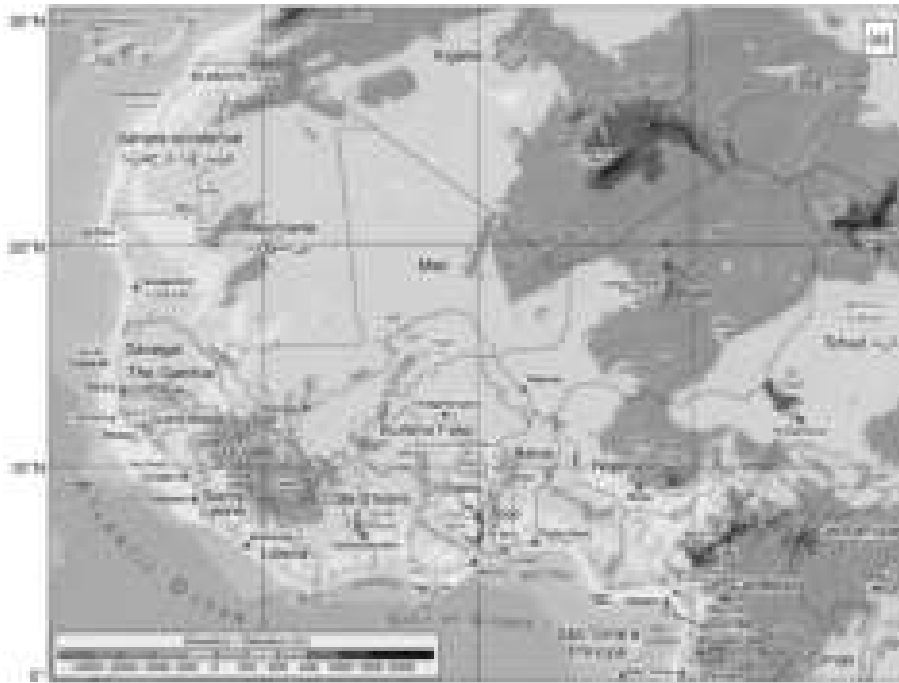
Figure 2.1: Map of West Africa (Fink et al., 2017).
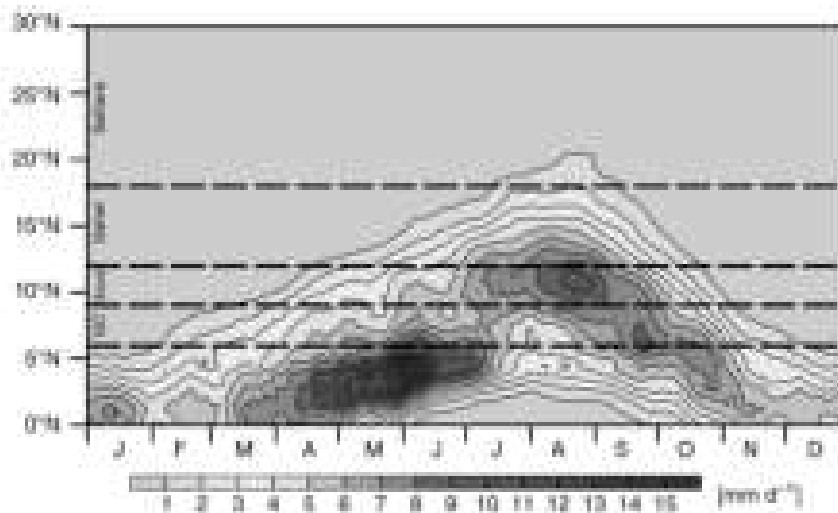
Figure 2.2: A Hovmöller diagram of the 15-day running mean of daily precipitation, averaged between 10°W and 10°E with the labelling of four climatic zones at their respective latitude bands: Guinea Coast (GC), Soudanian (Soud), Sahel and Sahara, based on the computation from TRMM 3B42 Version 7 in the period 1998–2012 (Fink et al., 2017).

During the summer months, the Sahara Desert warms more rapidly due to strong surface heating than the cooler, damp air originated from the eastern tropical Atlantic Ocean, resulting in the formation of a region of low pressure, surface-based, warm cored known as the Saharan Heat Low (SHL) or West African Heat Low (WAHL), and this is usually found over northern Mali (Fig. 2.3). On the contrary, in the southern part, the relatively cooler and moister air from the Atlantic Ocean establishes a high-pressure system. These variations in atmospheric pressure generate pressure gradients that drive the southwest monsoonal winds towards the coast.

Figure 2.3: Schematic illustration of the atmospheric and oceanic features of West Africa in July (Fink et al., 2017). Shown are the positions of the ITD, the monsoon trough, upper-level air streams (AEJ, TEJ/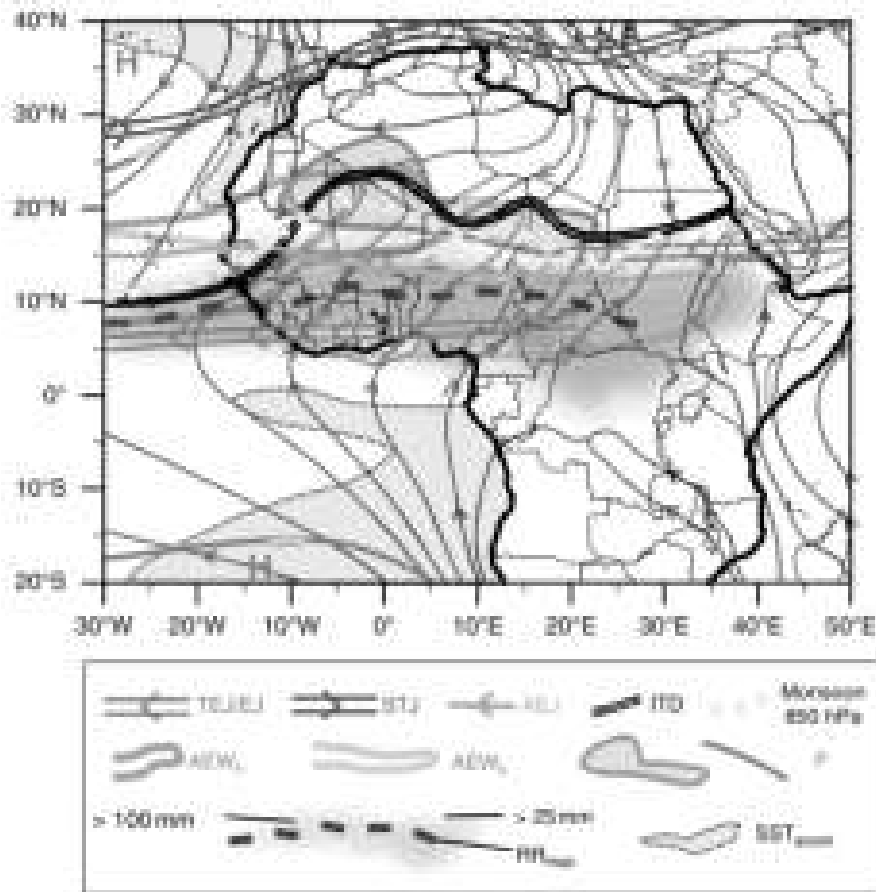EJ (Easterly Jet) and STJ), surface winds coloured according to the 2 m air temperature (see colour bar), the tropical rain belt with the maximum axes of rainfall (RRmax), northerly and southerly AEW-associated vortices propagation zones (AEWn and AEWs respectively), areas with relatively cold SSTs (SSTanom) and example pressure lines marking the Azores ('H'), Libyan ('h') and Saint Helena ('H') highs and the heat low ('L') (Fink et al., 2017).

This dichotomy sets the stage for the "four weather concepts zones" as shown in the schematics of the meridional cross-section of West African monsoon system in July (Fink et al., 2017), namely Zone A-D, spanning from the dry Sahara to the moist Atlantic ocean Fig. 2.4). This figure has illustrated probable vertical circulation patterns within these latitudinal bands. The Intertropical Discontinuity (ITD) signifies the boundary between these air masses and is marked by the northernmost reach of moist monsoonal air around 20°N.

Zone A, the northern part of the continent, where the Sahara desert is located, experiences hot, dry, and dusty conditions with a deep boundary layer. It has a high surface albedo which leads to strong radiative loss to space. SHL is situated over land and primarily confined to the lower troposphere below approximately 600 hPa. With a limited amount of moisture in the desert region, precipitation is rare and the dew-point temperature is low which forms the Saharan Air Layer (SAL).

On the other hand, at the southern part over the ocean, coastal upwelling from the Gulf of Guinea driven by Ekman transport, results in relatively cooler sea surface temperature. This is named as the
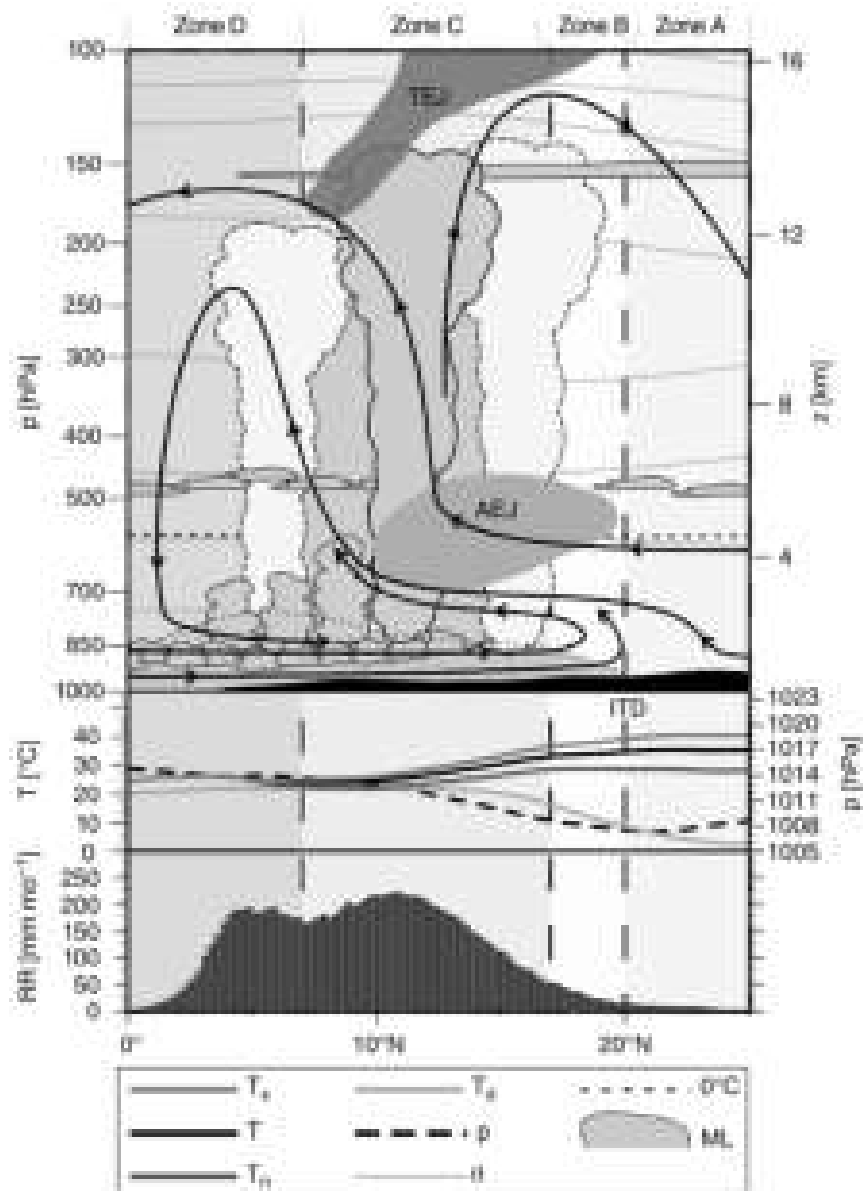
Figure 2.4: Schematic cross-section of the atmosphere between 10°W and 10°E in July and illustration of the weather zones A–D of the West African monsoon system. This uppermost subfigure highlights the ITD position, African Easterly Jet (AEJ) at mid-tropospheric level, Tropical Easterly Jet (TEJ) at upper level, the monsoon layer (ML) (as defined by westerly, i.e. positive, zonal winds), streamlines, clouds, the freezing level (0°C isotherm as dooted line). The middle subfigure displays isentropes (θ), minimum (T_n), maximum (T_x) and mean (T) and dew point temperatures (T_d), atmospheric pressures (p). The lowest subfigure draws the mean monthly rainfall totals over this latitudinal band(RR) (Fink et al., 2017).

Atlantic equatorial cold tongue region where the stability of marine atmospheric BL is increased (Fink et al., 2017). This phenomenon has been observed in the parts of the Ivorian Gulf and along the Coast of Ghana. This region, as represented by Zone D, has a deep monsoon layer but infrequent deep convection. Shallow stratus or mid-level altostratus clouds are mostly found.

The sharp contrast between these air masses creates surface baroclinicity and is marked by the In-tertropical Discontinuity (ITD). ITD indicates the northernmost penetration of the moist monsoonal air onto the continent, roughly at 20N. Zone A and Zone B are distinguished by the position of this air-mass boundary, which separates the hot and dry northerly surface flow, i.e. the Saharan Air Layer (SAL), and the moist and cool southwesterly monsoon flow from the south. At the south of ITD, Zone B being this narrow band, experiences shallow moist southwesterly winds and only short-lived thunderstorms would take place in this area.

While over Zone C, maximum convergence and precipitation are found. The shallow moist monsoon layer is overlaid by the northeasterly trade wind. Deep convection is expected over this area. The SAL from the north and the cooler monsoon air at the south have different moisture content which follow different lapse rates. The surface baroclinicity leads to an increase in geostrophic wind with height, which is defined as thermal wind balance. A narrow band of strong zonal easterly wind, at the latitude of 15°N, with the speed about 15 ms^{-1}, is found at 600-700hPa, namely the African Easterly Jet (AEJ), situated between Zone B and Zone C. There is a gradient reversal of wind above the jet level, from low-level southwesterlies change to mid-level easterlies. This climatic pattern is found in the summer months owing to the convergence of the two air masses from opposite direction by summer monsoon, while as in the winter months, only Zone A and B could be found (Cornforth et al., 2017).

Furthermore, in terms of thermodynamic profiles, the monsoon layer at the south is a humid zone bounded to the land surface which extends northwards into the Sahel such that the depth decreases from south to north (Parker et al., 2005). Air parcels at this layer are lifted pseudo-adiabatically which leads to strong surface fluxes and deep moist convection in this zone. The monsoon layer is modulated strongly by diurnal circulation over the land surface. Meanwhile the SAL over the continent follows a thermodynamic profile close to a dry adiabat with low static stability and potential vorticity (PV) because of higher boundary-layer potential temperature. This lead to a large-scale north-south meridional gradient in boundary-layer equivalent potential temperature θ_E. Dry adiabats and moist adiabats are expected to meet and cross at mid-levels and negative meridional gradients of θ_E take place at low levels. This creates a baroclinic environment in this region. As illustrated in Figure 2.5, the maximum of θ_E is found at the position of AEJ while decreases at the two flanks of AEJ. SAL overlaying the monsoon layer drives strong deep moist convection. Strong horizontal wind shear at the anticyclonic northern flank of the AEJ leads to a reversal in the poleward PV gradient at the AEJ level. This is associated to barotropic instability and contribute to the wave disturbances over this zone (Thorncroft and Hoskins, 1994).

West African Summer Monsoon is influenced by factors like local topography, mesoscale processes, and large-scale environments such as African Easterly Waves. In addition to the zonal-averaged latitude-time plot, within the east-west extent of tropical Africa, there is a remarkable rainfall variability between the central Africa and the southwest coast. Most of the inner regions experience only one rainy season given by the onset of the summer monsoon season (Fink et al., 2017). The monsoon flow transports warm, moist air from the Atlantic Ocean towards the continent, providing the necessary moisture and instability for the development of AEW and organized convective systems (OCS) (Mathon et al., 2002).
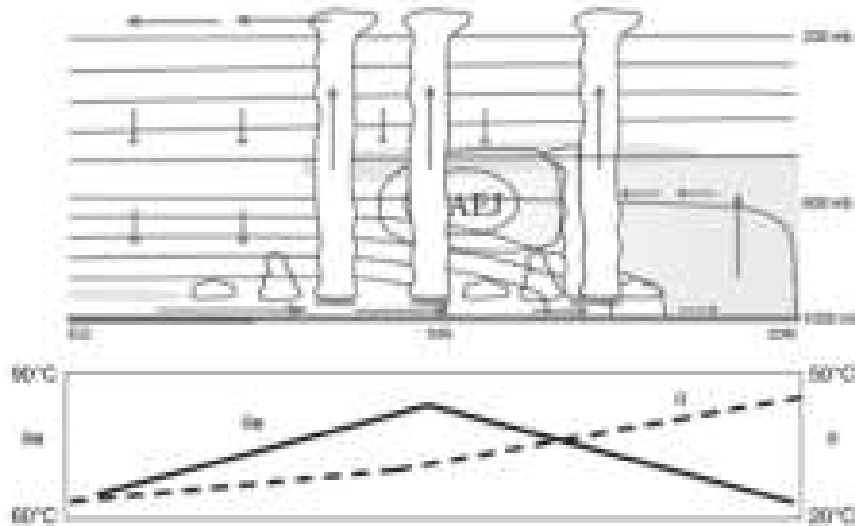
Figure 2.5: Schematic south–north vertical cross-section along the Greenwich Meridian, highlighting the SHL–AEJ–ITCZ system and SAL (shaded yellow), with meridional variations in atmospheric boundary-layer potential temperature θ (contoured in upper panel) and equivalent potential temperature θ_E. The monsoon trough is located just to the south of the AEJ (Parker et al., 2005; Cornforth et al., 2017).

Specifically over the Guinea coast, with reference to Fig. 2.2, there are two rainfall peaks observed which take place in May/June and October respectively each year (Fink et al., 2017). This could be attributed to the propagation of the overhead sun. The rainy season during early summer takes place when the ascending branch of the Hadley cell from an oceanic ITCZ over the equatorial Gulf of Guinea is approaching and strengthening. In July, SHL shifts northward and ascending branch of Hadley cell is weaker. Compared to the earlier month, less rainfall would occur over the region along the Guinea coast. As in October, as a consequence of the retreat of monsoon layer equatorward, more vertical motion takes place in the Guinea coast region again and leads to a second peak of rainfall. In this regard, bimodal seasonal rainfall distribution over the Guinea Coast is resulted.

As depicted in Figure 2.3, the Subtropical Jet (STJ) and AEJ are delineated along the Mediterranean Coast and the 15°N parallel, respectively, with distinctions between higher (100 hPa) and lower (200 hPa) TEJ components over different regions (Fink et al., 2017). AEW activity could be subdivided into northerly and southerly tracks at at 850hPa and 600hPa respectively (Fink and Reiner, 2003), converging over the Eastern Atlantic Ocean. Maximum rainfall occurs between 10–12°N, within the southerly AEW track region. Cumulonimbus cloud depths are the deepest in the AEJ region and relatively less deep in the southerly rainy zone. Low-level convergence and vertical motion take place in the vicinity from the ITD, with an equatorward return flow around 700 hPa contributing to deep ascent in the rainy zone.

2.2 Typical Rainfall Systems in Tropical Africa

2.2.1 Processes and factors governing convection

Convection is a widespread process as a result of an unstable vertical distribution of thermodynamic energy. The resulting circulation pattern aims at restoring the stable conditions by releasing excess moist energy gained from the heated surface and compensating for energy loss through radiative processes in the upper atmosphere. This phenomenon would advance to universally unstable conditions across tropical regions. The factors that govern convective activities include convective updraft, convective downdraft, vertical wind shear and external forcings. The following highlights the necessary conditions for the occurrence of these elements.

A Skew-T Log-P diagram is one of the commonly used thermodynamic diagrams in weather analysis and forecasting, which is a useful tool to represent the vertical temperature and moisture profiles. As shown in the Figure 2.6, convective updraft refers to the lifting of air parcels to their level of free convection (LFC) due to conditional instability. An air parcel rises when it is warmer than the environment. LFC indicates the point on the Skew-T Log-P diagram that the temperature profile of the air parcel and the ambient temperature profile intersects. The parcel is more buoyant than the surrounding and thus becomes instable.
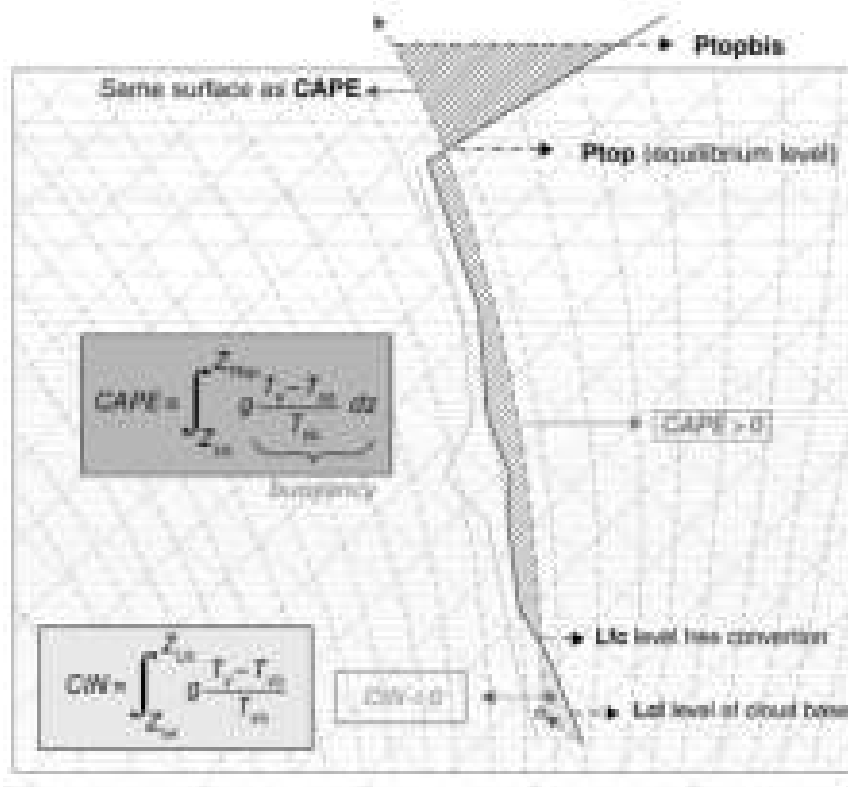

Figure 2.6: A Skew-T-log-p diagram demonstrating the parcel theory (Lafore et al., 2017).

When a parcel of air is lifted in the atmosphere, the parcel expands and cools at the dry adiabatic lapse rate, which assumes no condensation or evaporation of water vapor. As it reaches its dew

point temperature, it becomes saturated with water vapor, and condensation begins. At this point, the parcel follows the moist adiabatic lapse rate and cools at a slower rate. The point at which condensation occurs is known as the Lifting Condensation Level (LCL), which represents the cloud base. If the environmental lapse rate, which signifies the temperature change with height in the surrounding atmosphere, is steeper (with warmer air aloft) than the moist adiabatic lapse rate, the parcel becomes colder than the surrounding environment as it rises. This creates a stable atmosphere, which is referred as Convective Inhibition (CIN). This refers to energy barrier required to overcome for free convection, namely the Level of Free Convection (LFC).

Above the LFC, this saturated air parcel becomes warmer than its environment as it rises, making it less dense than the surrounding air. The parcel gains buoyancy and rises all up to the equilibrium level. Hence convective clouds and potentially thunderstorms develop. The difference between the potential energy of the parcel lifted from the surface to the LFC and that of the surrounding environment at the LFC is quantified as Convective Available Potential Energy (CAPE). The vertical integral of the buoyancy force can be related to the maximum updraft velocity $w_{max} \approx \frac{1}{2}\sqrt{CAPE}$. The following outlines the equations of the above quantities.

$$B = \frac{T_v - T_{v0}}{T_{v0}}$$
$$CAPE = \int_{LFC}^{EL} B dz$$
$$CIN = -\int_0^{LFC} B dz$$

B denotes the buoyancy force. EL denotes the equilibrium level; LFC denotes the Level of Free Convection. T_v denotes the virtual temperature, which is defined as the temperature that a dry air parcel has to be, compared to a moist air parcel under the same pressure and density.

Regarding the geographical context of tropical West Africa, the relatively low rate, at which dry air cools in the Saharan Air Layer (SAL), results in significant conditional instability (Lafore et al., 2017). The presence of a CIN barrier delays the initiation of convection, allowing for the accumulation of additional energy in the lower layers of the atmosphere below the clouds. The elevated temperature at the bottom of the SAL plays a crucial role in restricting the upward movement of air masses in monsoon layer, which could be quantified by CIN, while the colder upper regions of the SAL enhance CAPE for convective activity. As a result, it gives rise to the formation of more intense storms later in the day or even the next day. This could explain the reason why convective systems in tropical Africa are able to sustain overnight. From the above, updrafts require high CAPE and PW, but limited by CIN. A higher CAPE value indicates a greater potential for strong convection and thunderstorm development.

Another key element governing the convective activities is convective downdraft. As discussed in the previous section, in order to maintain mass conservation, convective updraft has to be compensated

by certain subsiding motions, i.e. convective downdrafts. These are caused by the cooling from the evaporation and sublimation processes, with a range of speed 1-15 ms^{-1}.

Convective downdraft is based on the assessment of Downdraught Convective Available Potential Energy (DCAPE), as proposed by Emanuel et al. (1994), which quantifies the upper bound for maximum downward acceleration. To dive in, as illustrated in Fig 2.7, given an air parcel at a certain pressure level where the vertical speed reaches its minimum, it gets saturated at constant pressure by evaporation of rain. This is then brought down pseudoadiabatically from z=h to the surface z=0 such that it remains saturated by rain evaporation. Parcels are cooled isobarically to its wet-bulb temperature. The energy released by this process is DCAPE of the parcel. Such intense downdraught lead to extreme dying and stabilization above the boundary layer.
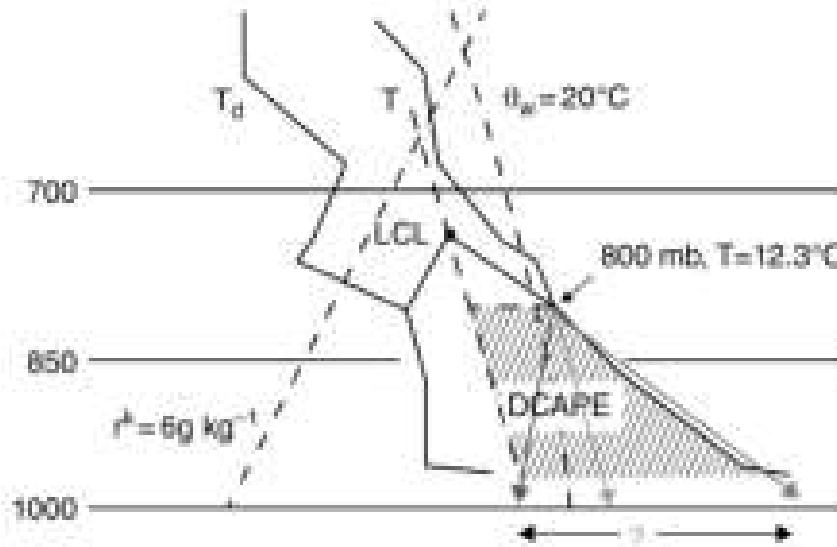

Figure 2.7: Illustration of the computation of the DCAPE index on a Skew-T Log-P diagram, for a subsiding parcel taken at 800 hPa. The blue arrow indicates the descent of air that reaches the ground completely saturated, the red arrow denotes dry adiabatic descent, and the green arrow represents the most common occurrence, lying between the moist and dry extremes. Therefore, there is considerable uncertainty in the temperature of the downdraught at ground level (Lafore et al., 2017).

$$DCAPE = g \int_h^0 \frac{T_v - T_{v0}}{T_{v0}} dz$$

As displayed in the schematics in Figure 2.8, intense downdrafts are notably pronounced when accompanied by elevated cloud bases, dry mid-tropospheric layers, and a well-mixed boundary layer over West Africa. The dry air layer allows strong downdraft motion. The spread of cold air at ground level takes place in the form of a density current, characterised by a rotor circulation. These cold pools give rise to exceptionally strong gusts along their leading edges and elevate the surrounding warm air, fueling further convective growth. This phenomenon is common to be observed in African squall lines (Fink and Reiner, 2003).
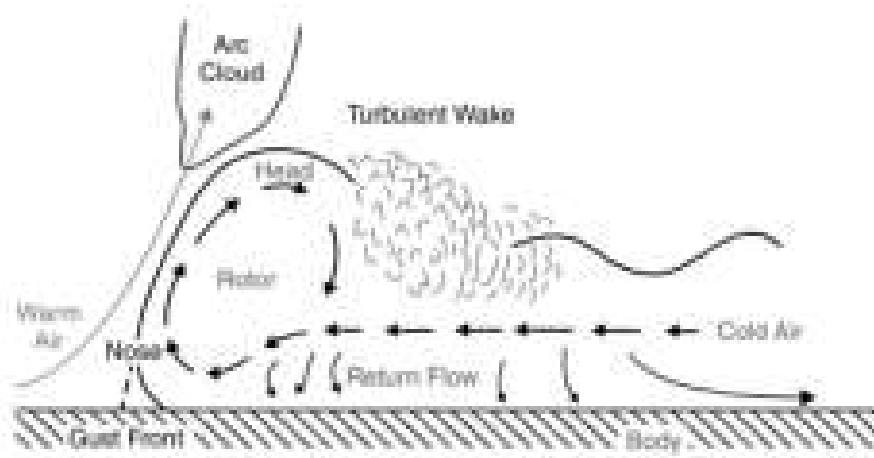
Figure 2.8: Schematics of a density current (Lafore et al., 2017)

Another key feature which contributes to deep convection is the presence of vertical wind shear. A tilted updraught and a strong downdraught give fuel to the development of intense and long-lasting convection. Buoyancy is counteracted in the vertical motion entirely by the pressure gradient acceleration. In a sheared environment, pressure gradient force does not directly counteract updraft. Vertical motion in a sheared flow induces a non-hydrostatic pressure deviation, for about 1 hPa. The updraft is reduced but horizontal acceleration helps the growth of the hydrometeors in convective systems. Clouds in a sheared environment are likely to live longer and lasting updrafts.

Particularly, the presence of easterly shear from AEJ complicates the processes involved in the disturbance growth. Mid-level dry air contributes to the transportation of momentum, thereby propelling a density current. This current attains faster and more profound characteristics along its downshear edge, intensifying convergence. This concentrated convergence not only triggers new convective cells, but also strengthens them. Consequently, in the presence of shear, the density current becomes a catalyst for the initiation of fresh convective cells on its downshear side, thus perpetuating the cycle of convection and complicate the convective processes.

All in all, the main processes affecting convective instability have been explained with the concepts of convective updraughts, downdraughts and vertical wind shear. In addition, the typical convection organisation is categorised into single cell, multi-cells and supercells (Markowski and Richardson, 2011). These classification is based on its corresponding scales. Its structure can vary among different spatial and temporal scales, including some isolated cells, or others in the form of complexes and lines.

A single-cell storm is linked to a weak background wind-shear, upright updraught, precipitation falls within the updraught and cuts off the flow that is feeding the updraught. To add on, multi-cell strom usually requires a moderate to strong wind shear. The formation starts when precipitation falling out of updraught, initiating a downdraught. When it gets more mature, intense downdraught takes place with a density current spreading downshear such that next cell could trigger new cell at the density current leading edge. The interactions between cells are effective to lengthen their convective lifetime. The propagation of a multicell storm is attributed to combination of the propagation of

each cell (mean wind speed in the convective layer) and the speed of the discrete triggering of new cells. Meanwhile, a supercell storm requires vertical wind shear vector that needs both to be strong and to rotate at low levels. In view of the above, these organization process could determine the subsequent hazard risks posed to the regions, such as floods, gust winds, and the like. In relation to the rainfall pattern over tropical West Africa, the formation of multi-cell storms is through cold pools in sheared environments.

2.2.2 Mesoscale Convective Systems

Convection is a widespread and crucial process in geophysics caused by an unstable vertical distribution of thermodynamic energy (Lafore et al., 2017). It aims to restore stable conditions by releasing excess moist energy gained from the heated surface and compensating for energy loss through radiative processes in the upper atmosphere. This phenomenon leads to universally unstable conditions across tropical regions.

Mesoscale Convective Systems (MCS) are characterized as an organized thunderstorm regions with at least 100 kilometres in one direction (Glickman and Walter, 2000). Depending on the length-to-width ratio, typical categories of MCS are more round-shaped Mesoscale Convective Complex (MCC) and more elongated Squall Lines (SL). The structure of MCS/SL comprises of a convective part, associated with tall cumulonimbus clouds at the leading edge leading to heavy downpours, and a large stratiform part which brings prolonged light rainfall. In the convective part of MCS/SL, upward motion of air pacels is driven by latent heating. This part is identified as cloud clusters. As they reach the equilibrium level, they diverge and form the anvil cloud at middle to high levels. This stratiform precipitation fell from the anvil cloud. Convective downdraft takes place below the anvil cloud, which is at the side of the main convective cloud clusters and redistribute momentum. The regional variability of stratiform rain from MCSs can impact the large-scale circulation responding to the heating caused by MCSs.

SL are fast-moving and self-sustaining which is the dominant type of MCS over the tropical West Africa. From Figure 2.9, here shows an illustration of a fast-propagating squall line

Over tropical Africa, there are various rainfall types observed, which is caused by its characteristic kinematic and thermodynamic environment (Fink et al., 2006). Highly organized MCS dominates in the summer months which can bring prolonged intense rainfall (Fink et al., 2006; Maranan et al., 2018). They usually exist in a squall-line structure and are particularly favourable in the combination of cyclonic vortex and mid-level northeasterlies, which generates a strong vertical wind shear at low levels. As aforementioned, high CAPE and CIN eventually contribute to a strong convective growth in a large scale while dry mid-level air layers drive a higher potential downdraft acceleration and thus favour the formation of organized MCS (Klein et al., 2021). The above synoptic-scale forcing modulating rainfall would be attributed to AEW. These squall-line or MCS can be tracked by satellite imagery, such as passive microwave (Fink and Reiner, 2003) or infrared imagery (Klein et al., 2021). Stronger significance can be observed in the Soudanian zone when the summer monsoon kicks in and more moisture convergence occurs. This type of rainfall modulated

Figure 2.9: A diagram showing the structure of an African Squall Line (Lafore et al., 2017).

by AEW is of particular interest in this project because of its paramount importance contributing towards the regional rainfall pattern.

Apart from organized MCS, there are a few more types of rainfall listed in (Maranan et al., 2018). They are less obvious over Sahel-Soudanian region than to southern West Africa (SWA), especially along the Guinea coast. Diurnal circulation could result in some localized, weakly-organized, short-lived convective systems. Some long-lasting but light rainfall can exist as a form of monsoon rain. Knippertz et al. (2017) highlights that rainfall over SWA occurs under the environment with high moisture, low CIN and weak vertical wind shear. This contributes to some isolated thunderstorms or showers which is more driven by sea-breeze convergence along the Guinea coast, rather than synoptic-scale forcing. The most intense MCS formed over SWA are found in March to May which is actually outside of the period of being affected by summer monsoon (Klein et al., 2021).

Fink et al. (2006) has identified some vortex-type rainfalls which is not related to AEW but during unusual synoptic situation. Knippertz et al. (2017) has further proven this phenomenon by observing three westward-propagating coherent cyclonic vortices between 4-13N during the DACCIWA field campaign in June-July 2016, modulating the local wind circulation and rainfall pattern over the Guinea coastal region.

2.3 African Easterly Waves

African Easterly Waves (AEWs) are westward-propagating synoptic-scale features across the West African monsoon region and tropical Atlantic during boreal summer. These notable tropical synoptic disturbances are found between May to October, peak in August and September (Carlson, 1969a,b; Burpee, 1974). A better prediction of AEW is crucial to global numerical weather prediction (NWP) models in multiple ways (Pante and Knippertz, 2019), which has a close connection to the

predictability of synoptics over tropical West Africa and Atlantic basin. AEW provide a source of positive potential vorticity and are the important precursor for tropical cyclogenesis in the Atlantic Ocean (Thorncroft and Hodges, 2001; Hopsch et al., 2007, 2010; Russell and Aiyyer, 2020). AEW is particularly significant in the lower part of the atmosphere and has its peak at about 650hPa.

2.3.1 Basic Information

African Easterly Jet (AEJ) and African Easterly Wave (AEW) play a vital role in shaping the West African climatic pattern during the summer months. AEJ refers to the easterly jet formed at roughly 15°N, which is confined by the geostrophic balance between the hot and dry Sahara air layer at the north, and the moist and cooler monsoon layer at the south (Parker et al., 2005). The surface baroclinicity of the two air masses leads to the jet to be found over the mid-troposphere. In terms of the associated potential vorticity structure, it is observed that there are two opposite signs of PV anomalies at the southern and northern flank of the jet. Beneath the jet, extending up to the Sahel region is the moist monsoon layer. The monsoon layer increases its depth towards the south and it is modulated by the land surface on diurnal time-scales due to the growing convective activities in the mixed layer and the formation of shallow cumulus clouds. Above the monsoon layer and the jet, SAL is hanging on top of the monsoon layer when the two layers converge. SAL is connected to the land surface.

Previously as suggested by Kiladis et al. (2006), a typical development of AEW starts from an orographically favoured genesis area for MCSs over Sudan (Berry and Thorncroft, 2005) and the Ethiopian Highlands (Mekonnen et al., 2006) over central and East Africa. These convective systems propagate westward along the AEJ and the AEW activities amplify. Its horizontal and vertical structure vary as it propagates westward.

2.3.2 Growth processes

African Easterly Waves develop barotropically from a baroclinic jet, namely from African Easterly Jet (AEJ). The initiation of AEW relies on the upstream triggers from convection. This is on account of the convective activities provoked in the central or eastern African region. Details will be presented as follows.

One key process feeding AEW growth is from the large-scale dynamics. AEW develops through barotropic-baroclinic energy conversion processes, namely to fulfill Charney-Stern criterion (Charney and Stern, 1962). The reason for a barotropic growth is that AEW associated with initially small perturbations to the flow barotropic instability requires that basic state absolute vorticity gradient must have both signs in the domain. Over the AEJ level, the wind vector decreases logarithmically towards the side of the jet. This forms two vorticity gradients.

$$\eta = \left[-\left(\frac{\partial \overline{u}}{\partial y} \right)_\theta + f \right] g \frac{\partial \overline{\theta}}{\partial p} \tag{2.1}$$

Potential vorticity is evaluated on isentropic surfaces η. The northern and southern cyclonic disturbances are leaning against the shear of AEJ in between. AEJ is feeding kinetic energy to the disturbances.

$$\frac{\partial \overline{\eta}}{\partial y} \equiv \beta - \frac{\partial^2 \overline{u}}{\partial y^2} - \frac{f_0^2}{N_s^2} \frac{1}{p_s} \frac{\partial p_s}{\partial z} \frac{\partial \overline{u}}{\partial z} - \frac{f_0^2}{N_s^2} \frac{\partial^2 \overline{u}}{\partial z^2} \tag{2.2}$$

where N_s^2 refers to Brunt-Väisälä frequency.

As suggested by Charney and Stern (1962), the horizontal and vertical shear of the mean zonal wind in creating the instability such that $\frac{\partial \overline{\eta}}{\partial y}$ change sign somewhere in the fluid. From the case of AEJ, horizontal and vertical shear terms, namely $\frac{\partial \overline{u}}{\partial y}$ and $\frac{\partial \overline{u}}{\partial z}$ are negative terms. This fulfills the prerequisite of barotropic instability. Eddy momentum flux transports zonal momentum against the background gradient, which means extracting kinetic energy from the jet. It is commonly observed from the low-level streamlines that as the jet and the wave disturbance propagates westward from the continental Africa to Atlantic ocean, the disturbance is tilted horizontally against the shear of the jet. The opposite tilt would favour jet acceleration.

Other than barotropic growth, since convective activities would contribute to a considerable amount of baroclinic energy conversion, the contribution of this is also remarkable. Latent heat release due to diabatic processes lead to redistribution of potential vorticity and impact AEW intensity.

The genesis of AEW requires upstream triggers. AEW is initiated over Darfur mountain region in Sudan and East Africa Ethiopian Highlands (Berry and Thorncroft, 2005; Mekonnen et al., 2006). A certain intense localised heating is found there, as they are close to the entrance of AEJ. The genesis could be associated with this deep convective burst as suggested by Thorncroft et al. (2008) and this usually exists a series of events composed of several mesoscale convective systems over elevated terrain in Sudan. The disturbance has to respond to it through baroclinic and barotropic growth over tropical Africa. Convective activities upstream serve as a prerequisite for disturbances due to diabatic heating. This warm anomaly forms at lower levels near the origin of the convection. A vertical gradient is created and thus a new PV anomaly which helps the wave propagate westward. It interacts with a mid-level region of high potential vorticity (PV) situated on the cyclonic shear side of the African easterly jet, promoting baroclinic growth. This interaction is further enhanced by the emergence of small-scale PV anomalies generated by intense convection within the evolving baroclinic structure of the AEW.

As the AEW propagates to the West African coast, its baroclinic characteristics weaken, yet convective activity persists. Mid-level PV anomalies within the AEW blend with each other and with PV anomalies generated by convection over terrain ahead of the system. These mergers give rise to a notable PV feature that moves away from the West African coast and become a source of tropical cyclogenesis.

2.3.3 Structure

AEWs are prominent in the lower troposphere, peaked at AEJ level, around 650hPa. These waves have a characteristic period of 2 to 6 days and wavelength ranging from 2500 to 4000 kilometers. AEWs develop within the AEJ and are influenced by its position, intensity and structure. Modulation in the AEJ would also affect AEW. As discussed in the previous part, AEWs are tropical disturbances that are sustained by barotropic-baroclinic energy conversion. Its structure and growth processes would vary depending on the location or time of day.

AEW structure could not be simply described by a single layer. From Figure 2.10, at the mid-troposphere level, AEW trough–ridge structures are tilted against the horizontal shear north and south of the jet, which is attributed to its barotropic growth. Mostly the trough axis is negatively tilted at the northern flank of AEJ while positively tilted at the southern flank.
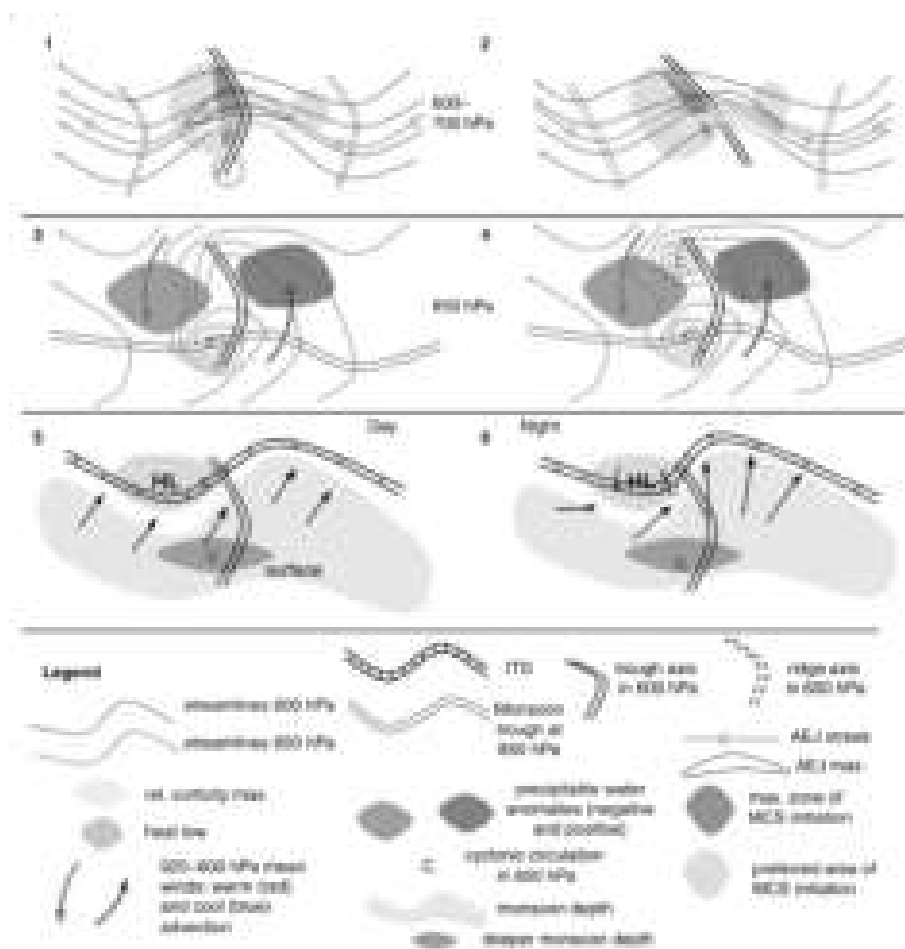

Figure 2.10: A schematic diagram illustrating the AEW structure. The left panel shows a 'normal' situation while the right panel shows the structure given an additional barotropic shear, with a stronger easterly wind to the north within AEJ (Cornforth et al., 2017).

As seen in Figure 2.10 originated from Cornforth et al. (2017), at 600-700 hPa level, AEW troughs are seen at the AEJ level, with trough and ridge lines aligning with streamline curvature. The wind exhibits a cyclonic curvature, with the trough axis tilting upshear. This highlights that faster AEJ winds occur to the east of the trough. Westward tilting occurs both north and south of the AEJ axis.

At 850hPa level, a closed vortex would take place and usually lies at the equatorward shear side of AEJ. This marks the relative vorticity maximum, associated with the baroclinic wave tilt. It is situated at the west of AEW trough axis at 600hPa. The vortices at 850 hPa coincide with the line of maximum vorticity, delineating the monsoon trough and favour thunderstorm development. Precipitation Water (PW) denotes an integrated measure of northward monsoon system penetration. Within the AEW structure, there is a notable feature from the spatial deviation of PW (PW*). PW* and thermal anomalies coincide at 850 hPa. The peak PW* lies east of the AEW trough. Southerly winds at AEJ level, high θ_e in the northward moist air occurs, and θ_e (which leads to a strong convective instability) contribute to this pattern. High CAPE associated with an AEW follows a SW to NE pattern.

The monsoon depth is characterized by a deep layer of cool and humid air with predominant southerly advection. Notable for high PW*, relative anticyclone flow at lower levels. Convective systems are commonly observed to be embedded along with the westward propagation of the AEJ. Fast-moving MCS aligns with the AEJ core ahead of the trough. Slow-moving systems appear southward with weak wind shear and deep monsoon depth.

Finally, as for the surface and low-level The displaced northward air exhibits a cooler, shallower, and more humid boundary layer (BL), featuring extended shallow cumulus clouds and a deeper monsoon layer compared to the southward region. The occurrence of ITD displacement is indicative to the northward intrusion aligning with AEW, influencing its progression. The ITD displays a diurnal cycle with low-level wind surges and cyclonic circulation around the heat low and AEW trough. A significant north-south ITD deviation follows the AEW, observed at 925 hPa as well. Advection of moist and cooler air from the south at the eastern flank of the trough, and the dry and warmer SAL from the north, help build up CAPE and reduce CIN. This serves as the favourable environment to drive strong convective activities over tropical West Africa.

Another approach to understand the wave structure is through meteorological variables. In terms of its vertical structure of meridional wind, OLR minimum is located mainly in the trough given low-level southerlies. There is almost vertical wind structures up to 300hPa and abrupt reversal above that. Lower-level maxima descend from 500hPa to the surface. The structure is tilted against the shear of AEJ. Before reaching the coast of West Africa, the vertical profile of temperature within an AEW disturbance has a three-tiered vertical structure. It is a complicated mixture of advective and convective signals. The main center at 250-300hPa due to latent heating. For instance, when there is rainfall at Sahel, cold air is found at the bottom as evaporating cooling occurs. The temperature gradient goes reverse which is caused by the difference in the lapse rate. Above the mid troposphere, latent heat is released during the condensation process.

2.3.4 Identification and tracking

There have been multiple studies done on easterly wave identification and tracking methods. Fink et al. (2004) and Agudelo et al. (2011) have suggested using Hovmöller diagram to identify the AEW troughs based on spatio-temporal filtered 2–6 days meridional winds and westwards-propagating

relative vorticity anomalies. After that, Kiladis et al. (2006) has tracked AEW signals based on satellite-derived outgoing longwave radiation (OLR) after spectral filtering to the corresponding AEW wavelength and frequency. These signals is associated with the lowest OLR and mean convection appears strongest. AEW are tracked based on the kinematic predictors, including the anomalies of curvature vorticity advection from the wind vector fields.

Previous work on AEW tracking covers mostly on utilizing kinematic variables, such as such as 850- or 700-hPa meridional wind (Burpee, 1974; Pytharoulis and Thorncroft, 1999; Gu et al., 2004), or relative vorticity (Reed et al., 1988; Thorncroft and Hodges, 2001; Hodges et al., 2003).

In specific, the study of Belanger et al. (2016) utilized data from ERA5, specifically the zonal and meridional wind fields, i.e. u and v winds, at a resolution of 0.5 degrees and sampled every 6 hours over tropical Africa and the Atlantic region. The methodology entails several steps for identification and subsequent tracking of Atmospheric Easterly Waves (AEW).

The identification process involves multiple steps. Initially, curvature vorticity (CV) was computed from u and v components and then resampled to a coarser grid of 2.5x2.5 degrees. The computation of CV Anomalies (CVAs) followed, based on a previously determined ERA5 CV climatology. Advection of CVAs through u dx and v dy has been calculated. Lines where CVA-Advection equals zero (CVA maxima) were established. These zero-lines were filtered with the criteria, such as being above the 66th percentile of CVA, possessing a positive 2nd advection-derivative (indicating local maxima), and being associated with easterly winds ($u < 0$). Finally, only wavetroughs within specific latitude boundaries (5°N to 25°N) and surpassing a minimum length were retained, aiming to eliminate small artifacts.

Alongside in terms of the tracking method, Belanger et al. (2016) introduced a novel technique, structuring the data in a graph format inspired by Limbach et al. (2012). Wave troughs at a given time t were compared with those at t+6h and t+12h. A polygonal search area was defined around the predicted location based on estimated speeds (ranging from 0 to 15 ms^{-1}). Overlapping areas between these polygons and wavetroughs at corresponding times were used to link wavetroughs into the same AEW. Edges between these connected wavetroughs constituted the AEW graph, which served as the basis for track extraction. For instance, if an edge t to t+6h exists and the t+6h wavetrough has an edge to t+12h, then a 12-hour track from t to t+12h is established.

To compute the tracks, these graph edges are connected. The outcomes encompass split and merge information, denoting wave troughs that point to multiple downstream or converge into a single wave trough. Transitive edges are removed, and further complexities arise in defining track start/end points due to the intricate nature of the tracking graph. Filtering is applied to retain tracks spanning over 2 days and exhibiting a westward propagation speed exceeding a threshold of 3 ms^{-1} within each 48-hour window. This comprehensive methodology allows for the identification and tracking of AEW in the targeted regions. A detailed description of utilizing the wave trough dataset in this project is provided in the methodology section.

2.3.5 AEW and interaction with precipitation

AEWs are known to have the effects in modulating the development of MCS or SL. However the variating forcings over the time of day and locations make the causal relationship much less visible and more challenging to comprehend. AEW and MCS have a stronger association, especially over the Soudanian-Sahelian region. Fink and Reiner (2003) has highlighted that 42 percent of squall lines observed are AEW-driven. Squall lines are usually propagating along with the southern track of the vortices. The Sahel region, particularly during the monsoon season, provides the favourable conditions for the rapid genesis of squall lines. This phenomenon is attributed to the simultaneous emergence of multiple factors contributing to their development.

The warm Saharan Air Layer (SAL) situated above the moist monsoon air substantially contributes to convective inhibition, thereby leading to the accumulation of Convective Available Potential Energy (CAPE) (Cornforth et al., 2017). The presence of moisture within the monsoon layer, results in increased precipitation water (PW), easterly wind shear of approximately 15 m/s spanning around 4 km vertically between the African Easterly Jet (AEJ) and the monsoon layer, as well as the inclusion of dry air within the AEJ layer, responsible for the provision of downdrafts and density currents. Diabatic processes from rainfall systems such as the MCS, associated with AEW induces stronger baroclinic energy conversion.

Multiple studies have already suggested that rainfall peak tends to be found ahead of the wave trough, namely to the west of the trough (Duvel, 1990) as the wave propagates over the continent. There are two main tracks of vortices over West Africa at 5°N and 15°N, and then converge over Atlantic on latitude 17.5°N (Diedhiou et al., 1999). Wave activities are strongest in Aug and September. Rainfall, convection and monsoon flux are strongly modulated by AEW.

To add on, the region ahead of AEW troughs is a favourable location for the genesis of the squall line in all tropical West African countries (Fink and Reiner, 2003). As the wave disturbances propagate to the ocean, rainfall maximum tends to fall at the wave trough or behind it (Fink and Reiner, 2003). It is common to observe two troughs or cyclonic vortices centers that travel westward along with AEJ at either side of the jet, which could be related to the northern and southern tracks.

Gu et al. (2004) suggested the two distinct relationships between the waves and convection. AEW could be quantified by 850hPa meridional wind component. Southerly wind perturbations and precipitation anomalies tend to be in-phase given its moisture abundance which indicates maximum precipitation occurs at or just behind the max southerly wind. However ahead of the wave trough, where northern wind perturbations dominate. Convective diabatic heating enhances the development of these easterly waves which contributes to wave propagation.

Convection formed ahead of the PV anomaly leads to isentropic lifting or diabatic heating which then creates a vertical gradient (Berry and Thorncroft, 2005). A new PV anomaly is formed ahead and the system can then propagate westward. Moisture convergence allows the propagation of the AEW due to the reorganization of the AEW center toward the downstream PV maxima. In contrast, if the convection is close to the center, it can amplify the wave through vortex stretching.

The differences in convective activity can result in different AEW growth rates (Hsieh and Cook, 2007). Especially convective activity leads to larger baroclinic energy conversions. This coupling is particularly crucial especially when the convection relative to the trough axis migrates from ahead of WT to a relative position closer to WT. This is non-negligible effect which would happen over the region near the Guinea Highland. The wave trough is likely propagating from the land-ocean boundary over the West African coastline. Therefore a thorough understanding of the coupling effect is crucial for predicting the rainfall pattern in the region.

Cornforth et al. (2009) has emphasized the significance of moist processes associating to AEW development. Amplitudes at jet-level and in northerly low-level regions increased overall, although in moist conditions, low-level amplitudes decreased due to the interaction of AEW with convection, a trend consistent with observations during the peak monsoon period. The evolution of these phenomena was governed by two distinct processes, for example AEJ was replenished influenced by heat fluxes upstream, and the growth-rate of the wave, affected by damping, along with the slower development rate of the jet. While the AEJ predominantly develops in conditions of dry convection, the final disturbances of the wave are influenced not only by the AEJ but also by other moisture-related processes throughout its lifespan, with moisture playing a role in influencing upstream triggers.

Janiga and Thorncroft (2016) has highlighted that AEW and convective development depend strongly on the large-scale environment, namely lift, moisture, conditional instability and wind shear. From Fig. 2.11, ahead of the trough, it is expected to be the northerly regime, which favours adiabatic forcing for ascent, but mainly forcing for descent in the southerly regime. More ascent would enhance column relative humidity and an increase in moisture content is expected, and such phenomenon contributes to higher rain rates associated to the wave trough propagation.

Vertical wind shear is a crucial element in facilitating the formation of supercells and sustaining their lifetime, given both its strength and considerable amount of low-level rotation (Lafore et al., 2017). The shear environment given by AEJ and AEW leads to persistence in convective activities. Organized deep convection embedded within the AEW plays an important role in influencing the synoptic-scale mean potential vorticity and energetics of the AEW (Berry and Thorncroft, 2012). Diabatic heating associated with convection is important in producing eddy available potential energy of the synoptic AEW given the hybrid adiabatic and diabatic structures. Diabatic processes prompt the generation of PV within the AEW trough leading to the intensification of the wave. Active convection favours synoptic AEW along their propagation to persist for a longer time.

2.4 ECMWF Integrated Forecasting System

2.4.1 ECMWF IFS Infrastructure

The European Centre for Medium-Range Weather Forecast (ECMWF) has pioneered its numerical weather prediction (NWP) model system in 1992, which is recognised as one of the most skillful
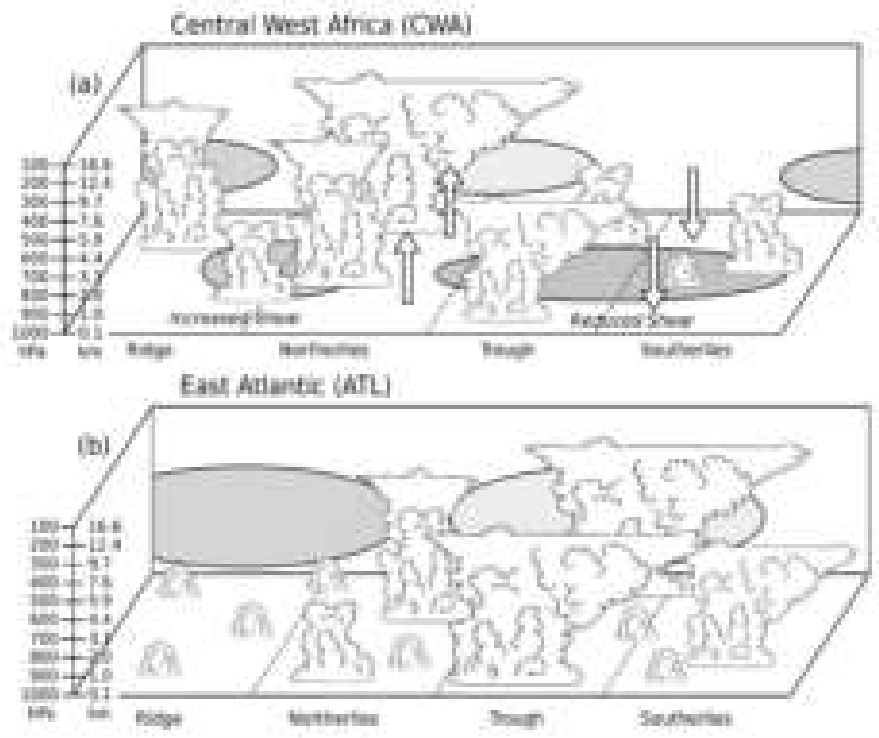
Figure 2.11: Illustration of the vertical profiles associating with AEW-precipitation coupling over (a) Central West Africa (CWA) and (b) Tropical Atlantic (ATL). Green (brown) circles indicate positive (negative) moisture anomalies. Red (blue) circles indicate regions of warm (cool) low-level temperatures and increased (reduced) CAPE. Arrows indicate the adiabatic forcing for ascent or descent (Janiga and Thorncroft, 2016).

global NWP models nowadays. The forecasting system is comprised of a deterministic and an ensemble weather forecast. A deterministic forecast produces a single point value as its output based on the input data as initial conditions. An ensemble weather forecast operates by a collection of forecasts that generates a potential range of future weather scenarios and aims at giving our best estimate of the initial state of the atmosphere. Numerous simulations are conducted, each with small deviations in their initial conditions and perturbation in the weather models. A small difference in the initial conditions could lead to greater perturbations in the future states. These deviations account for the inherent uncertainty in the initial conditions and the approximations made in the models, resulting in a diverse set of possible weather outcomes. If the range of outcome varies a lot, this infers that there is a lot of uncertainty about the possible outcome. The uncertainty of a weather forecast model could come from the errors of the initial conditions, boundary conditions and the model. The chaotic nature of the physical system has posed a great challenge for NWP models to represent completely, for example the variation of different processes within a day or due to multiple weather regimes. On the other hand, relying solely on a single deterministic model can be misleading to users when the predicted outcome differs from the actual weather phenomenon. In contrast, the ensemble forecast method is highly valuable as it provides essential information about the likelihood of various weather scenarios. This enables users across sectors like agriculture, energy, industry, and aviation services to make informed decisions. The society greatly cherishes and values this approach for its utility and significant contributions.

Taking all the deterministic forecasts together become an ensemble, which exhibits the spread of these possible outcomes and the likelihood of their occurrence. The benefits of stochastic parameterization is to represent the possible systematic errors of the model, trigger of noise-induced drifts or regime changes, enhancement of ensemble spread, quantify forecast uncertainty. These 51 medium-range forecasts in a run are computed up to 15 day lead time and the performance at different lead times becomes a useful information for further investigation on the skills of the NWP model in representing different weather phenomenon.
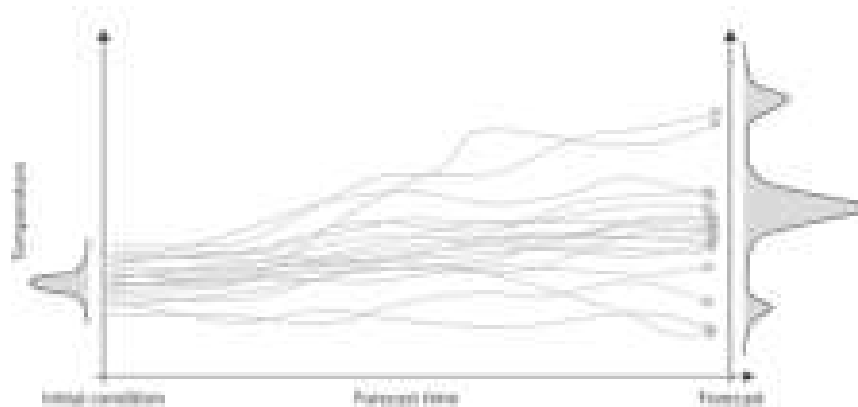

Figure 2.12: Illustration of Ensemble Prediction System for temperature (ECMWF Confluence Wiki)

The behaviours of the atmosphere are mainly calculated by understanding the dynamics and physics. The dynamic component of NWP models deals with representing the large-scale atmospheric motion. It involves solving the fundamental equations of fluid dynamics to simulate the evolution of atmospheric variables over time. The key equations used in the dynamics component are the primitive equations, which is a set of partial differential equations that govern the behavior of the atmosphere, i.e. conservation of mass, momentum, energy and ideal gas law. However, the computation in NWP models is indeed very computational costly. Parameterizations deals with subgrid-scale processes, those occurring at scales smaller than what the model can resolve. Multiple physical processes would have to be represented through parameterizations, including radiation, convection, cloud microphysics, turbulence and the like.

Specifically in terms of the importance of parameterizing convection, the convective processes are not resolved explicitly at the grid scale due to computational limitations. Instead, simplified representations of convection are used in the model, referred to as parameterizations. These parameterizations are empirical or semi-empirical relationships that estimate the effects of convection on large-scale variables based on simplified representations of the convective processes. The parameterizations typically use subgrid-scale information, such as the large-scale environment, moisture profiles, and stability conditions, to estimate the convective heating, moisture transport, and other effects.

The key difference between explicit and parameterized convection lies in the level of detail and resolution at which the convective processes are represented. Explicit convection allows for a more detailed and realistic representation of individual convective cells, their interactions, and the associated dynamics. On the other hand, parameterized convection provides a simplified

representation of convective processes at larger scales, relying on empirical relationships to estimate their impacts on the larger-scale atmospheric variables.

2.4.2 Moist Physics upgrade

Thanks to the advancements in the computational capabilities which permits the running NWP model at storm-resolving scale (Satoh et al., 2018; Stevens et al., 2019; Freitas et al., 2020; Hohenegger et al., 2020; Wedi et al., 2020), ECMWF has established a strategic objective to enhance the horizontal grid resolution from 18km to 5km (Bechtold et al., 2020). The operational NWP model has been constantly improving through updating its version cycle. As part of this effort, the horizontal resolution has already been increased from 18km to 9km in IFS Cycle48r1 in 2023. Additionally, major improvements for the IFS have been made to the representation of moist processes from the physically based parametrizations since Cycle 47r3, such as cloud dynamics, convection, turbulent mixing, and cloud microphysics. The upgrade from IFS Cycle 47r2 to IFS Cycle 47r3 took place in late October 2021. These revisions aim to maintain a straightforward, efficient, accurate, and scale-independent depiction of these processes. It is suggested that the upgrade of these subgrid-scale processes parameterization would help simulate a better structure and organization of storms. New convective instability clousure is expected to align better with the probability density function of observed rainfall, derived from radar and satellite-based rainfall products. It introduces new forecast products, like Most Unstable Convective Available Potential Energy (MUCAPE), mixed-layer CIN, CAPE variants, and a clear air turbulence diagnostic, resulting in reduced biases in fog, rain and snow. These changes contributes to better representation of the extratropical geopotential heights and winds, reduced wind errors in the tropics, and improved character of precipitation, especially in strongly forced convective systems. The focus of the IFS parameterization for moist processes includes turbulent mixing, convection, subgrid clouds, and microphysics, addressing previous inconsistencies between buoyant updrafts used in turbulence and convection schemes.

ECMWF Operational Analysis updates its cycle in roughly about 1-2 year(s). Each model versions might lead to inhomogeneity in the integration. Therefore regular comparison between different model versions in relation to the observational data is necessary.

Specifically, Becker et al. (2021) suggested that the best agreement with the satellite retrieval Global Precipitation Measurement (GPM) Integrated Multi-satellite Retrievals for GPM (IMERG) is achieved when an integrated and scaled total advective moisture tendency term. Q_{adv} is incorporated into the convective instability closure.

$$Q_{\text{adv}} = -\alpha L_v \tau_c \frac{1}{gH} \int_{p_s}^{60\text{hPa}} \frac{\overline{q_v}}{\overline{q_s}} \left. \frac{\partial \overline{q_v}}{\partial t} \right|_{\text{adv}} dp$$

$$M_{\text{base}} = M_{\text{base}}^* \frac{PCAPE' + Q_{\text{adv}} - PCAPE_{\text{BL}}}{\tau} \times \frac{1}{\int_{P_{base}}^{p_{top}} \frac{g}{T_v} M^* \left(\frac{\partial \overline{T_v}}{\partial z} \right) + \frac{g}{c_p} dz}$$

The inclusion of this advective term into the closure allows for improved coupling between the convective parameterization and mesoscale dynamics, leading to enhanced precipitation intensity, reduced precipitating area fraction, smaller individual deep convective system sizes, and westward propagation. However, despite these improvements, the duration of rain events continues to be underestimated. It highlights that resolving deep convection by scale-aware parameterization is still necessary even at a resolution of 9 or even 4km for global NWP models.

2.4.3 Difficulties in predicting African rainfall systems

Predicting rainfall and MCS over West Africa is particularly hard since it is given by multiple factors including synoptic, mesoscale and local topographic disturbances. It is hard to distinguish the importance of synoptic-scale forcings towards rainfall variability. There are also other factors affecting the moisture distribution include large-scale environmental moisture advection, convectively-coupled equatorial waves' actions, including CCKW, MRG, ER waves (Schlueter et al., 2019). However due to data sparsity of observation data from rain gauges in Africa, limited amount of observations is assimilated into NWP model computation. It is rather difficult to find persistence from the rainfall pattern and most NWP models nowadays are still incapable in capturing the high rainfall variability of tropical Africa (Lafore et al., 2017).

The primary focus of this project lies in studying how convective precipitation over tropical Africa, a region known for highly active MCS, to what extent would be modulated by AEW. Conventional convective parametrizations often fails to capture the characteristics of MCS without taking account of the synoptic forcings (Vogel et al., 2018; Pante and Knippertz, 2019), leading to issues such as widespread but insufficiently intense convective precipitation (Stephens et al., 2010) and inaccurate initiation and duration times (Marsham et al., 2013). Moncrieff et al. (2017) highlighted the failure of many traditional convective parameterizations in representing MCS and squall lines over tropical Africa, as their development heavily relies on vertical shear. To address this issue, a shear-aware multi-scale convective structure parameterization (MCSP) has been introduced, which helps with better representations of interactions with mesoscale dynamics and improved capturing of MCS and organized convection (Moncrieff et al., 2017; Chen et al., 2021).

MCS forecast has a very low skill score, even for a very short lead time Elless and Torn (2018). They propagate westward along with AEJ or AEW. AEWs are synoptic features which show a relative higher predictability. Older parameterization did not take account of the total advection of moisture in the environment. Errors might occur for the position of the convective system as the development of it has no preference over direction (Crook et al., 2019), but observed MCS propagate predominately towards the Atlantic in the direction of AEJ due to parameterization. According to Becker et al. (2021), the known issues of the current NWP models in simulating deep convection are listed in Table 2.1.

	Parameterization	**Explicitly resolved**
Precipitation Intensity	Too light	Too strong
Precipitation area fraction	Too widespread	Too cluster
Duration	Too short (both Q_{on}/Q_{off})	Well captured
Size	Too big	Too small
Propagation	No preferred direction	Better coupled with the dynamics

Table 2.1: Known issues of representing deep convection in the existing NWP models (Becker et al., 2021).

2.4.4 Uncertainty in predicting AEW and associated rainfall in EPS

Janiga and Thorncroft (2013) has suggested that diabatic PV generation is dependent on the vertical profile of latent heating, which is poorly constrained over tropical Africa and the Atlantic. Diabatic processes are of paramount importance in affecting AEW position, intensity and variance but only a few of these studies have addressed the effect of those processes or the environment on the predictability of AEWs. Elless and Torn (2018) has done a study on the predictability of AEW observed in the periods of 2007-2009 and 2011-2013 and it has suggested that AEW intensity bias could be influenced by the error in simulating convective activities but the relationships vary over time. Elless and Torn (2019) adds on that the variance of AEW intensity could also be linked to the uncertainty from simulating the diabatic processes, especially for regions with high moisture availability or its variability. The coupling of AEW and rainfall is worthwhile to evaluate and eventually impacts the overall prediction of the synoptic pattern over tropical Africa. This has suggested that AEW forecasts are likely sensitive to the amount of convection and its location relative to the AEW center.

AEW intensity forecasts were most sensitive to the overall wave structure, longer lead time forecasts (24–48 h) were more sensitive to downstream thermodynamic variables, suggesting errors in convective processes could play a key role in AEW predictability at longer lead times (Torn, 2010). Convective-scale errors can rapidly grow upscale and begin to influence large-scale features as highlighted by Lorenz (1969). In this regard, this has created the research objective in view of the possible improvement in the moist physics in simulating AEW and a complete statement about the research questions will be introduced in the next section.

3 Research Questions

This section explains the research statement of this master thesis. As mentioned above, the growth of AEW strongly depends on barotropic-baroclinic growth and upstream triggers. Along the wave trough, two distinctive potential vorticity (PV) anomalies are commonly found. Positive PV is usually associated with moist convection, which drives stratiform rainfall and the frequent occurrence of MCS around the region. Therefore, it is foreseen that vortex centers are often embedded within the AEW dynamics.

Moisture convergence is an important factor to sustain the development of AEW. Due to the baroclinic nature of AEW (Reed et al., 1977), a good understanding of the coupling of precipitation and AEW would be important for interpreting the rainfall pattern. Latent heat release causes the redistribution of potential vorticity and thus has an effect on AEW development, by observing the respective propagation and intensity. As described in the previous section, potential vorticity generated from convection to the west of the AEW trough center would enhance the westward propagation across the African content. On the contrary, diabatically generated PV over the Guinea highlands over the West Coast of tropical Africa can merge with the PV maximum in the AEW trough which contributes to a stronger wave. From the above, it is shown that moist processes have a great influence on AEW development. The phase relationship between AEW and precipitation will have to be considered comprehensively. One of the approaches will be the location of these dynamic features, since the effect of them situated over land and ocean could exhibit a distinguished manner respectively.

There has been a lack of skill in predicting precipitation in tropical west Africa (Vogel et al., 2018) which could be attributed to the insufficiency in the parameterization of convection, where mesoscale convective systems are dominating rainfall systems. The development of MCS is highly dependent on the thermodynamic profile and vertical wind shear.

In view of the moist physics upgrade in the ECMWF Integrated Forecast System, this is suggested to bring improvements in the simulation of the structure and organization of storms, thanks to a possible improvement in moisture convergence organization. Rainfall prediction in tropical West Africa is difficult due to the underlying challenges in constraining the moisture field in the domain. Taking operational forecasts of the summer months in 2021 and 2022 has incorporated the analysis of forecast data originated from the two model versions, namely IFS Cycle 47r2 and Cycle 47r3, where the moist physics revision has already taken place. This has brought up the research incentives of the project, that is to investigate if the moist physics upgrade in the ECMWF IFS would bring any behavioral changes in representing the AEW-precipitation coupling through a composite analysis approach. Therefore, the following lists out the research questions of the study.

- What are the main changes in the phase relationship between AEW and rainfall in the ECMWF IFS in 2021 and 2022? How does the pattern change with lead time?

- How does the variability of the AEW-rainfall coupling change with different AEW intensities?

- Is there any observable relationship between AEW and other variables related to the moisture and dynamic fields in the forecast between the two years?

- Are there any similar patterns from associating various variables with vortices centers in the tropical Africa and Atlantic?

To validate the precipitation forecast, observable dataset is needed, which is applying the satellite-driven product Integrated Multi-satellitE Retrievals for GPM (GPM-IMERG). The next section will describe the techniques in full.

4 Data & Methodology

This chapter provides the description of the datasets and methodology applied, which aims at addressing the aforementioned research questions of this study. The aim of the analysis is to investigate if there are any particular patterns observed from precipitation rate and other possible variables in the ECMWF IFS model, having coupling effect with African Easterly Waves, which is in line with previous studies depicting AEW dynamics. It would be also intriguing to discover if there would be changes between 2021 and 2022 given the change in the formulation of the moist physics and how the patterns are changed or lost as the lead time propagates.

4.1 Datasets

This section describes the available datasets for the investigation. Firstly, a wave trough (WT) dataset has been compiled so as to represent the AEW troughs in the project. Secondly, forecast datasets of multiple atmospheric variables are extracted, including precipitation rate, several variables related to moisture fields, namely Total Column Water Vapour (TCWV), Vertically Integrated Moisture Divergence (VIMD), 700hPa Specific Humidity, and other variables related to the dynamics, including 700hPa and 850hPa Relative Vorticity (ζ700 and ζ850), and low-level vertical wind shear between 600-950hPa. The operational forecast run that was used in 2021 and 2022, is based on the IFS Cycle version by then, namely IFS Cycle 47r2 before 27 October 2021 and IFS Cycle 47r3 after that. Therefore, there is a moist physics change behind between the datasets of the two years.

Specifically, to contrast the performance of the precipitation pattern from the NWP model computation, an observation based on satellite-derived rainfall product is also used. With the knowledge that AEW are prominent features found during the West African summer monsoon seasons, the analysis focuses on AEW-driven effects in the period between June to October each year. The following section provides a detailed description.

4.1.1 Wave trough data

The wave trough data is based on the 2-6 day filtered 700hPa curvature vorticity (CV) anomalies of ERA5 reanalysis data. It has an horizontal resolution of 0.25° x 0.25°. The computation refers to wave trough identification and tracking method from Belanger et al. (2016) with slight modifications, which was based on Fischer et al. (2023).
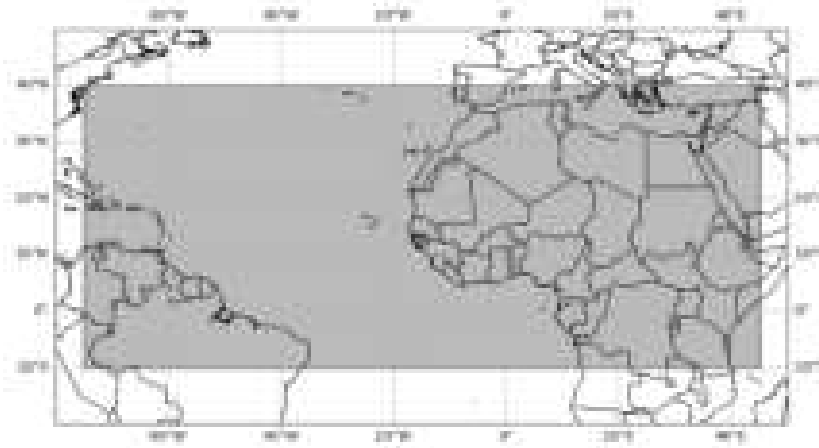
Figure 4.1: Map of tropical Africa and Atlantic with the domain shaded

The following explains the identification and tracking methods of the wave trough. The curvature vorticity was computed based on the zonal and meridional wind components, and has been resampled to 2.5° x 2.5°. CV anomalies (CVAs) were calculated based on a precomputed ERA5 CV climatology. Lines of CVA-Advection equal to zero could be found, which refers to the maxima of CVAs. These zero lines were filtered with the criteria, namely above 66th percentile of CVA, the second derivative of advection was greater than zero to look for the local maxima and u < 0 which kept only easterlies. Moreover, the final wave troughs were kept only if these were within the domain of 5-25N and had a minimum length so as to ensure small artifacts being removed.

Following Limbach et al. (2012), the wave trough (WT) dataset has a structure of sets of WT features every six hours. Edges indicate the points with zero CVA-Advection. Graphs indicate a subset of tracked WT features from different time steps. The number of tracks indicates the number of AEWs, which a WT could be linked together from different time steps based on the tracking algorithm as described before.

4.1.2 Precipitation data

The forecast and observation precipitation datasets are presented in the following. The European Center for Medium-Range Weather Forecast (ECMWF) Integrated Forecast System (IFS) is one of the leading reputable numerical weather prediction models in the world. ECMWF initializes its model run every twelve hours daily, namely 00 UTC and 12 UTC and creates 15-day medium range forecast. From there, precipitation rate forecast datasets of 2021 and 2022 were extracted with a horizontal resolution of 0.5° x 0.5°, a 6-hourly temporal resolution for each model run output. The selected domain is focusing on tropical Africa and Atlantic (10°S - 40°N, 75°W - 45°E).

ECMWF has updated its operational forecast cycle run, especially with a moist physics upgrade from IFS Cycle 47r2 to Cycle 47r3 in October 2021. The comparison of the rainfall field between

the two years and identifying the difference between the two cycles, on top of the slight possible difference in the dynamics between these two years.

In addition, in order to validate the precipitation rate forecast, a reliable rainfall observation product is necessary. In this project, Integrated Multi-satellitE Retrievals for GPM (IMERG) is used (Huffman et al., 2015). IMERG is a satellite-driven rainfall observation product produced from NASA Global Precipitation Measurement (GPM) satellite constellation over the most areas of the globe. This is a complete merged microwave-infrared (gauge-adjusted) precipitation estimate. The latest version IMERG Final Run V07 has been used in this project instead of the Early Run and Late Run. The Final run data was first based on the Late Run version which used a climatological adjustment that incorporated gauge data. This has further used a month-to-month adjustment to the monthly Final Run product, which combined the multi-satellite data for the month with gauges of Global Precipitation Climatology Centre (GPCC). Moreover the Final Run product complements from the Late Run version which the Late run version was computed about 14 hours after observation time, which might not have fully incorporated a microwave overpass. The Late and Final Runs have a constant ratio between them for the entire month given a constant multiplier by the gauge adjustment. Thus the Final Run product would be recommended for research purposes.

The raw data is stored in a spatial dimension of 0.1° x 0.1°, then remapped into 0.1° x 0.1° in order to match the WT resolution. The data was originally a half-hourly temporal resolutionm, then further aggregated into six-hourly, centered at 00UTC, 06UTC, 12UTC, 18UTC so as to obtain the same temporal grid as the ECMWF forecast data .

Exact agreement in the magnitude between IMERG and ECMWF precipitation fields cannot be expected since the nature of both products is different, namely, the former is a satellite-derived product while the latter is a model-run product. This might lead to a possible discrepancy in magnitude between the two products.

4.1.3 Vortex data

With reference to the AEW structure illustrated in Fig. 2.10, vortices are commonly found to be embedded within the AEW structure in the tropical West African region. Therefore, it would be insightful to observe the vortices within the domain.

The vortex dataset is based on the detection of coherent features by velocity gradient tensor from 2-8 day bandpass-filtered wind fields of ERA5 reanalysis data and it is also compiled by the author of . However, the vortices identified are only based on the mathematical derivation, could be found over more places other than regions affected by AEW. Similarly, this structure of the dataset is following the framework suggested by Limbach et al. (2012). The vortices dataset does not solely represent those related to AEW. Therefore, the vortices have been filtered with the criterion of 5°-25°N, 60°W-30°E, cyclonic, westward propagating. It is expected that most of the vortices in this domain would have an association with the AEW dynamics. As suggested by Cornforth et al.
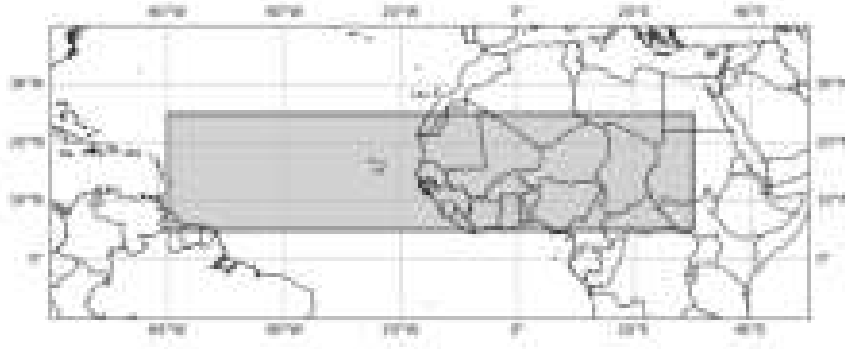
Figure 4.2: Domain of filtered vortices, lying with 5°-25°N, 60°W-30°E indicated by the shaded area

(2017), 850 hPa vortices are generally a good proxy of the possible location which depicts the development of thunderstorms and convective cells.

4.1.4 Other variables

In parallel to the ECMWF precipitation rate forecast dataset, several variables related to the moisture fields and the dynamics can be helpful for the comparison in order to investigate how the variables are performing in relation to AEW trough axes. The moist variables used include Total Column Water Vapour (TCWV), vertically integrated moisture divergence (VIMD), and 700hPa specific humidity (q700). As for other kinematic variables, 700hPa and 850hPa relative vorticity, and 600-925hPa vertical wind shear have been included. The wind shear is derived from 2-6 day bandpass-filtered zonal and meridional wind fields at the 600 and 925hPa level.

The following provides the definition of the necessary variables from ECMWF data source. To begin with the moisture fields, Specific humidity is the mass of water vapor per kilogram of moist air. Specifically, it can be useful to investigate the 700hPa level in relation to the jet level, a typical height for the transition between the SAL and moist monsoon layer.

$$q = \frac{m_v}{m_{\text{air}}}$$

where:

$$
\begin{aligned}
q &: \quad \text{Specific Humidity,} \\
m_v &: \quad \text{Mass of water vapor,} \\
m_{\text{air}} &: \quad \text{Mass of moist air.}
\end{aligned}
$$

Total Column Water Vapour (TCWV) refers to the integrated mass of gaseous water in the total column of the atmosphere over unit area. This parameter represents the area-averaged value for a grid box.

$$TCWV = \int_0^{z_{top}} q \, dz$$

where:

$$TCWV: \quad \text{Total Column Water Vapour,}$$
$$q: \quad \text{Specific Humidity,}$$
$$z_{top}: \quad \text{Top of the atmosphere.}$$

Secondly, another variable to include is the Vertically Integrated Moisture Divergence (VIMD). The vertical integral of the moisture flux is the horizontal rate of flow of water vapor per meter across the flow, for a column of air extending from the surface of the Earth to the top of the atmosphere. Its horizontal divergence is the rate of moisture spreading outward from a point, per square meter.

$$VIMD = \nabla \cdot \int q \mathbf{v} \, dz$$

where:

$$VIMD: \quad \text{Vertically Integrated Moisture Divergence,}$$
$$\nabla: \quad \text{Divergence operator,}$$
$$q: \quad \text{Specific Humidity,}$$
$$\mathbf{v}: \quad \text{Wind vector,}$$
$$dz: \quad \text{Differential height.}$$

In addition, for these moist variables, it is expected that the pattern might be highly influenced by the moisture availability based on the corresponding geographic locations for tropical West Africa. Areas in the south tend to have more available moisture because of their proximity to the ocean. The north-south pattern would not be pronounced in this regard. Therefore, ERA5 reanalysis datasets particularly on TCWV and Q700 are taken for the computation of the 30-year climatological average of each corresponding grid point, namely from the period of 1991-2020. This is done to mitigate regional dependence which is possibly overriding the synoptic signals.

Apart from the above, it would be useful to take several variables related to dynamics within the AEW to investigate its structural development based on the forecast data. Given that the wave disturbances lead to curvatures in the streamlines, relative vorticity at 700hPa and 850hPa level is taken, which can be related to northerlies and southerlies regime to a certain extent. Besides, another important element which drives strong convective activities over tropical West Africa is the presence of strong vertical wind shear (see the equation below). In practice, a low-level wind shear metric is derived from the difference of the 2-6 day bandpass-filtered zonal and meridional wind components between 600hPa and 950hPa levels.

$$Shear = \sqrt{(u_{600} - u_{925})^2 + (v_{600} - v_{925})^2}$$

4.2 Methodology

4.2.1 Wave trough properties

With the knowledge that AEW propagates from east to west along the AEJ and further explore the general properties of the wave trough tracks, a method is developed to find one of the most representative points from an individual WT. This representation is useful to calculate the wave trough propagation in each track, such as the propagating distance from east to west, lifetime and the propagating speed.

To obtain this point for WT representation, as illustrated from Fig. 4.3a from the edges of each WT, they were linearly interpolated between the two neighbouring edges, so as to create more interpolated points between the northernmost and southernmost edges. The middle point in terms of the latitude is defined as the mid-point of the WT. This is compared with other time steps throughout a track to observe the WT propagation. Furthermore, these midpoints of each WT in each time step were smoothened by three consecutive time steps, which deduces the black line. This helps reduce the effect of sudden jump between the two consecutive time steps.

The length of a track refers to the westward propagating distance of the wave trough. It was quantified by the distance between the longitudinal positions of the mid-points between the first and last time steps. The lifetime of a track is here defined as the difference between the first and last time steps given by the number of hours. As for the propagation speed, it is based on dividing the aforementioned length divided by the lifetime.

The binary classification of a WT, whether it is situated over land or ocean, is based on counting the number of interpolated points over land / ocean, as shown in Fig. 4.3a. Each point is individually classified for its location over land or ocean by a land-shape mask from the Python Cartopy library. The larger fraction will determine the categorization of WT. For example, from Fig. 4.3a, since all interpolated points at the edges are situated over land, this WT is thus classified as a WT over land. As for the others, if more than half of the interpolated points are over land and the rest is over the ocean, this WT is also classified as a WT over land. If the fractions of points over land and ocean are equal, this would be determined by the midpoint of the two middle points. For instance there are 26 interpolated points. If the fraction over land and ocean is the same, the classification of WT over land or ocean will solely depend on the properties of another mid-point between the middle two consecutive interpolated points, i.e. another mid-point between the 13th and 14th in this case.

From the wave trough attribute, for each edge within a wave trough, the intensity value of a WT feature is defined as the averaged CV along all edges of the wave trough as an estimate. As seen from Fig. 4.4, a probabilistic density function was computed from the wave trough over the period of 2002 and 2022, and two thresholds have been drawn namely, the lower quartile (Q1) with the
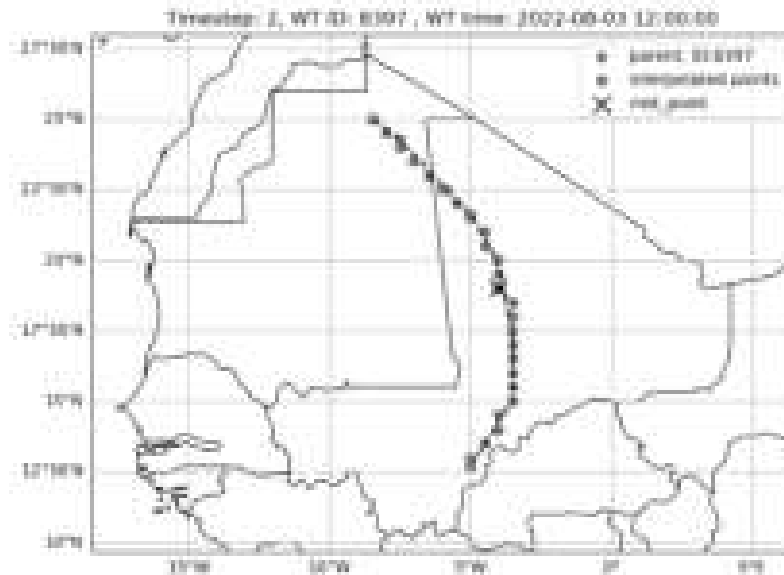
(a)
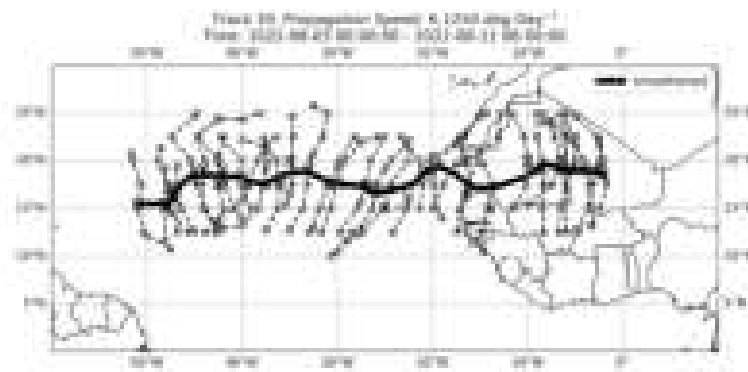
(b)

Figure 4.3: Illustration of mid-point definition from a wave trough and calculation of wave trough properties. (a) Interpolating the points (blue dots) along a parent node wave trough edge (red dots), defining the mid-point of a wave trough feature (cross) (b) Track of centroid indicated by the black line.

intensity of 6.18 x $10^{-6}s^{-1}$ and upper quartile (Q3) with the intensity of 1.615 x $10^{-5}s^{-1}$. With these two cutoff in mind, the classification of all WT in the later analysis could be divided into three groups, namely strong WT with their intensity values greater than or equal to Q3, weak WT with their intensity values smaller than Q1 and the rest belongs to the "medium" group which has the intensity value lying within the interquartile range of the 21-year WT intensity distribution.

Taking a look at an example as shown in Fig. 4.5, a wave trough lifetime does not always follow a smooth development of intensity like a normally-distributed curve, but it can get quite random. This could be attributed to multiple local effects for each individual wave trough propagating from east to west, whether they were at which latitude bands, the terrain they passed by and also the strength of the synoptic forcing due to the energy conversion. In this regard, following simply a wave trough lifetime might not be representative for its strength, but instead by individually a WT feature's intensity value at different time steps. Each of the WT feature identified at each time point would
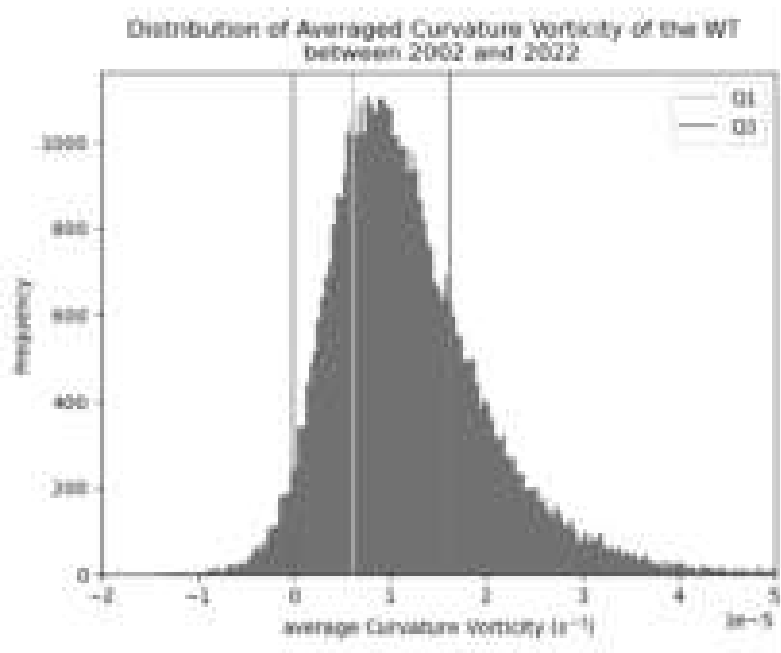
Figure 4.4: Distribution of Average Curvature Vorticity of WT between 2002 and 2022, two static thresholds are drawn, namely the upper (Q3) and lower (Q1) quartiles.

be categorized individually based on the thresholds. Wave troughs with intensity values within the red (green) box belong to the stronger (weaker) wave trough group for the later composite rainfall distributive curve calculation. The right upper subplot display the progression of this certain WT in degrees . This measure represents the length extent of the wave trough, which could tell how the wave trough is stretching or shrinking throughout its lifetime. There is no observable relationship between the averaged curvature vorticity of the wave trough and its length extent. As for the right lower subplot, it shows the east-to-west propagation for this particular wave trough example which has the same structure as in 4.3b.

4.2.2 Precipitation aligning to a wave trough axis

In order to investigate any pattern of a certain variable (e.g. precipitation rate) relative to the wave trough axis, a rectangular box was drawn to re-grid precipitation field. As depicted in Fig. 4.6b, the box was structured with a length grid of relative longitude from -15° to +15° from the WT edges, and the height grid of the latitudinal position difference between the northernmost and southernmost edges. The precipitation was then plotted relative to the WT axis (Fig. 4.6c). Then a conditionally-averaged precipitation relative to WT relative longitude was computed over the bins with a precipitation rate greater than 0.1 mm hr^{-1} within this latitudinal extent. This allows the filtering out of a lot of grid data which has no rainfall at all but extracting regions with a considerable amount of rainfall magnitude out. This curve of precipitation relative to each wave trough axis versus the relative longitude coordinate could be further manipulated with more wave troughs. The following plots illustrate the method.
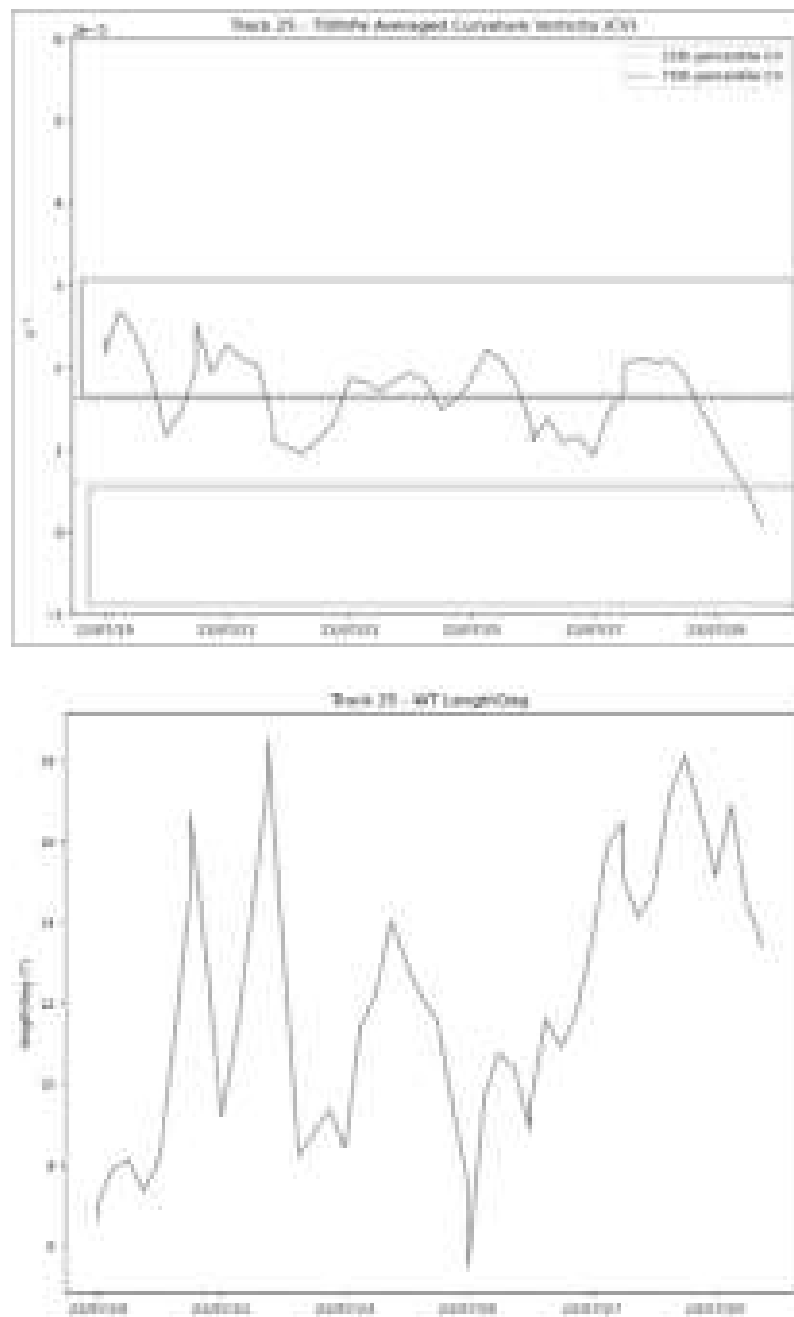
Figure 4.5: An example illustrating (a) the intensity, (b) length of the WT in degrees (bottom) of a certain wave trough lifetime. (a) The red and green boxes category the WT features belonging to the WT category >Q3 and <Q1 respectively.

The above method has been applied to all wave trough features so as to obtain a similar-structured precipitation curve from each wave trough. For precipitation, to eliminate some ambiguous and noisy signals from the dataset, precipitation rate smaller than 0.1 mm hr^{-1} from individual grid is filtered out conditionally for the mean value computation. These distributive curves could be grouped based on different criteria, such as over land or ocean, or the category according to the intensity thresholds, for a composite distribution of the corresponding WT group. The precipitation forecast field also varies with different forecast time steps, aligning to the time point of ERA5-derived WT axes observed to perform the composite analysis. With this method, it is

(a)

(b)

(c)

(d)
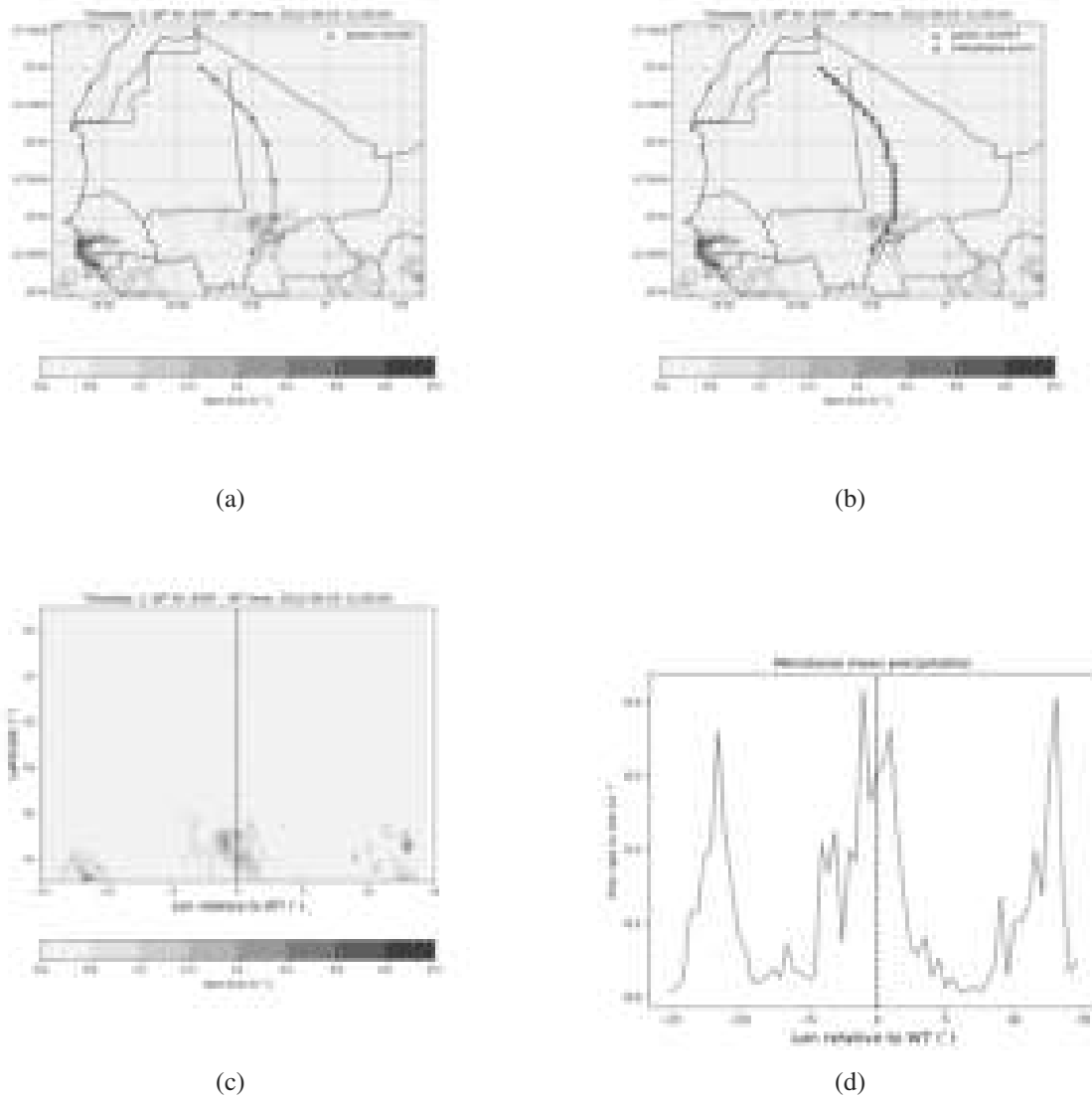
Figure 4.6: Computing precipitation relative to wave trough axis. (a) Overlaying the precipitation field on a map (b) Interpolating the points along a WT, similar to Fig. 4.3a (c) Regridding the precipitation field into relative longitude of -15° to +15° from the WT axis (d) Perform a meridional average over the latitudinal extent of the WT. Particularly, this method has indeed been extended to

then insightful to observe how the overall pattern of such alignment of precipitation field and other variables aligning to a wave trough, would alter or be lost for longer lead time hours. The lead time computation was done only up to the first five days, namely 120 hours. Figure 4.7 illustrates the lead time composite.

4.2.3 Precipitation aligning to a vortex center

Another area of investigation focuses on associating multiple variables to vortices centers, such as precipitation rate, finding the spatial pattern of these fields relative to each individual vortex. Fig. 4.8 illustrates an example. For all the filtered vortices within the scope of interest over West Africa and tropical Atlantic, each vortex has a feature ID and time. As seen from Fig. 4.8a, to align with
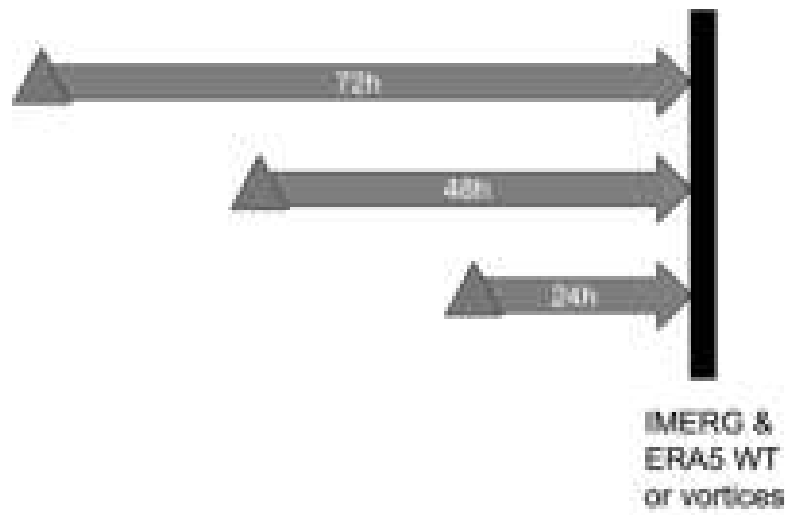
Figure 4.7: Illustrating the lead time alignment of the forecast field, i.e. precipitation rate with the WT for composite analysis. A specific point of forecast data with a certain lead time. The black strip is the time point when different wave trough features from ERA5 are tracked. Correspondingly by the method shown in Fig. 4.6, precipitation field from IMERG or ECMWF could be aligned. Similarly, the forecast field run at earlier lead time hours (red triangles) to predict the time point pattern when the wave troughs were tracked individually (black strip), were grouped together.

the precipitation field, the coordinates of each of the vortex is rounded up to the nearest gridded coordinates (following the 0.5° x 0.5° grid from the precipitation rate field).

Then a square of the precipitation data is drawn with the length grid of relative longitude from -15° to +15° and also the width of relative latitude from -15° to +15°. This creates another matrix as shown in Figure. 4.8b. With this 2D map of precipitation associated with one vortex center, we could further compute the same for the other vortices centers and perform an average value for each relative 2D grid. Similarly each vortex center could be further classified into either over land or ocean. The average of different vortex-associated rainfall could be based on the vortices' characteristics. Other lead time of the precipitation field were also taken to align with the ERA5-derived vortices centers as well.

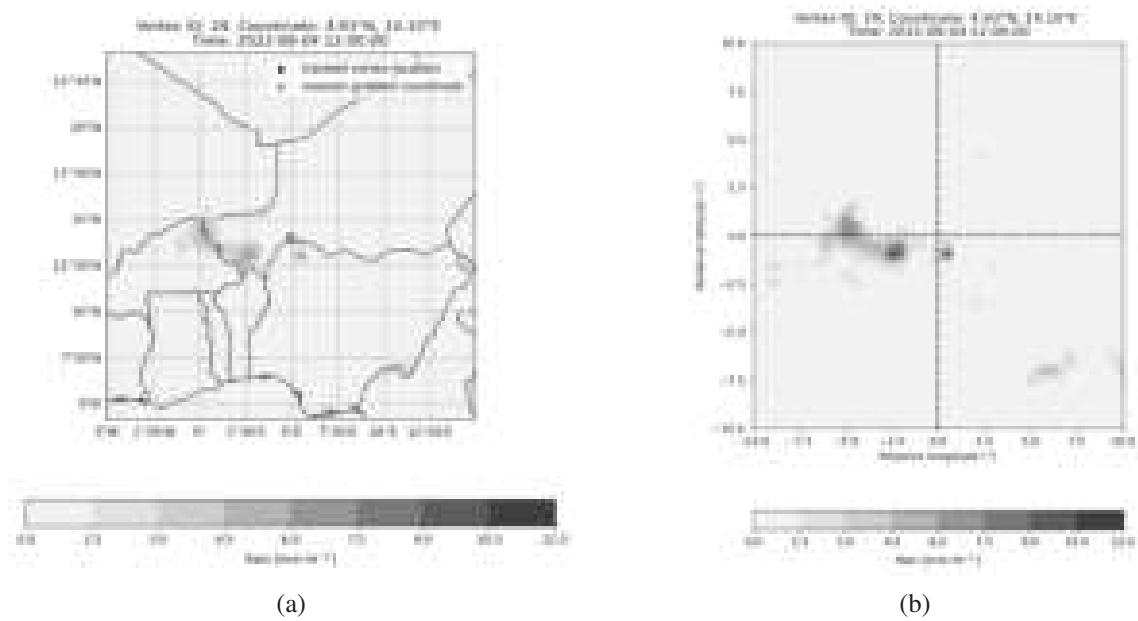(a)   (b)

Figure 4.8: An example illustrating the computation of precipitation relative to vortice centers. (a) Overlaying precipitation field on a map. The coordinates of a vortex center (black dot) are rounded off to the nearest gridded coordinate (blue dot) (b) Regridding the precipitation field into a rectangular box of relative longitude of -15° to +15° from the longitude of a vortex center and similarly relatude latitude from its corresponding latitude.

5 Results

This chapter presents the research findings, after performing the steps described in the methodology section in Chapter 4. The analysis of the result would be presented in the following sequence. Firstly, the dynamic properties of the wave troughs and the vortices will be presented. Secondly, the composite pattern of WT-precipitation coupling will be shown, and followed by vortex-precipitation association composite. Lastly, similar techniques applied to other meteorological variables will also be illustrated.

5.1 Dynamic properties

5.1.1 Wave troughs

The following table shows the simple statistics computed from the wave trough dataset. From the period of 2002 and 2022, the number of tracks per year lies in the range of 60-80. Based on Table 5.1, the average lifetime of a track is 109.46 hours, roughly 4-5 days. In average, the sample of AEW is propagating for about 31.80° longitude. The average speed is at $6.90°\text{day}^{-1}$. Fig. 5.1a displays a histogram of probabilistic density function of propagation speeds of the wave trough in the period of 2002 and 2022, while Fig. 5.1b shows a histogram of propagation speed for the individual year.

The above computed statistics agree well with known AEW characteristics. This gives a confidence toward the reliability of the wave trough dataset representing AEW. The focus of the project is to investigate, in particular, the AEW pattern in 2021 and 2022 and how the associated precipitation forecast is having a relation with AEW. The numbers of AEW tracks in 2021 and 2022 are found the highest in August, namely 22 tracks (Fig. 5.2).

In addition, the overall edge position, which represents points of zero curvature vorticity anomaly advection along the wave trough has been also explored. From the appendix section with Fig. 7.1, the geographical distribution of the overall position of the edges of the WT is drawn. This serves as a reference of how they are situated over which latitude bands over the geographical scope of interest, namely the tropical Africa and Atlantic region. Since AEW propagates along AEJ, the shifting of the whole distribution of edges could roughly coincide with the oscillation pattern of AEJ during the summer season.

Year	No. of Tracks	No. of Graphs	Lifetime (hours)	Length (°)	Speed (° day^{-1})
2002	65	2435	111.69	35.24	7.63
2003	73	2561	102.90	28.56	6.63
2004	63	2386	114.29	33.06	7.00
2005	64	2479	114.47	29.61	6.19
2006	63	2481	118.19	33.88	6.78
2007	63	2364	107.81	29.79	6.77
2008	63	2510	116.76	33.25	6.93
2009	72	2480	101.92	29.18	6.79
2010	70	2433	112.20	32.90	6.91
2011	62	2402	107.23	30.68	7.01
2012	67	2441	109.25	31.94	7.12
2013	66	2392	106.00	31.24	7.20
2014	61	2459	112.92	33.22	6.92
2015	57	2223	99.16	29.82	7.27
2016	71	2533	105.04	29.46	6.76
2017	65	2545	116.95	31.73	6.44
2018	60	2392	110.50	31.41	6.73
2019	65	2403	101.91	28.95	6.73
2020	69	2445	98.78	29.91	7.31
2021	67	2527	116.51	35.11	7.35
2022	76	2728	114.16	32.01	6.68
Average	67	2483	109.46	31.80	6.90

Table 5.1: Simple statistics of wave trough tracks, including lifetime, tracked length, track speed in the period of 2002 and 2022
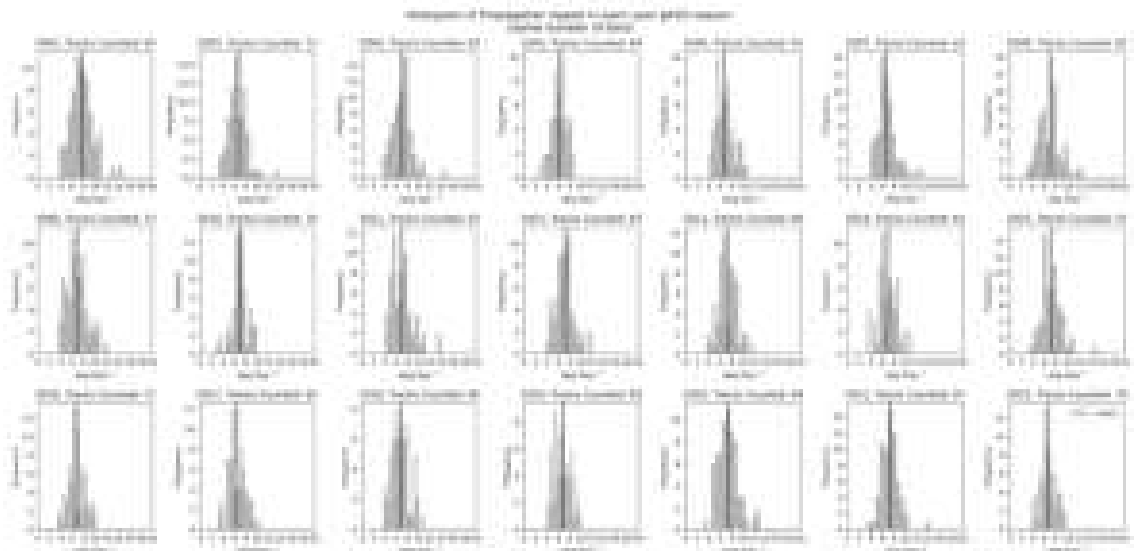
5.1.2 Vortices

Apart from the WT dataset, this part gives a brief summary of the vortex dataset analysis. Similar to Fig. 7.1, the same configuration has been used to analyze the spatial distribution of vortices. This can be referred from Fig. 7.2 and 7.3 based on the corresponding pressure level. In contrast to Fig. 7.1 previously described, the drawn histogram of vortice locations is noisier, which could extend to the southern hemisphere.

Moreover, the vortices have been specifically selected for later composite analysis namely based on the scope of interest within the tropical domain and required cyclonic features of vortices. Table 5.2 shows the number of filtered vortices in 2021 and 2022, and they are also classified if located
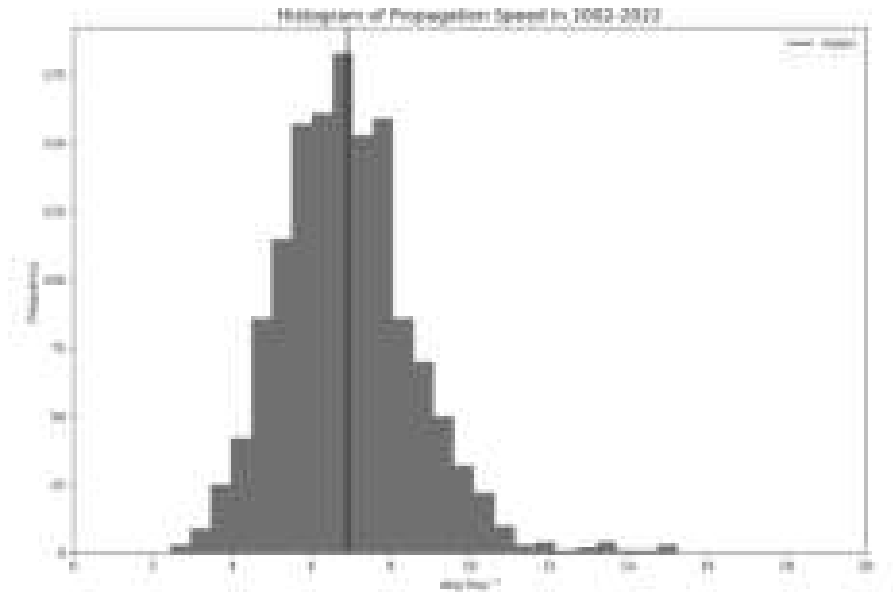
(a)

(b)

Figure 5.1: Histogram of WT propagating speed in deg Day^{-1} (a
in the whole period of 2002-2022 (b) for individual year

over land or ocean. A normal distribution for vortices with positive PV could not be directly
approximated, while positive PV is favourable for convection initiation (not shown).

5.2 Aligning precipitation field to WT

The relative positioning of the precipitation plays a crucial role in its interaction with African
Easterly Waves (AEWs), and this relationship can vary for several reasons. For instance, differences

<center>(a)   (b)</center>
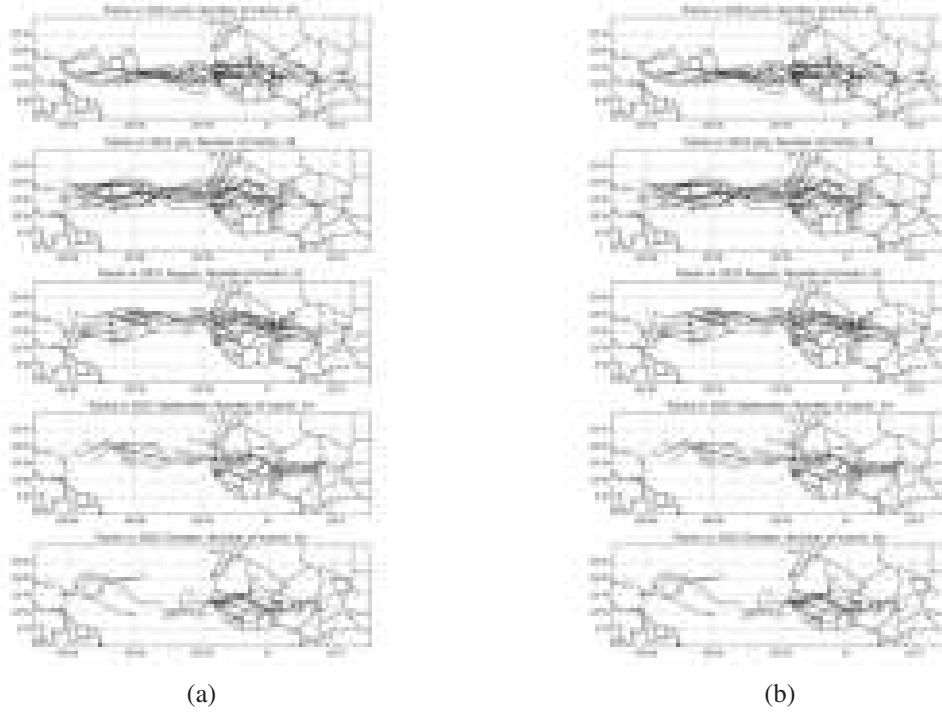
Figure 5.2: AEW monthly tracks in (a) 2021 and (b) 2022, as represented by the westward propagation of mid-point of a wave trough feature as illustrated in Fig. 4.3. The number of tracks per month is indicated from the title of each subplot map. The same track is shown in the maps of two months if the whole period of its lifetime covers consecutive two months.

Filtered vortices	2021	2022
All	3793	3618
Land	1999	1857
Ocean	1794	1761

Table 5.2: Number of filtered vortices in 2021 and 2022, and over land or ocean, based on the criteria of 5°-25°N, 60°W-30°E, cyclonic, westward-propagating

in the strength of the wavetrough can lead to varying degrees of modulation in precipitation patterns. Additionally, the positioning of the WT over different geographical regions is influenced by distinct environmental conditions, with significant phase disparities often observed between land and ocean areas. Furthermore, improvements in moisture physics or changes in dynamics may contribute to discrepancies between the representation of AEW-related precipitation in 2021 and 2022. Bearing these factors in mind, a composite analysis of the precipitation field, aligned with all WT axes, has been conducted, and the findings will be presented subsequently.

As shown in Fig. 5.3, as represented in the initial condition, when viewing at the first and second column, more intense WT is associated to stronger precipitation rate, especially at the peak point that can be observed ahead of the WT. Meanwhile the composite of weaker WT (<Q1) yields a flatter distribution of associated precipitation. While comparing the two years, for stronger WT (>Q3) over land, the peak of 2022 is spread wider over the relative longitude and pushed a bit more further ahead, spanning from -7.5° to -2.5° relative longitude, than 2021 which the peak stays at
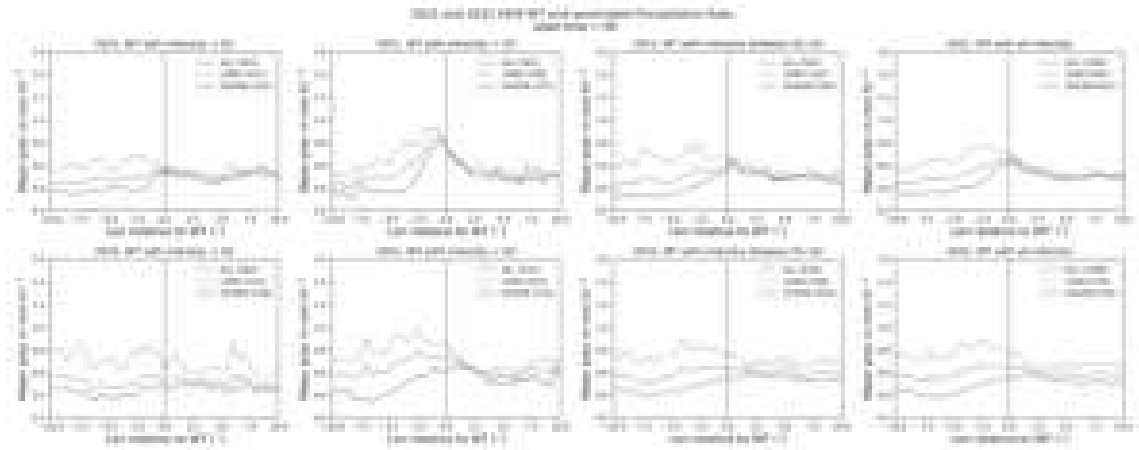
(a) Precipitation rate based on ECMWF forecast, aligning to WT axes in 2021 and 2022
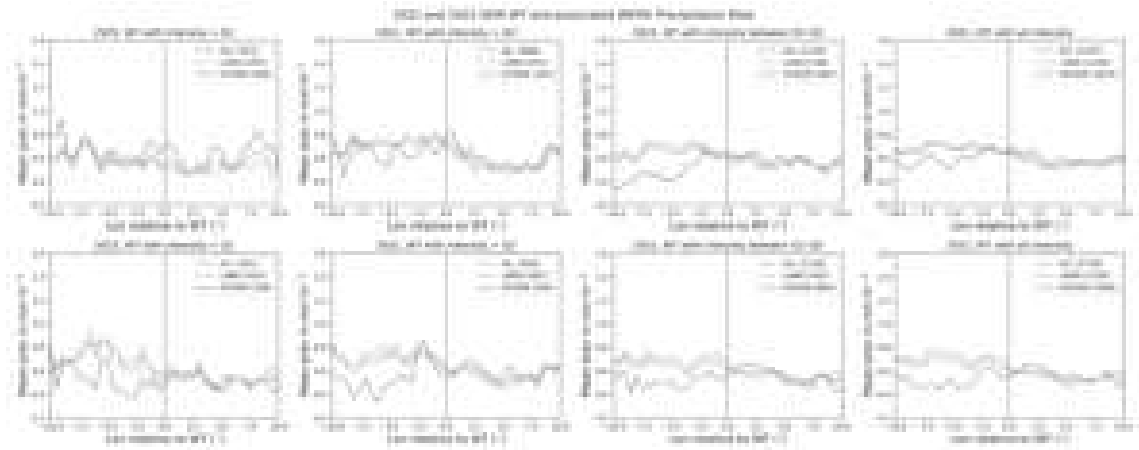
(b) Precipitation rate based on IMERG product, aligning to WT axes in 2021 and 2022

Figure 5.3: Results of the average precipitation rate in mm hr^{-1} aligning to WT axes by composite (The red line is the remapped WT axis for all WT in the compoiste) from (a) ECMWF forecast and (b) IMERG satellite-derived products. The two rows in each subplot represent the precipitation aligning to WT patterns in 2021 and 2022 respectively. The four subplots indicate the four different categories in grouping the WT, from left to right, namely WT with intensity smaller than the lower quartile Q1, WT with intensity greater than the upper quartile Q3, WT with intensity lying between Q1 and Q3 and WT with all intensity values. The intensity thresholds are drawn based on the intensity distribution from all tracked WT in the period of 2002 and 2022. In each subplot, the three lines represent the composite of all WT (green), WT over land (orange) and WT over ocean (blue). The bracketed value is the sample size of WT features falling into corresponding category, which is the number of precipitation distribution curve based on the number of WT falling into the location and WT intensity category

around -1°. In general, it is observed that the area of the curve ahead of WT enclosed by the orange curve (land WT) is bigger than that of ocean WT. This implies that precipitation amount associated to land WT is greater than that of ocean WT ahead of WT axis in the composite. Meanwhile the precipitation peak of land WT has a precipitation peak (>0.8 mm hr^{-1} located more ahead of WT axis, while that of ocean WT has its peak (0.8 mm hr^{-1}) closer to the WT axis. From the labels of each subplot, the bracketed values indicate the WT sample size included in this composite curve. The fourth column includes all WT samples for the composite. A larger sample size yields a relatively smoother distribution in comparison with the other three columns, namely the group of WT with intensity values <Q1, >Q3 and lying between Q1-Q3 respectively. For the last two

columns, it is observed that a stronger wiggling pattern is observed over land WT of the composite. This is even obvious, especially before the WT axis. In 2021, there is a rather small distinction in the magnitude of precipitation values after the composite over land and ocean behind the WT axis, while it is still observable that the composite average values of precipitation over land WT is bigger than those of ocean WT.

While the magnitude of the forecast initial condition shown in Fig. 5.3a is unable to show a direct agreement with that from the observational precipitation data from IMERG as in Fig. 5.3b given an inconsistent nature of different rainfall products, forecast data have shown a smoother pattern, but the observation looks more jumpy, but they still give the remark of the distinctive WT-precipitation phase relationship given by the difference of the peak locations of blue and orange lines, corresponding WT over ocean and land respectively. The limitation is still that the magnitude difference in precipitation association between those over land WT and ocean WT based on the IMERG data is not obvious. They are lying in the range of 0.4-0.8 mm hr^{-1}. The difference in the precipitation amount ahead of WT between land and ocean is more observable in the last column, as represented by the orange and blue lines respectively.
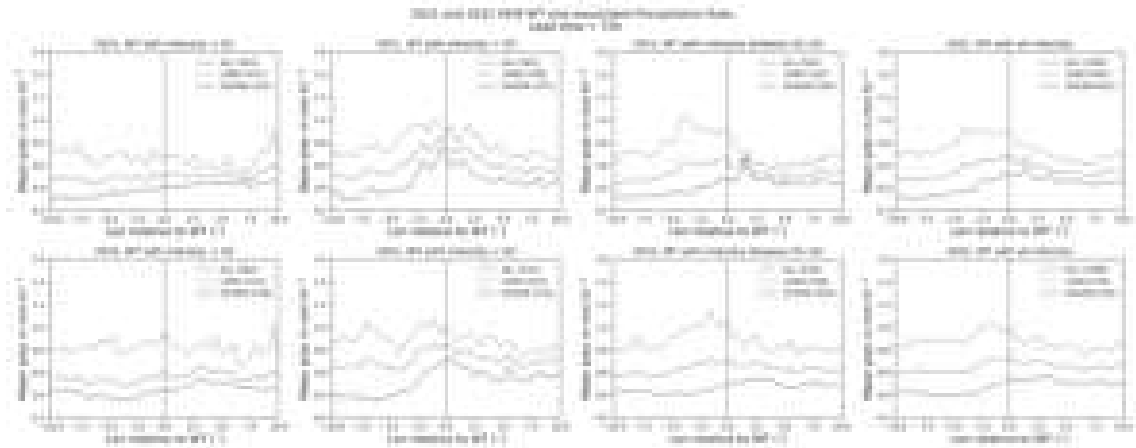
(a) Similar to Fig. 5.3, but with lead time = 72 hours
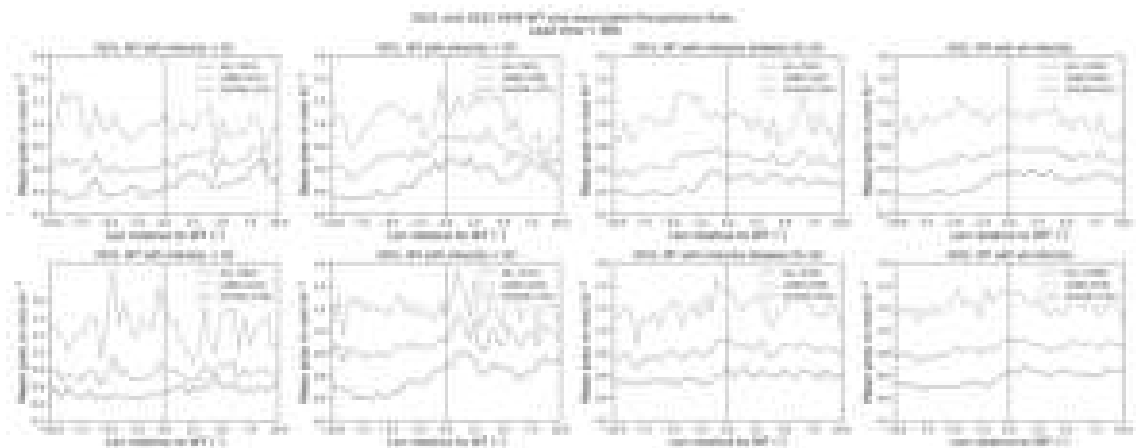
(b) Similar to Fig. 5.3, but with lead time = 96 hours

Figure 5.4: Results of the average precipitation rate aligning to WT axes composite, with lead time (a) 72h (b) 96h, similar to Fig. 5.3

While observing the composite of longer lead time, the magnitude of precipitation is observed to be increasing simultaneously. The aforementioned pattern can roughly be seen until 72h but then the distribution becomes flatter (between ahead or behind the composite WT axis). From the model precipitation forecast, WT and precipitation have much weaker coupling in later stages. There is hardly any pattern observed with lead time greater than 96 hours (Fig. 5.4b). There is no obvious distributive patterns of precipitation ahead or behind the WT axis. There is a stronger fluctuation observed for precipitation over land WT, as represented by the orange lines. The only pattern remained observable is that precipitation rate associated to land WT is greater than that over ocean WT. It can be concluded that the WT-precipitation profiles have been blurred out between 3 to 4 day lead time. A set of lead time composite for 24 and 48 hours is provided in the Appendix section.

5.3 Associating precipitation field with vortex centers

Other than analyzing the coupling of WT and precipitation field, the relationship between the precipitation field and vortex centers will be described in this section. Based on the composite analysis, this method shows that the relative position of the precipitation field associated to vortex centers, by observing the spatial distribution from four quadrants relative to the composite vortex centers. This is also equivalent to the geographical directions. The left (right) half belongs to the west (east) side of the composite vortex center.

In addition to examining the coupling between the WT and precipitation patterns, this section will delve into the interplay between precipitation fields and vortex centers through spatial composite analysis in 2-dimensional map representation. Specifically, by categorizing the precipitation field into four quadrants surrounding the composite vortex center, we discern the relative positioning of precipitation in relation to the vortex. In this illustration, the left (right) half corresponds to the western (eastern) side of the composite vortex center. Through this approach, we gain insights into how precipitation patterns are distributed with respect to vortex centers, shedding light on their spatial dynamics and potential influence on atmospheric processes.

As shown in Fig. 5.5, both ECMWF and IMERG precipitation fields show an underlying contour fields with less precipitation in the north and more precipitation in the south, which is highly influenced by the geographical setting over the tropical Africa domain. The north is always drier than the south. Overlaying this background spatial pattern, the eccentric contours of precipitation exhibit an notable association of the precipitation field with the vortices. From (a), the peak of the composite in 2021, as labelled by the black cross, is well centered at the point where the zero relative latitude and zero relative longitude meet. This might be highly contributed by oceanic vortices. In 2022, it is observed that the rainfall peak is situated at the west side of the zero relative longitude axis. Extending the analysis to IMERG data for further comparison, the rainfall peaks, no matter situated over land or ocean, are mostly situated slightly ahead of the vortices, namely at the southwest quadrant. In this case, when comparing the initial condition of the precipitation field from the forecast, namely taking its initial condition, with IMERG, there is a better agreement
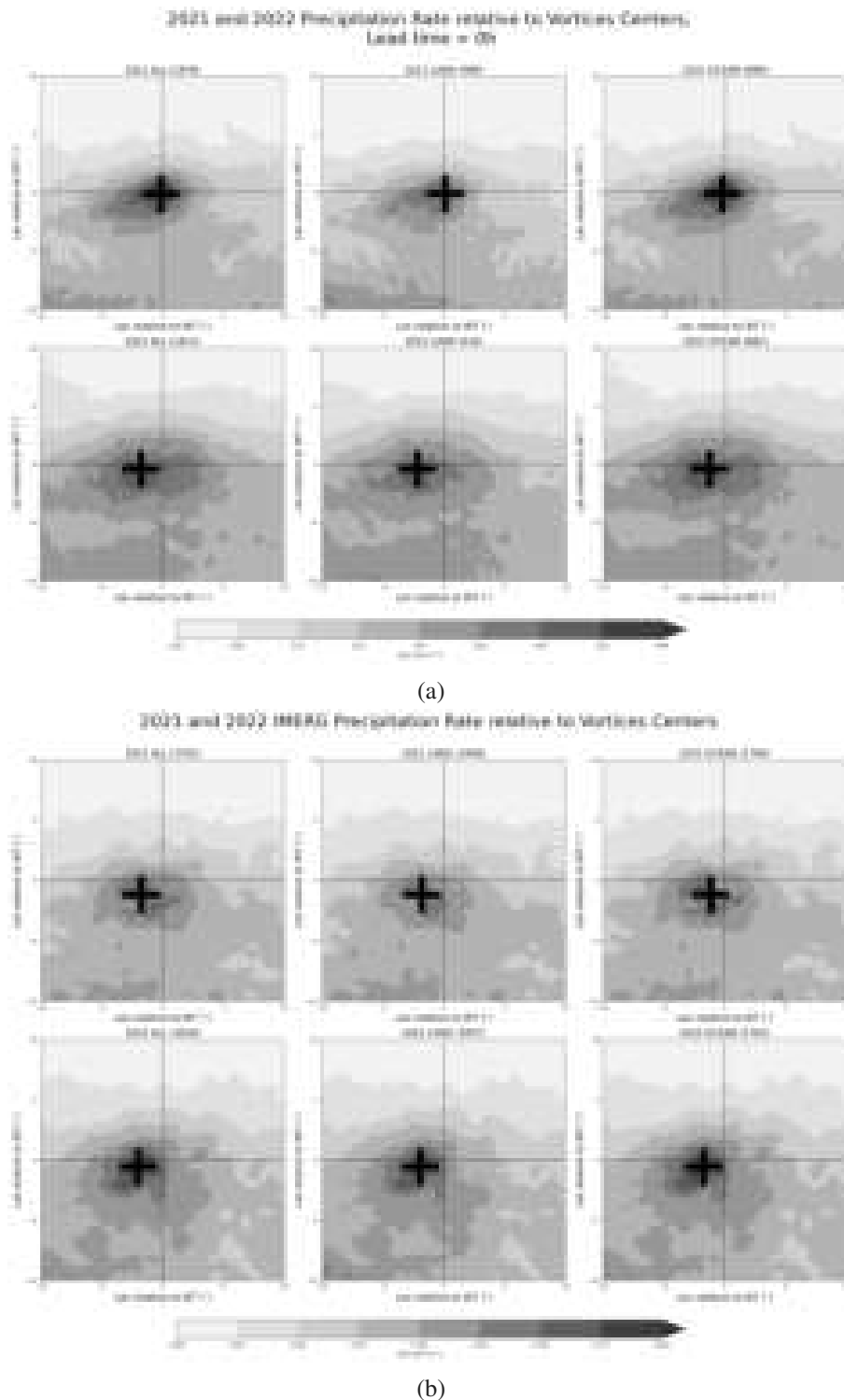
(a)

(b)

Figure 5.5: (a) Composite analysis of average precipitation rate associated to vortex centers in 2021 (first row) and 2022 (second row) of ECMWF forecast with lead time 0 hour. The first, two and third column represents the association of precipitation rate with all vortices, or composite of those vortices located over land and ocean respectively. The bracket in each subheading marks the sample size of vortices included. The black cross indicates the location where peak precipitation is observed. (b) Similar to (a), but using IMERG precipitation field with also 6-hourly temporal resolution.

in terms of the location of precipitation peak in the latter year. Both the forecast field and the observation precipitation field in 2022 has a peak located slightly west of the center.

(a)

(b)
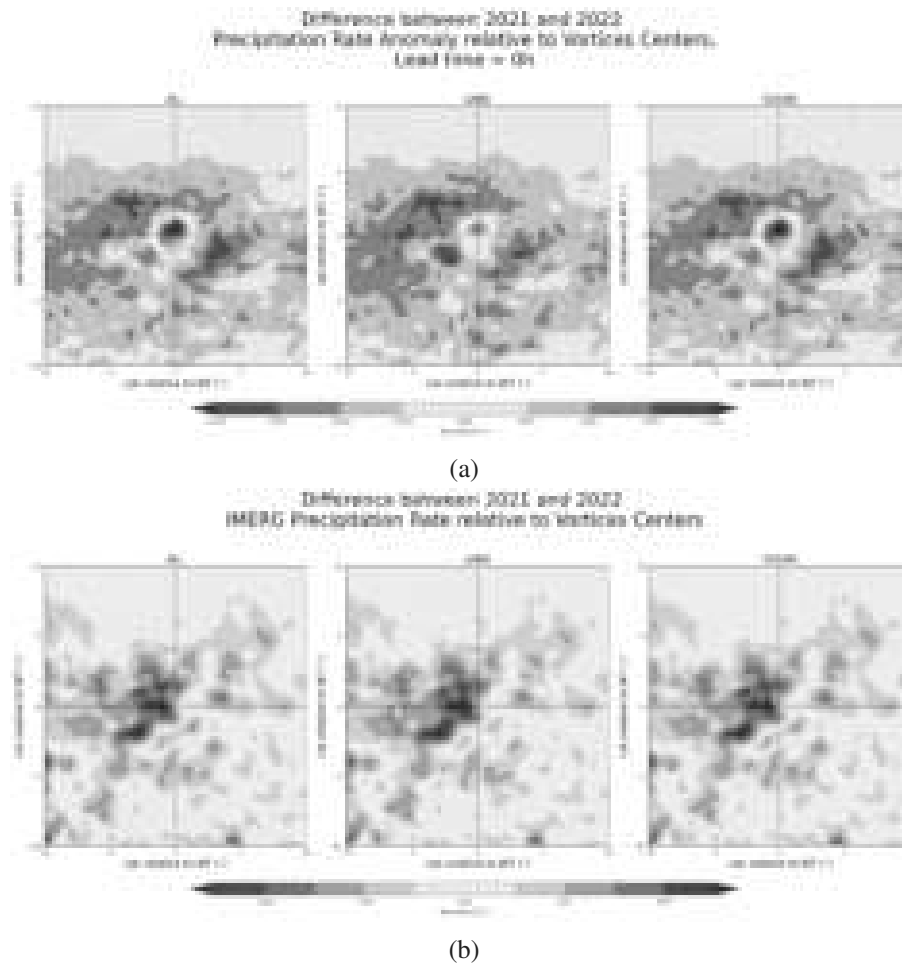
Figure 5.6: The difference in precipitation rate between 2021 and 2022 based on the same configuration of Fig. 5.5. This is calculated by the subtraction 2022 from 2021. Red (blue) colour indicates 2022 has less (more) rainfall than 2021. (a) ECMWF Forecast data (b) IMERG data

Fig. 5.6 compares the precipitation rate in this vortex association framework between the two years. The difference between 2022 and 2021 is significant at the center of the composite. 2022 is observed to be yielding higher precipitation amount at the west from the center but overall more widespread precipitation away from the center, represented by the blue patches surrounding the red patched center. The red patch indicates a strong centering of precipitation peak in 2021. In contrast, as for IMERG, from Fig. 5.6b, the precipitation peak is indeed located at the west of the zero relative longitude axis, lying at the range of 0 to -3 degree relative longitude. The pattern is similar no matter for all, land or ocean. This could be attributed to the difference in the actual dynamics between the two years, which leads to a inherited position different of the peak precipitation.

As opposed to the previous plots with shorter lead time, by observing the composite analysis of precipitation with longer lead time, from Fig. 5.7, the eccentric peaks are becoming less obvious with longer lead time, especially comparing the patterns with lead time 72 or 96 hours. From Fig. 5.7a, the eccentric peak is still weakly observable in 2021 especially for the composite of all vortices and ocean vortices. The precipitation associated to land vortices is observed to have less stronger eccentric patterns. This implies that there is a weak association between vortex centers and precipitation starting from 4 day lead time ahead in the composite, which would also be similar to the lead time barrier where WT-precipitation phase relationship is experiencing.
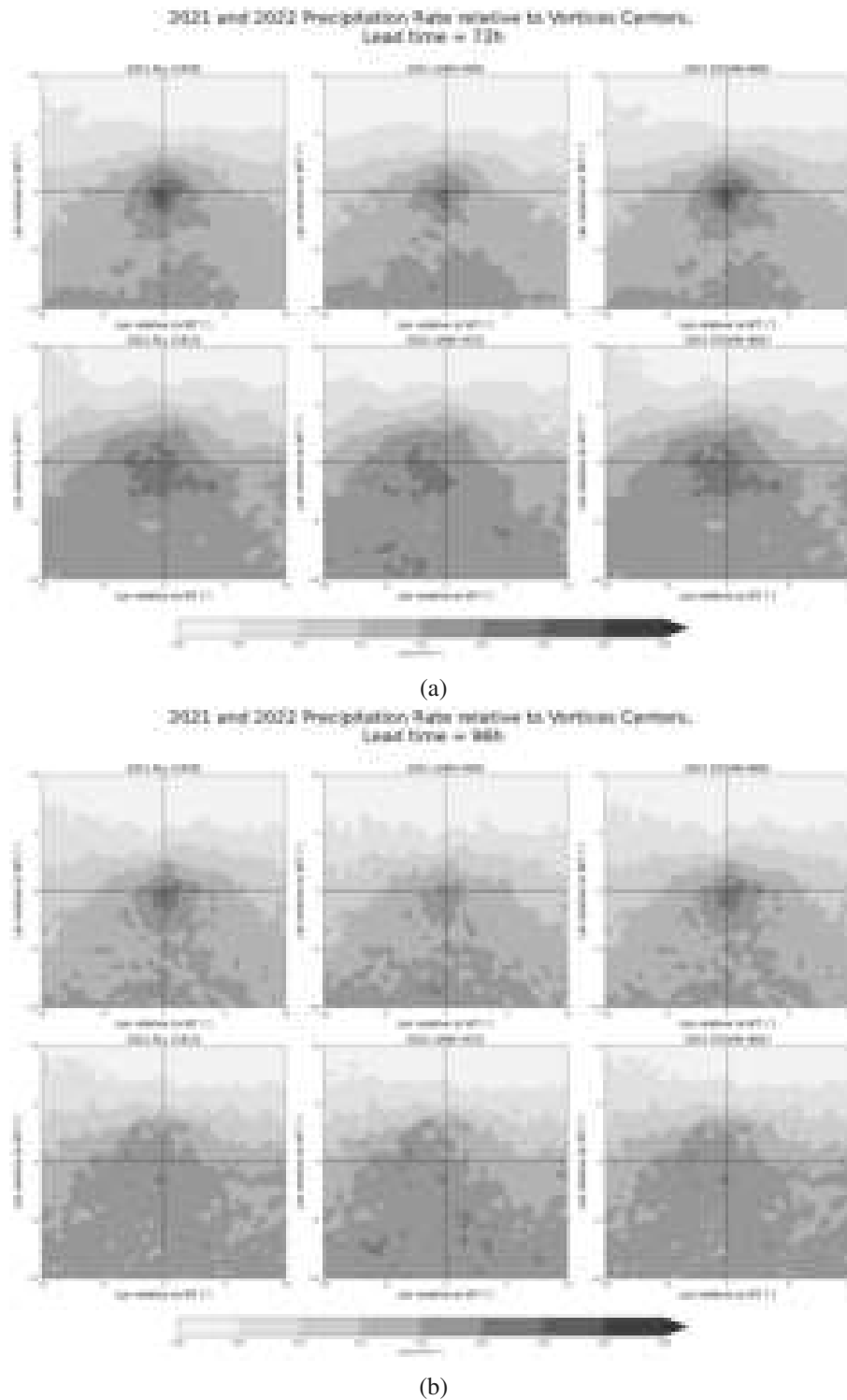
(a)

(b)

Figure 5.7: Composite analysis of the average precipitation rate associated with the vortex centers in 2021 (first row) and 2022 (second row) of ECMWF forecast. Similar to Fig. 5.5 but with lead time (a) 72h (b) 96h

5.4 Aligning other variables to WT

The same WT coupling methodology has been applied to other relevant variables of the ECMWF forecast output, which have been mentioned in Section 4.1. This section aims at providing a similar analysis as precipitation to other variables in this composite analysis associating to WT. It would be

beneficial to illustrate environmental conditions within AEW in the two model versions, to compare how their patterns are relatable with the rainfall fields in this framework.

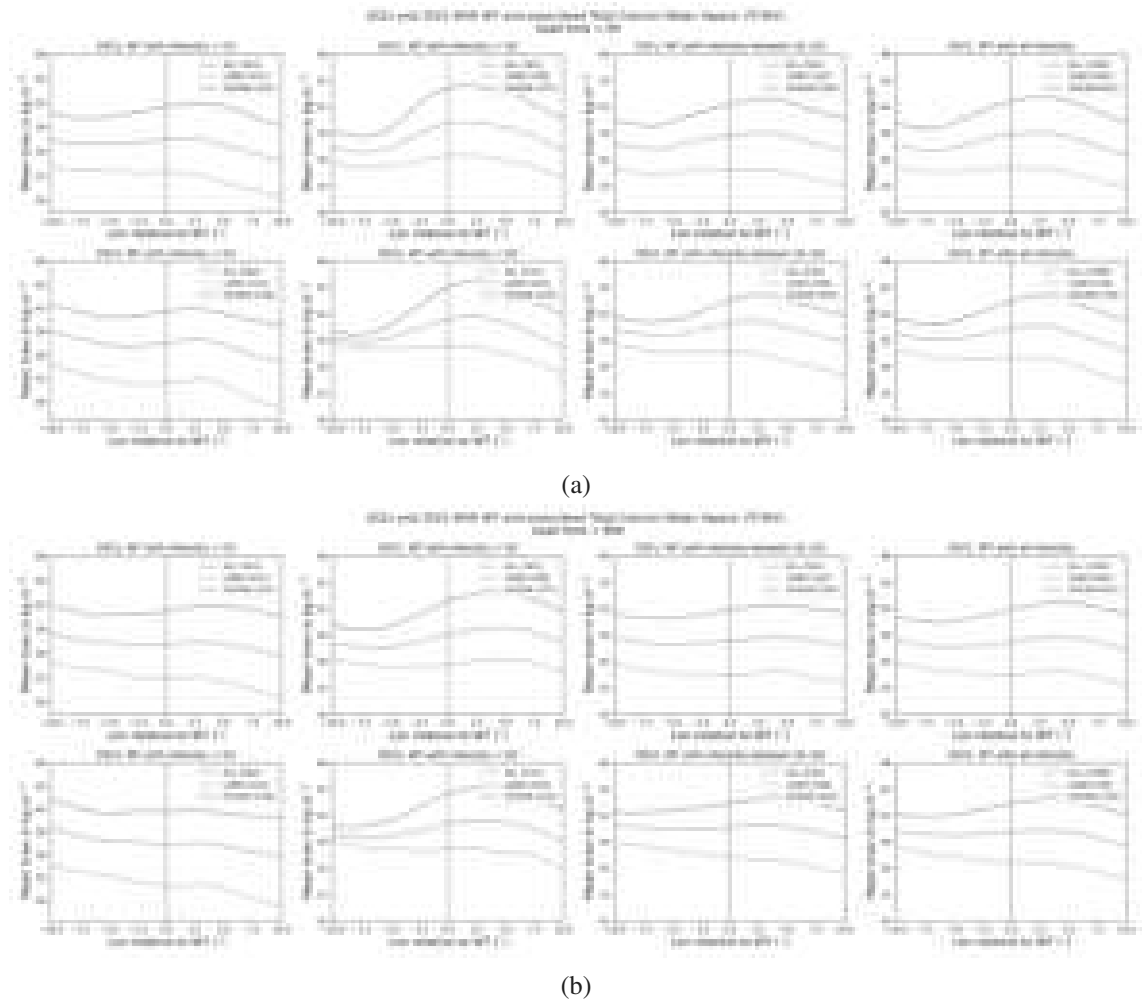## 5.4.1 Total Column Water Vapour

(a)

(b)

Figure 5.8: Similar to Fig. 5.3, results of the average Total Column Water Vapour (TCWV) aligning to all corresponding WT axes by composite with lead time (a) 0 hours (b) 96 hours

As observed in Fig. 5.8, based on the initial condition, higher TCWV values are associated with stronger WT, peak TCWV magnitude is situated closer to the wave trough or slightly behind, while weaker WT has a flatter distribution. No matter which WT strength categories, the composite plots for the four columns show smoother curve even having the same sample size of WT as the WT-precipitation alignment. TCWV distribution curves for all categories of WT strengths over land WT have generally lower magnitude than that over ocean WT, which is intuitively representing more moisture found in the air over ocean than over land, land WT has TCWV peak ahead of WT axis or into WT, ocean WT has precipitation peak more at the WT axis or behind, a converging point between land WT and ocean WT for >Q3 ahead of WT. The difference in the magnitude of TCWV over land WT between weak and high intensity WT is bigger in 2022 and this is obvious specifically ahead of WT axis, the value is considerably higher for stronger WT than weaker WT

in 2022. This converging point is roughly relatable in the WT category within Q1-Q3 and all. A hypothesis will be proposed in the later discussion.

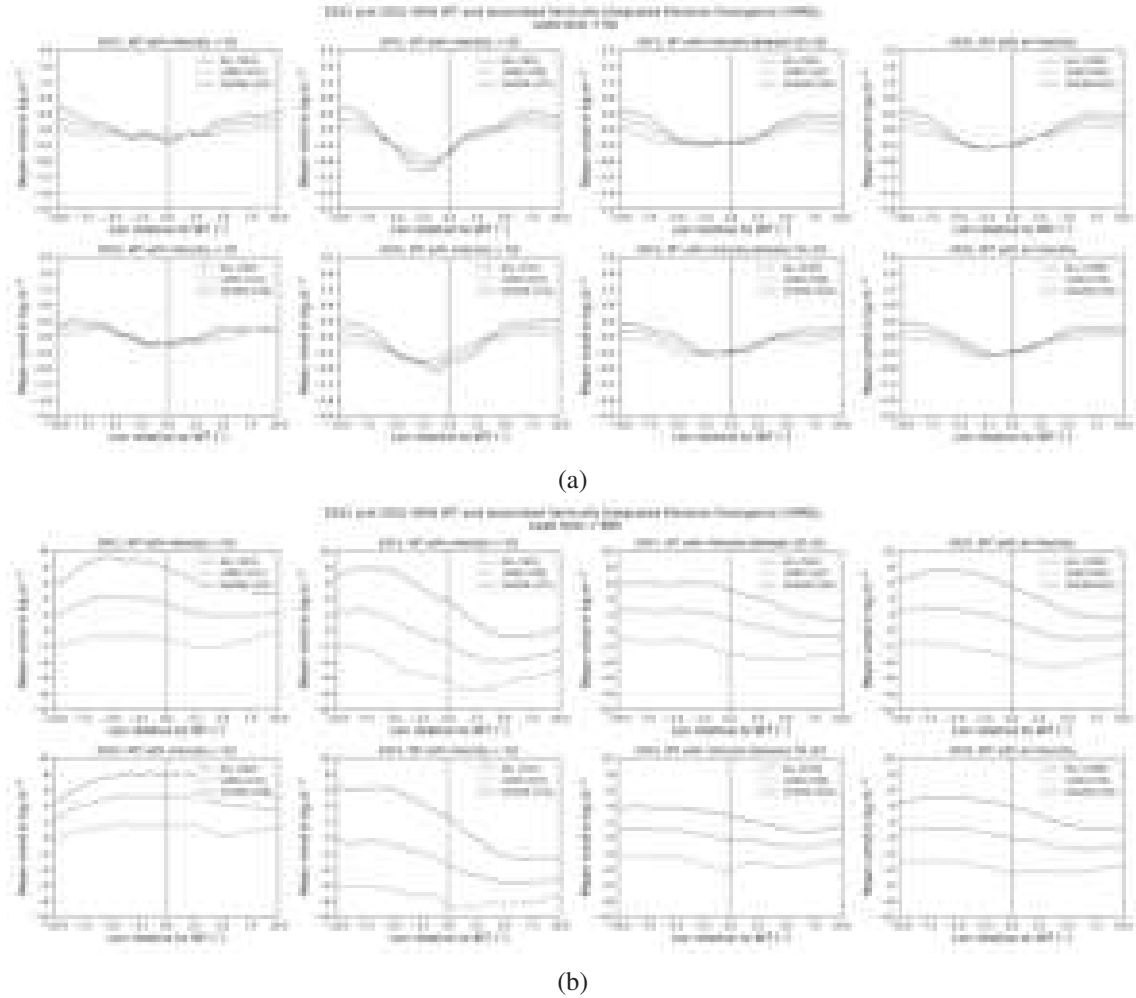## 5.4.2 Vertically Integrated Moisture Divergence

(a)

(b)

Figure 5.9: Similar to Fig. 5.3, results of the average Vertically Integrated Moisture Divergence (VIMD) aligning to all corresponding WT axes by composite with lead time (a) 0 hours (b) 96 hours

Another variable to evaluate is the Vertically Integrated Moisture Divergence (VIMD). This product is originally obtained from the moisture content and divergence of a specific grid box. It is mostly observed with a dip ahead of WT in the VIMD, which implies convergence behaviour. From Fig. 5.9, as represented by the initial condition, more intense WT is related to a larger fluctuation and a significant dip in magnitude. While based on the lowest point ahead of WT in this composite analysis, this indicates the relative location for convergence to take place. The peak of convergence dip is observed more into the wave trough and slightly behind, weaker WT has a flatter distribution, stay close to zero at the WT axis for weaker WT, convergence seen ahead of WT. The fluctuation over the ocean is greater than over the land because of higher moisture content, and the convergence peak of the land WT is larger than that of the ocean WT. 2021 convergence less ahead of the WT over land compared with over ocean. 2022 convergence ahead of WT over land than ocean for stronger WT. It is observed with a gradual retreat of the convergence peak from ahead of WT

shown in the initial condition, to behind the WT in longer lead time hours. For 4 day lead time, the convergence dip points for both land and ocean are situated already behind the WT which does not seem logically sound with the AEW characteristics. There is a big difference between the range of values of VIMD over land and ocean WT. For longer lead time, the VIMD over land WT is always negative, indicating different levels of convergence are always taking place.
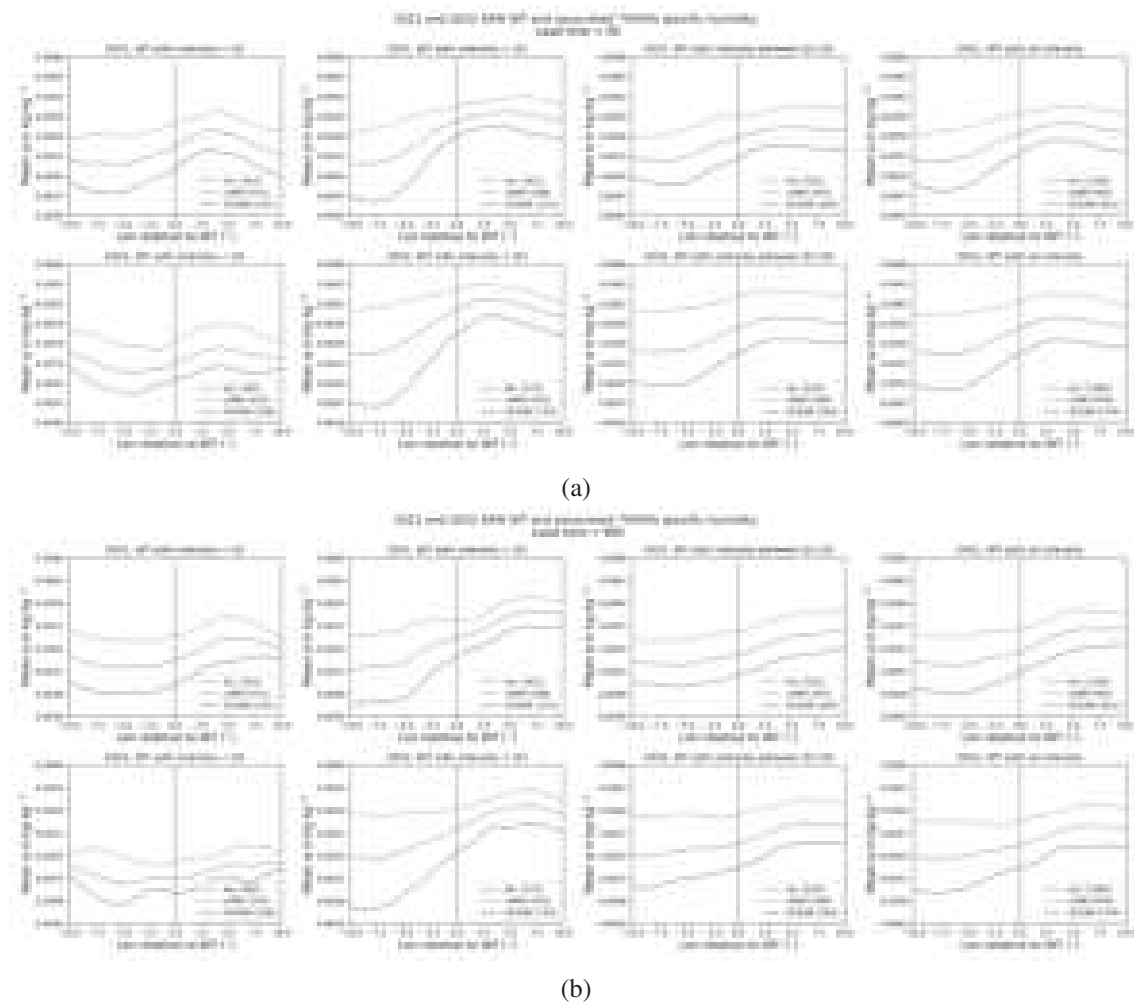
5.4.3 Mid-tropospheric Specific Humidity

(a)

(b)

Figure 5.10: Similar to Fig. 5.3, results of the average 700hPa Specific Humidity (Q700) aligning to all corresponding WT axes by composite with lead time (a) 0 hours (b) 96 hours

The patterns observed for 700hPa Specific Humidity (Q700) are similar to the precipitation field and the other moist variables. Roughly a higher average specific humidity is observed in 2022. For all cases, the specific humidity has its peak behind the WT axes. The difference of q700 over land, especially between weak WT and strong WT in 2022 is much bigger, while the difference is also observable for WT over ocean. In any situation, 700hPa specific humidity associating to WT over land is greater than to ocean. Similar to that of TCWV, there is another converging point observed behind the WT where the gap between blue and orange lines is narrowed. Over land, there is no dip in magnitude observed ahead of WT. This pattern is indeed still observable for a longer lead time, up to 96h.

In the following, similar framework has been applied toward other variables forecast data related to dynamics aligning to the WT and the result will be described.

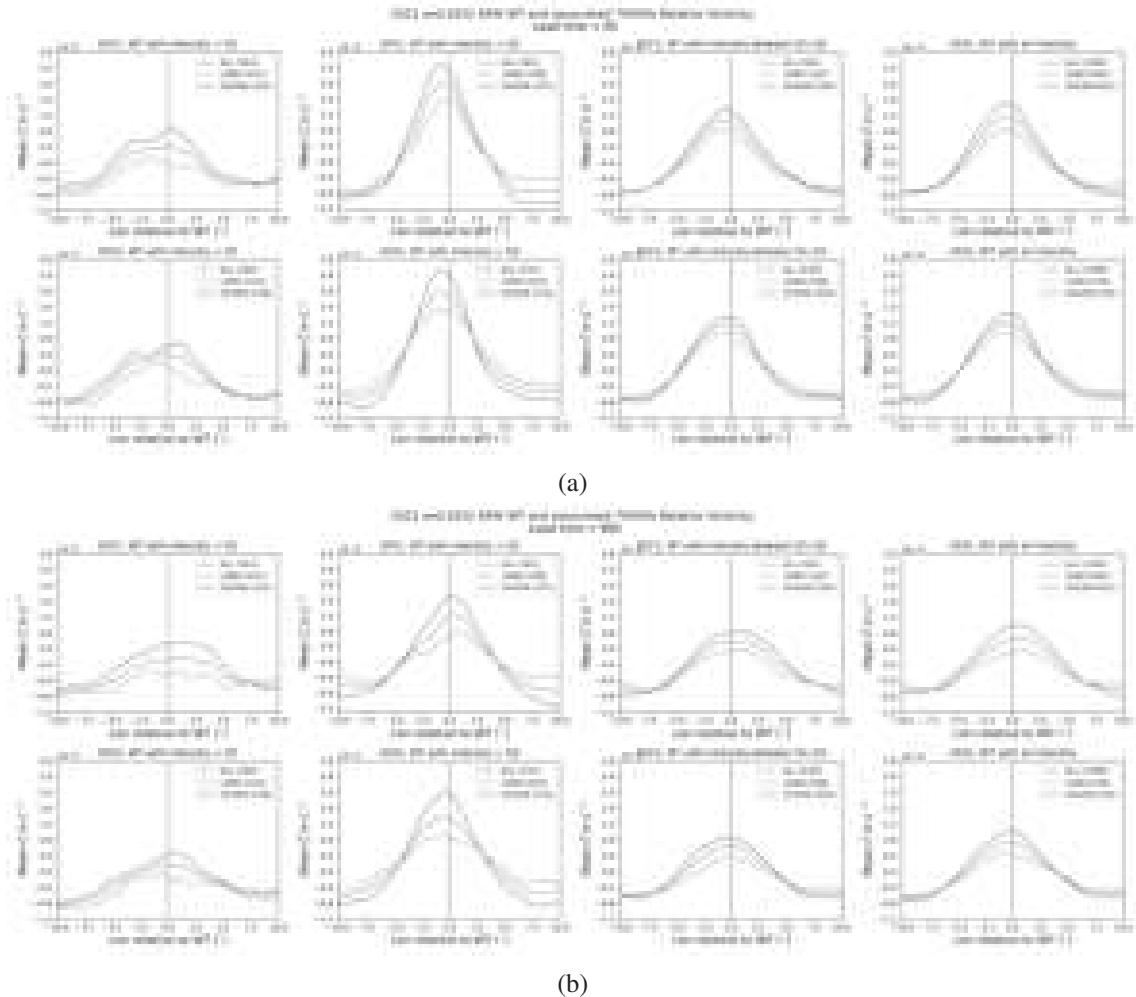## 5.4.4 Relative Vorticity

(a)

(b)

Figure 5.11: Similar to Fig. 5.3, results of the average 700hPa Relative Vorticity aligning to all corresponding WT axes by composite with lead time (a) 0 hours (b) 96 hours

While looking at 700hPa relative vorticity forecast and the ERA5-derived WT axes based on 700hPa wind fields, expectedly the relative vorticity correlates to higher WT intensity positively. The peak magnitude, both for the ocean and the land, coincides mostly with the WT axes, whereas most WT, especially WT, has its peak slightly ahead of WT. A weaker peak is observed for weak WT category. When comparing the peak magnitude, the value of that for ocean WT is greater than that of land WT. For the lead time at 72h and 96h, in 2022 the peak value over land is still observed slightly ahead of the WT. The pattern that ocean WT is associated with a higher relative vorticity than land WT, stays consistent for longer lead time hour window.
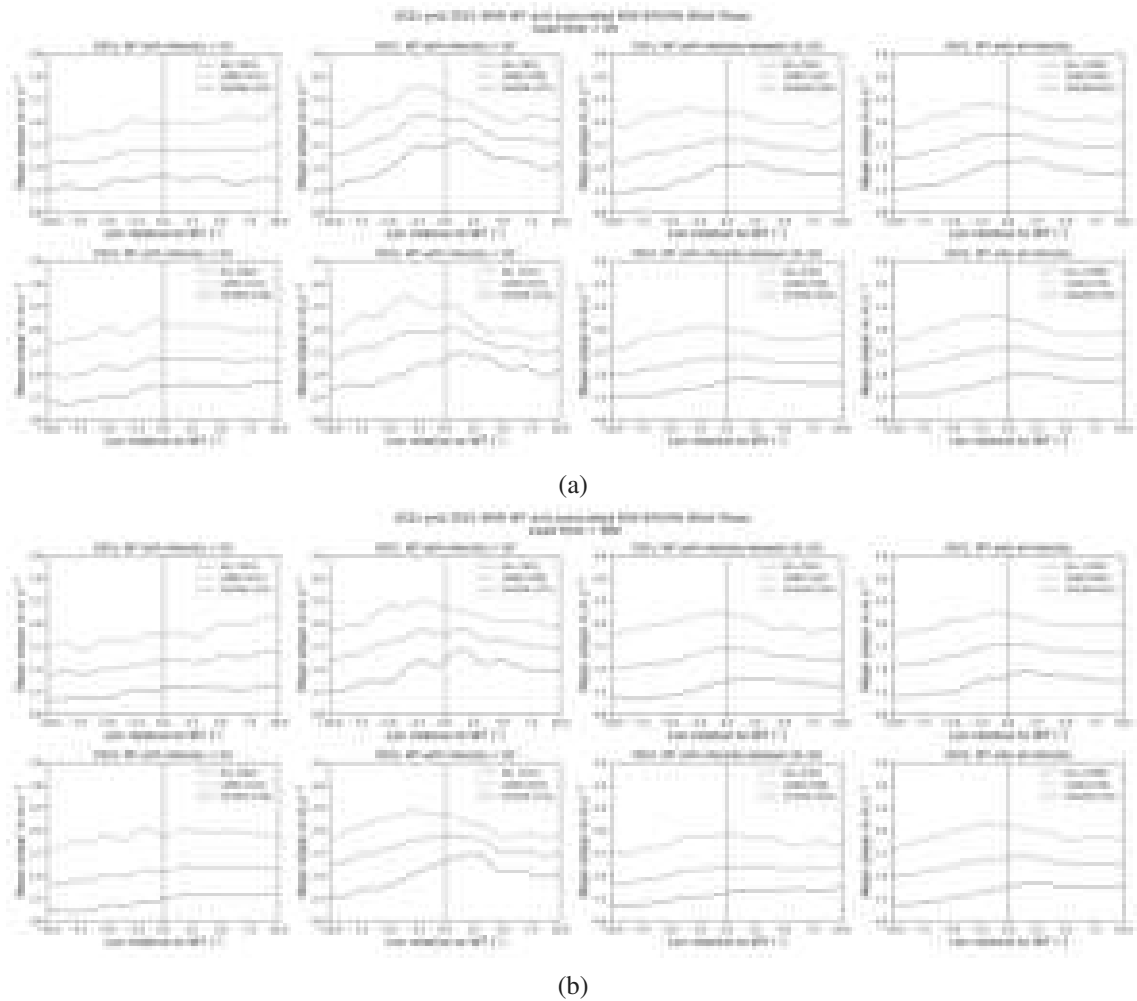
(a)

(b)

Figure 5.12: Similar to Fig. 5.3, results of the average 600-925hPa Wind Shear aligning to all corresponding WT axes by composite with lead time (a) 0 hours (b) 96 hours

5.4.5 Vertical Wind Shear

Since vertical wind shear is an essential element for the organization of MCS/SL, it is expected that AEW propagation would also be dependent on the vertical wind shear and precipitation rate. As shown in Fig. 5.12, higher intensity WT has its peak ahead of wave trough while this is not observable for weaker WT. There is a slight wiggling distribution here than previously shown variables given the same sample size of WT for the composite distributive curves. The wind shear over land is greater than that of the ocean. The peak value for land is ahead of WT while that over ocean is most at the WT axis. The peak of WT over land is more ahead in 2022. A small noticeable signal of peak value ahead of weaker WT (<Q1) over land is also observed in 2022. In general, peak magnitude spreads more ahead of the WT over land in 2022. This conclusion out of this variable is roughly similar to the precipitation rate, but this is showing a relatively smoother composite curve than that of precipitation rate. The alignment has been compiled up to a lead time of 5 days with the same configurations for all mentioned variables.

5.5 Associating other variables with vortex centers

A similar composite method in investigating the association between vortex centers and other variables was performed and the result finding will be presented in the following. Since moist variables, i.e. Total Column Water Vapour (TCWV) and 700hPa Specific Humidity (Q700) are highly impacted by the geographical setting over tropical West Africa, namely south is always moister than the north due to the distance away from the ocean. To minimize such an impact, as explained in Section 4.1.4, the anomaly value from the climatology is computed so as to observe better the association of the various meteorological parameters with the vortex centers.

5.5.1 Total Column Water Vapour

From Fig. 5.13, this displays the composite patterns of aligning TCWV fields to the vortices. 2022 indicates a higher magnitude of TCWV than 2021, as illustrated by the blue contours. In general, the west has a smaller magnitude of TCWV anomaly than the east. At its initial state (lead time = 0h), specifically in 2022, the highest TCWV is found at the northeast quadrant. TCWV associated to land vortices has relatively weaker dipoles than that of ocean vortices. The positive and negative dipoles stay close to the zero relative latitude line in the first year, while the latter year shows an overall moist peak at the whole northeast quadrant. For a longer lead time, 2022 gets generally moister than 2021.

5.5.2 Vertically Integrated Moisture Divergence

As for VIMD, from Fig. 5.14a at its initial condition, convergence peaks, as represented by the green patches, are observed in all plots around the vortex centers in the composite analysis. In 2021, there is a similar well-centerd pattern as the precipitation field in Fig. 5.5a, especially over all and ocean. Meanwhile the latter year demonstrates a rather similar behaviour of precipitation association with all vortices, no matter land or ocean. There is a split in the patches of the peak divergence. The eccentric contours are showing a relatively more widespread in 2022. This variable does not yield anymore sensible values and magnitudes to illustrate vortex-VIMD association for longer lead times. From Fig. 5.14b, there are already parallel contours observed with positive (negative) VIMD values , indicating divergence (convergence) at the relative north (south).

5.5.3 Mid-tropospheric Specific Humidity

Variables representing the moisture fields tend to yield a similar result, namely for the anomaly values of Total Column Water Vapour (TCWV) and 700hPa Specific Humidity. From Fig. **??**, the latter year has an overall higher magnitude than the earlier year. They reveal a pattern that the western quadrants are drier than the eastern quadrants, which is quiet agreeable with the known knowledge in relation to the AEW dynamics. These two variables demonstrate peak values from
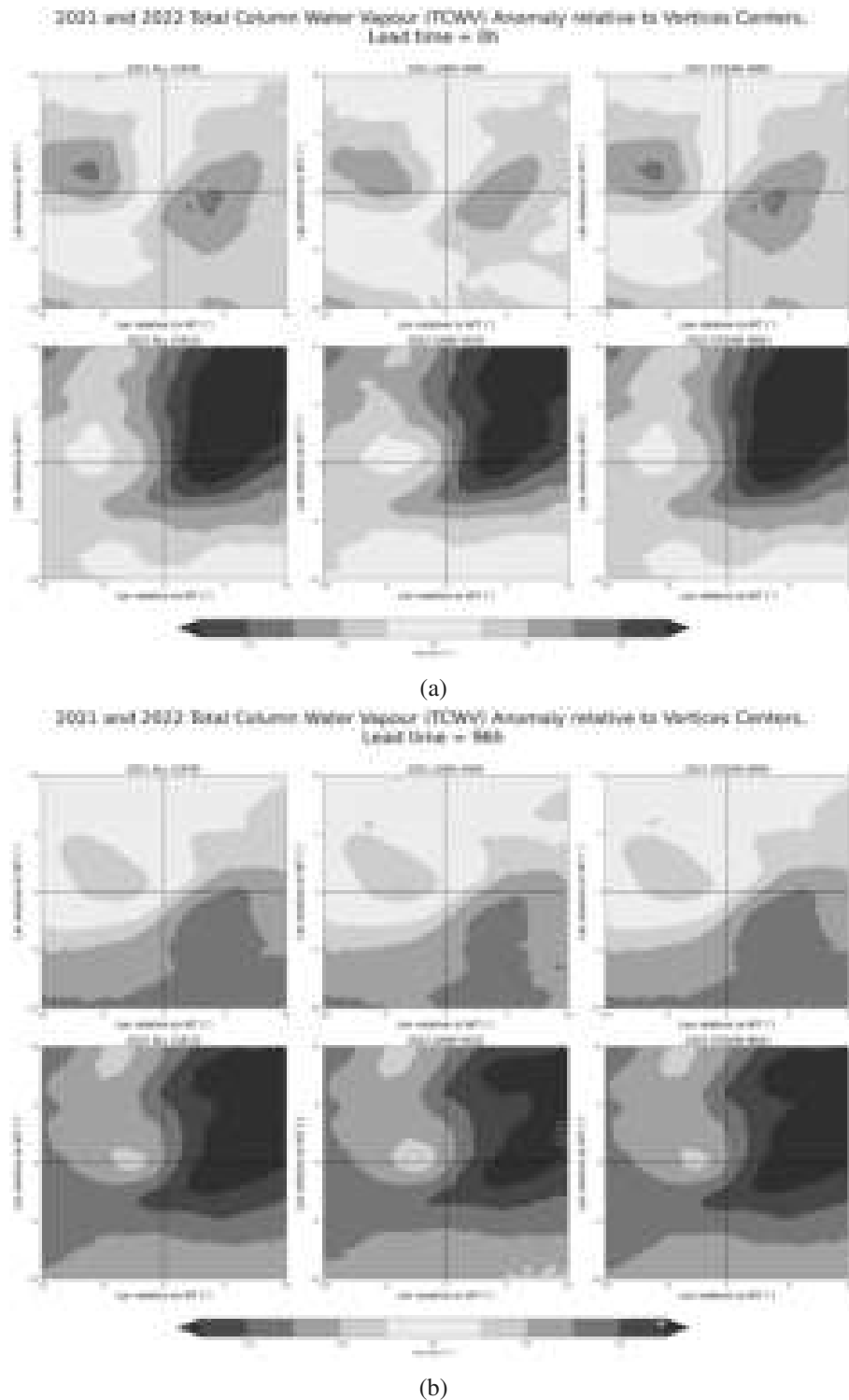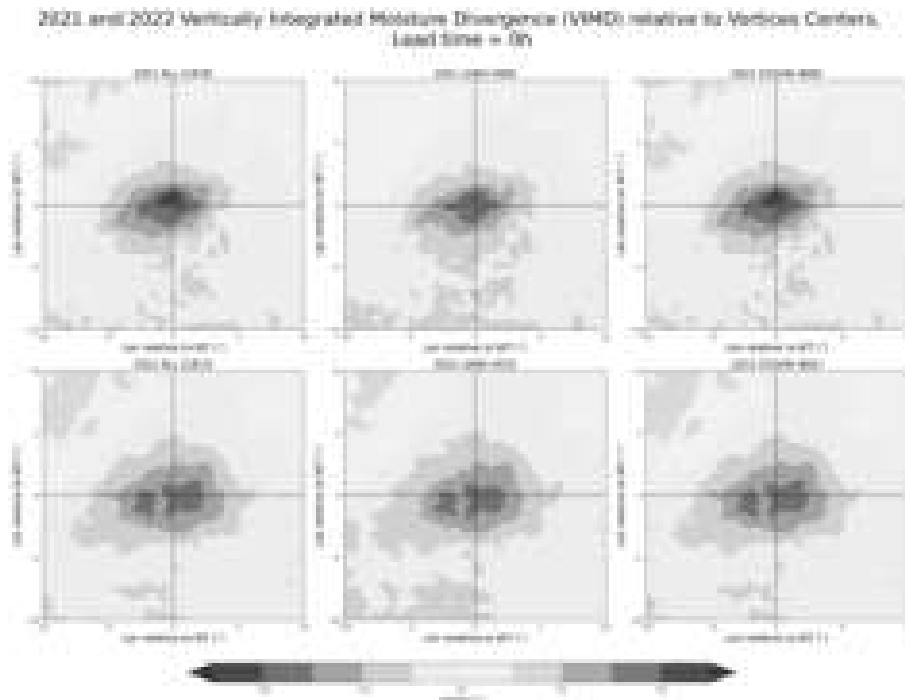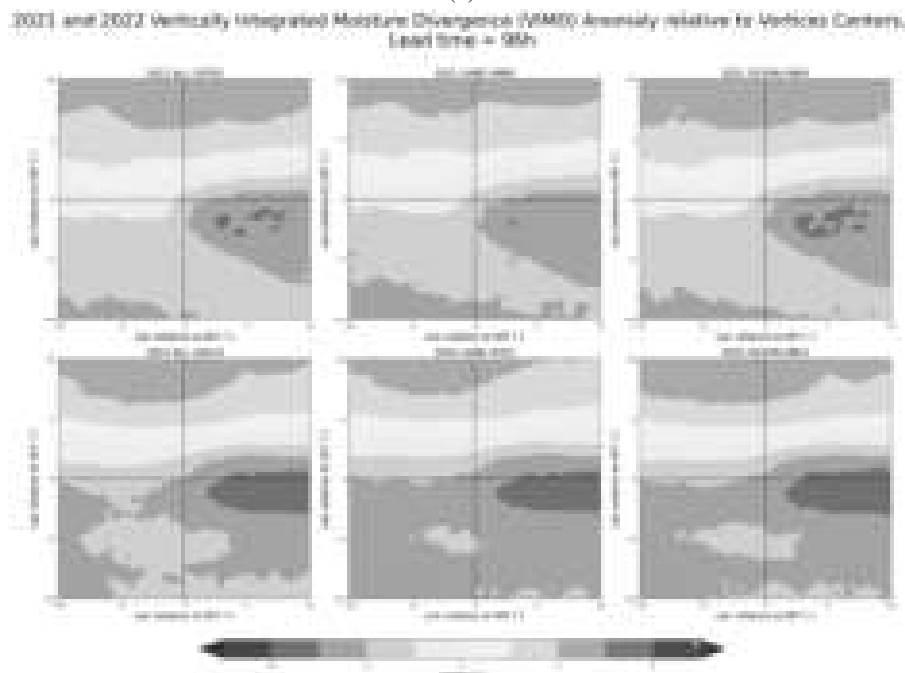
(a)

(b)

Figure 5.13: (a) Composite analysis of the average Total Column Water Vapour (TCWV) anomaly associated with the vortex centers in 2021 (first row) and 2022 (second row) of ECMWF forecast with a lead time of 0 hours. Same configuration as Fig. 5.5 (b) similar to (a), but with lead time 96 hours

the composite at the northeastern side, while the relative negative dipole is located at the west. Comparing the lead time between 0 hour and 96 hours, the initial condition is showing stronger dipoles between east and west while for longer lead times the dipoles become relatively weaker, but still obvious.

(a)

(b)

Figure 5.14: (a) Composite analysis of the average Vertically Integrated Moisture Divergence (VIMD) anomaly associated with the vortex centers in 2021 (first row) and 2022 (second row) of ECMWF forecast with a lead time of 0 hours. Same configuration as Fig. 5.5 (b) similar to (a), but with lead time 96 hours

From Fig. 5.16 and 5.17, they illustrate the difference in the moisture field anomalies between 2021 and 2022. It is observed that for both variables, the increase in their values over the northern side is more significant in 2022 than 2021. For TCWV, the northern part becomes moister while the southern part becomes drier. As for Q700, the whole composite is patched with blue color while
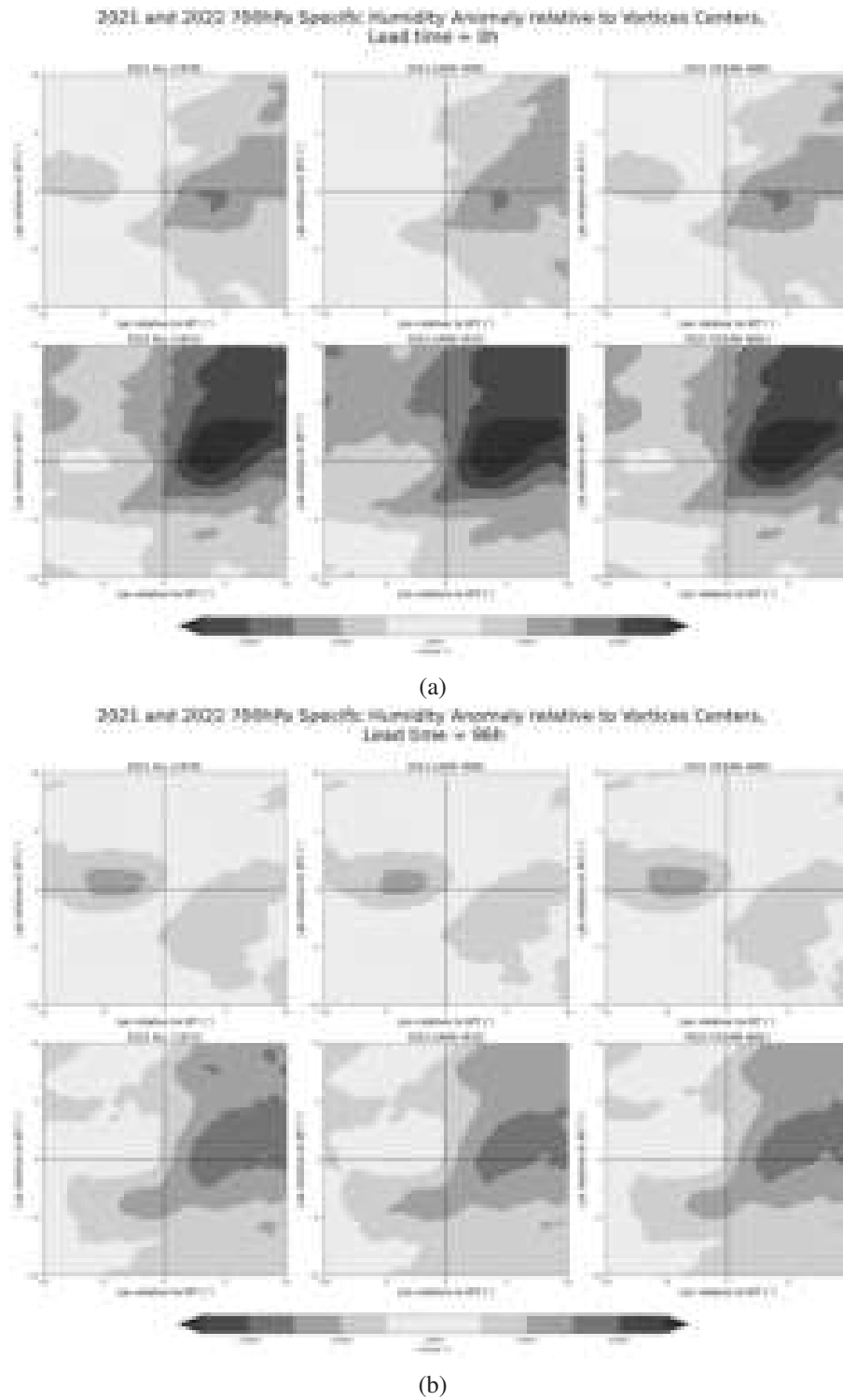
(a)

(b)

Figure 5.15: (a) Composite analysis of the average 700hPa Specific Humidity anomaly associated with the vortex centers in 2021 (first row) and 2022 (second row) of ECMWF forecast with a lead time of 0 hours. Same configuration as Fig. 5.5 (b) similar to (a), but with lead time 96 hours

implies an overall higher q700 values in the vortex composite. This implies a possible moisture organization within the model computation.
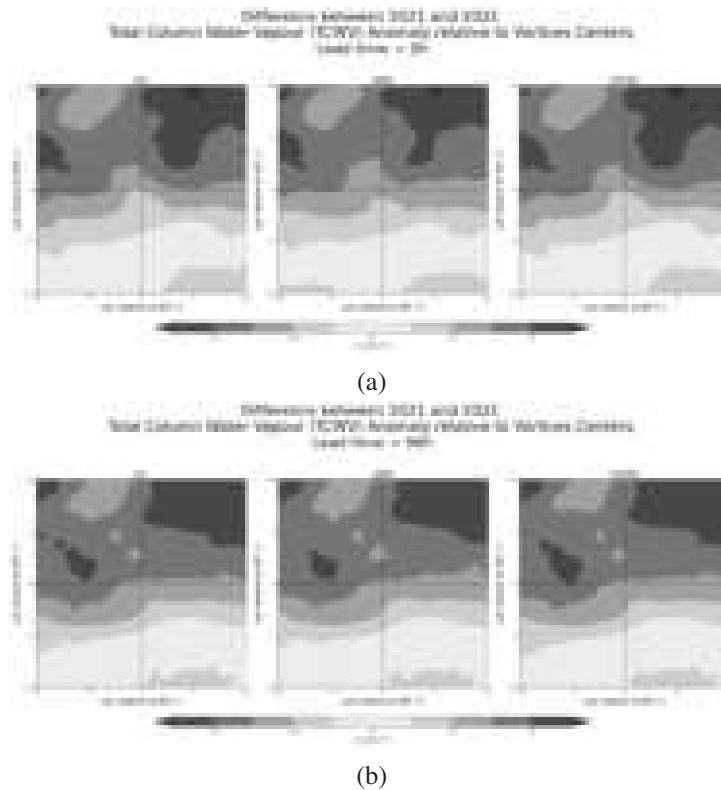
(a)

(b)

Figure 5.16: The difference in TCWV anomaly between 2021 and 2022 based on the same configuration of Fig. 5.5. This is calculated by the subtraction 2022 from 2021. Red (blue) colour indicates 2022 has lower (higher) TCWV values than 2021. (a) For the initial condition, lead time 0 hour (b) Lead time 96 hours

Apart from the moisture-related variables, the vortex association technique has been applied to other variables related to the dynamics.

5.5.4 Relative Vorticity

As shown in Fig. 5.18, this compares the initial condition and 96 hour lead time association of 850hPa relative vorticity to the ERA5-derived 850hPa vortex centers, expectedly all of the plots demonstrate that the peak values are well centered, for all, regardless for vortices over land or ocean. For the initial condition, 2022 has a higher peak vorticity value than 2021. This is the most observable for the composite of all vortices and ocean vortices, while for lead time 96 hour, the contrast of the peak vorticity value at the center is not significant.

5.5.5 Vertical Wind Shear

From Fig. 5.19, the contours are slanting from northwest to southeast with a peak wind shear found at the northeast quadrant. Highest wind shear observed at the northeast quadrant, especially over land vortices. This pattern is also observable in longer lead time. In association with vortices, the northern side has a higher wind shear than the southern side relative to the composite vortex centers.
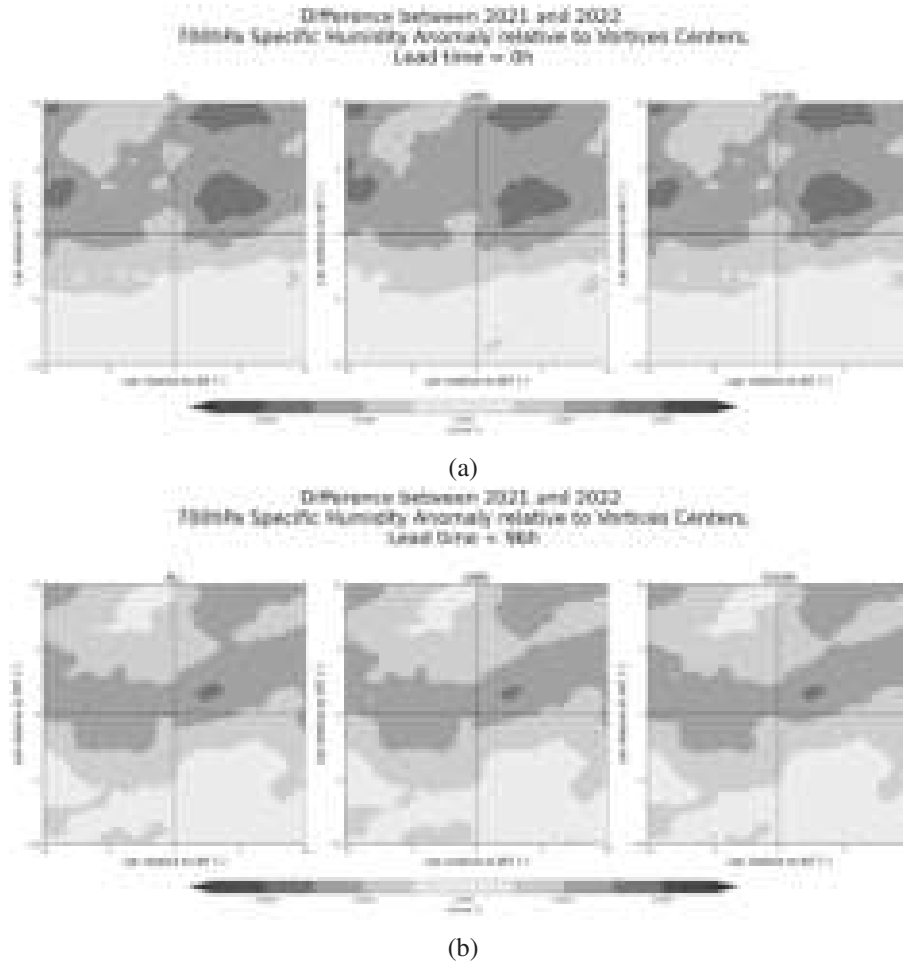
(a)

(b)

Figure 5.17: The difference in Q700 anomaly between 2021 and 2022 based on the same configuration of Fig. 5.5. This is calculated by the subtraction 2022 from 2021. Red (blue) colour indicates 2022 has lower (higher) Q700 values than 2021. (a) For the initial condition, lead time 0 hour (b) Lead time 96 hours

The above has provided the description of various plots which aim at understanding the coupling of important elements within AEW, especially between precipitation field and WT or vortex centers.
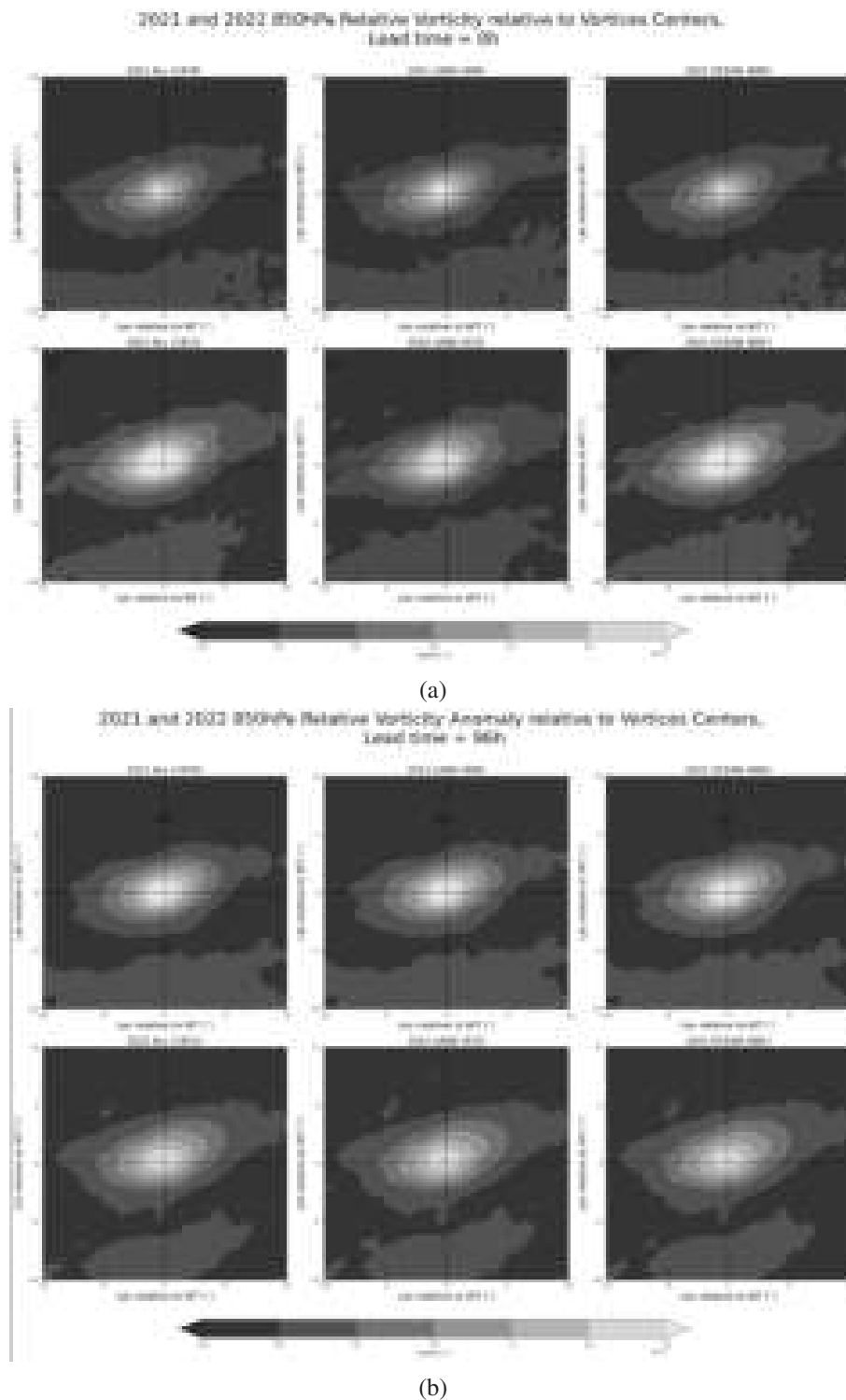
(a)

(b)

Figure 5.18: (a) Composite analysis of the average 850hPa Relative Vorticity associated with the vortex centers in 2021 (first row) and 2022 (second row) of ECMWF forecast with a lead time of 0 hours. Same configuration as Fig. 5.5 (b) similar to (a), but with lead time 96 hours
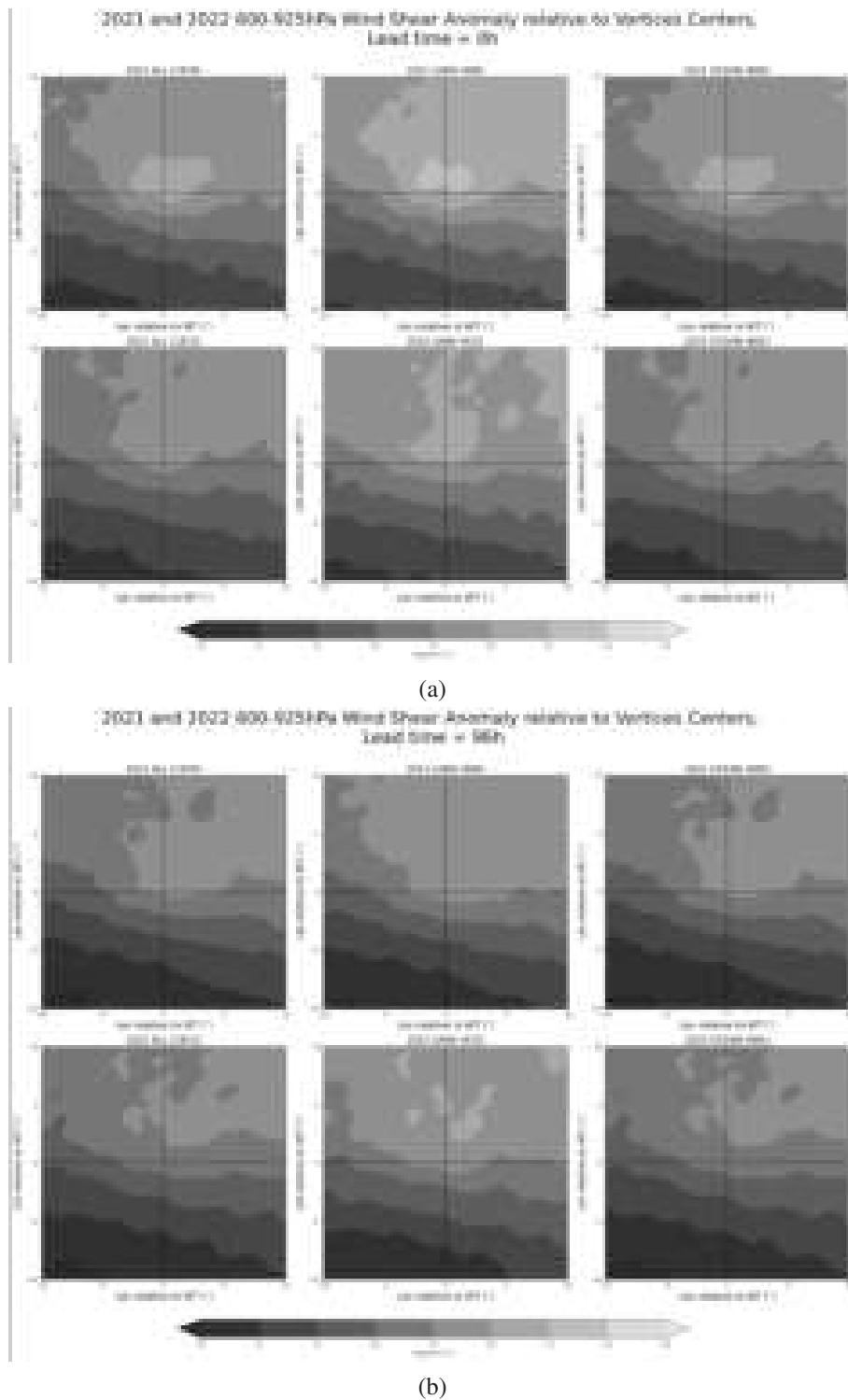
(a)

(b)

Figure 5.19: (a) Composite analysis of the average 600-925hPa Wind Shear associated with the vortex centers in 2021 (first row) and 2022 (second row) of ECMWF forecast with a lead time of 0 hours. Same configuration as Fig. 5.5 (b) similar to (a), but with lead time 96 hours

6 Conclusion and Outlook

The forecast skill on precipitation over tropical West Africa has been notoriously low due to the intricacies of various factors in simulating the weather patterns (Vogel et al., 2018). There is often a low rainfall persistence observed over the region (Nicholson, 2018). Among all possible factors, the synoptic-scale forcing is expected to contribute to a large variance in the predictability of tropical West Africa, namely AEW. Given the adiabatic and diabatic natures of AEW, the importance of understanding the phase relationships between AEW and precipitation could not be overlooked. An upgrade in the moist physics of ECMWF IFS is expected to bring a change into the subgrid-scale parameterization and better resolve the moisture convergence and organization (Bechtold et al., 2020; Becker et al., 2021).

Therefore, this project has been created to study the possible associations between precipitation fields and other variables related to the environmental conditions relative to AEW troughs, from the two model versions, namely ECMWF IFS Cycle 47r2 and 47r3, focusing on AEW in the summer months of 2021 and 2022 correspondingly. As indicated in Table 5.1, the wave trough dataset provides a reasonable result in terms of the number of tracks, lifetime, length and propagation speed, agreeing with the known AEW characteristics (Carlson, 1969a,b; Burpee, 1972).

A composite analysis framework has been developed to align precipitation field with wave trough axes. Referring to the composite result, the patterns observed is corresponding to the previous research findings about AEW dynamics and the importance of precipitation influencing AEW growths in its lifetime (Berry and Thorncroft, 2005; Janiga and Thorncroft, 2016). Precipitation is linked as the source of diabatic heating and the location of precipitation embedded in the AEW structure would affect growth of the disturbance. At the earlier stages, there are some localized convective triggers due to orography over East Africa leading to topographic lifting. They are possibly in relation to MCS which could bring abrupt increase in moisture content, where potential vorticity anomaly is initially situated. The initial cyclonic shear is found along African Easterly Jet which is favouring baroclinic growth. The isentropic lifting due to convective systems ahead of WT leads to PV redistribution. This leads to advection of PV anomaly such that the wave disturbance propagates westward.

Over land WT, the peak of precipitation is found ahead of WT. When comparing the composites of 2021 and 2022, the latter year shows precipitation peak further ahead of the WT than 2021. This could be an improvement in representing AEW propagation which highlights the importance of AEW-precipitation phase relationship representation. On the contrary, when precipitation is located more at the WT axis, this increases PV anomaly and the WT is therefore intensified. This is likely to take place near the Guinea coast at the west or even over the Atlantic ocean as the

disturbances hit the Guinea Highland (Berry and Thorncroft, 2005). There is local orography-driven convection which could intensify the WT. The above phase relationship could also be observed from the composite of both the forecast and observation field.

After observing the behaviours of different WT categories, the location and intensity of the WT have an remarkable effect on the modulations to the precipitation patterns. Precipitation associated with land WT is expected to be higher than that over ocean WT. This pattern can be distinguished especially for the group of WT with intensity >Q3. The rainfall distributive curve shows a sharper peak than the composite curve of weaker WT category. The thermal difference between land and ocean is the main driver of convection in the tropical domain. Moist and cool monsoon air blows inland, while over the desert area at the north, the air mass is hot and dry. Ahead of the WT, it represents the mid-level northerly regime where the shear between the south moist and cool air and the Saharan Air Layer (SAL) is strong and there is a region with the strong convergence ahead of the WT. Recalling the necessity of ascent forcing for strong convective development, the convergence between SAL over the continent and moist monsoonal air is effective in building up CAPE. This also corresponds to a higher wind shear over the convergence region. A strong low-level wind shear is important for sustaining the lifetime of MCS or SL (Maranan et al., 2018). In this composite framework associating with WT axis, the distribution of precipitation within the relative longitude is similar to that for vertical wind shear (Fig. 5.19). From the above result, stronger WT modulates the rainfall and vertical wind shear to a greater extent which underscores the importance of AEW-precipitation coupling so as to best understand the factors modulating tropical rainfall. This implies that an improved representation of AEW will likely improve the rainfall forecast. The overall coupling pattern between precipitation and WT gets faded out after 3-4 days. This could tell the temporal extent of AEW-precipitation coupling is no longer observed with this lead time barrier.

One of the major advances from IFS Cycle 47r2 to 47r3 is the addition of the total advective moisture tendency term into the convective instability closure computation. The enhancement of the moist physics scheme is striving for a better representation of deep convection coupled to the dynamics. Contrasting the above result of 2021 and 2022, AEW-precipitation phase relationship over land or ocean from this analysis is legitimate in illustrating the improved propagation of rainfall systems, given the parameterization scheme used to be incapable in simulating MCS with a probable propagating direction (Crook et al., 2019). While the rainfall systems, especially MCS, are propagating westward along with AEJ or AEW.

To further elaborate on a possible theoretical interpretation, precipitation is enhanced ahead of wave disturbances trough due to the presence of favorable atmospheric conditions. As the AEW propagates, it generates a region of convergence and upward motion in the atmosphere, creating an area of low pressure. Therefore, it is common to observe a convergence dip ahead of WT (Fig. 5.9). This low-pressure system leads to the ascent of moist air, resulting in the formation of clouds and precipitation. The peak of wind shear in association with vortex centers over land WT is located its northeast quadrant, and such pattern is more pronounced over land (Fig. 5.19). In relation to AEW dynamics, ahead of the wave trough, where vortices are commonly found embedded. Ahead of the AEW wave trough, the flow pattern is characterized by mid-level northeasterly winds, which

promote the convergence of moist air masses from different directions. The convergence of moist air enhances the uplift and condensation processes, leading to the development of deep convective clouds and increased precipitation.

On the other hand, behind the wave trough, the flow pattern transitions to mid-level southwesterly winds. These winds are associated with a subsidence region where the air is descending. Descending air suppresses the uplift and condensation processes, inhibiting the formation of clouds and precipitation. Based on the plots from WT-coupling analysis, there is higher moisture content behind the WT thanks to southerly regime in the AEW structure, yielding a higher moisture content, namely higher TCWV (Fig. 5.8). However lifting motion is not particularly significant in contrast to ahead of WT. Consequently, precipitation is generally reduced or suppressed behind the AEW wave trough (Fig. 5.3. Overall, the contrast in precipitation patterns between the regions ahead and behind the AEW wave trough is primarily attributed to the differential atmospheric conditions, including wind patterns and associated vertical motion.

Over oceanic regions, especially the Gulf of Guinea and the Atlantic Ocean, TCWV tends to be higher compared to land areas. This is primarily due to the large moisture source provided by the warm sea surface temperatures, which facilitate strong evaporation and moisture transport into the atmosphere. As a result, the total column water vapor, which integrates moisture content throughout the entire atmospheric column, is higher over oceanic regions as shown in Fig. 5.8. Despite the higher TCWV over oceanic regions, the mid-level specific humidity, namely at 700hPa is often higher over land compared to ocean along the AEW structure (Fig. 5.10. This discrepancy is attributed to the baroclinic nature of AEWs and the dynamics associated with them. AEWs are characterized by alternating cyclonic and anticyclonic circulation patterns, as seen from the troughs and ridges along the jet level. Within the AEW structure, there are regions of ascent and descent, which are associated with convergence and divergence of air masses, respectively. Strong convergence zones associated with AEWs lead to upward motion and the lifting of moist air to mid-levels of the atmosphere. This results in higher specific humidity at 700 hPa over land in particular. Over oceanic regions, while the total column water vapor is high due to the direct moisture source from the sea surface, the mid-level specific humidity may be relatively lower because the lifting mechanisms associated with AEWs are less prominent over water compared to land. As a matter of fact, there is a slight converging point behind the WT in the southerly regime where the difference of q700 distribution between land and ocean becomes smaller. This observed pattern could be attributed to an overall positive mid-level moisture anomalies associated with ocean WT into or behind the WT.

As for the composite of the relative vorticity fields aligning with WT at 700hPa staying close to the jet level, it is expected that the relative vorticity peak should stay close to the composite WT axis. In general, WT over ocean is observed with higher relative vorticity along the WT axis than WT over land which could be attributed to a probable trend of West Coast development proposed by Berry and Thorncroft (2005).

From the above, the result has displayed good linkages to previous studies concerning the AEW-related moisture and kinematic fields. There is a need in simulating the baroclinic processes within

AEW so as to explain the underlying factors influencing tropical rainfall variability. Thanks to moist physics upgrade possibly, a change in moisture convergence and organization of AEW observed between the two years.

Vortices are commonly found embedded in the AEW structure which propagates westward along the disturbances. It has been assumed that the filtered vortices could best represent those within AEW. Therefore another 2D vortex-precipitation association composite has been developed. From this composite analysis, a shift in the peak location of precipitation associating with the vortex centers is observed, from well-centered in 2021 to slightly westward or ahead of the vortices' propagation direction in 2022. The complete agreement between ECMWF forecast field and IMERG rainfall fields cannot be expected from their magnitudes, but the relative position of the precipitation peak is worth to inspect. When comparing the two years, the latter year produced a more ahead precipitation peak ahead of the vortex centers. While for IMERG, indeed it is also found with a few degrees ahead for the latter year. The extent for IMERG is smaller but yet to be quantified. However this shows that the change in the composite of precipitation field associating with vortex centers from the ECMWF forecast could be a mixture of the change of actual dynamics change and moist physics in IFS.

Along the relative longitude and latitude axes in the composite, this vortex-composite framework is able to showcase the relative position of precipitation in 2-dimensional how far the convective systems are away from vortex centers by composite. The width and length of the box drawn by relative longitude and relative latitude are the same as the geographical directions relative to vortex centers. The left (right) side of both AEW or vortex-precipitation association axes could be roughly deemed as northerly or southerly regime of the AEW. This has been assumed that the vortices are well located at the two flanks of AEJ, aligning to the WT axis. In addition, when looking at the TCWV anomaly and Q700 anomaly, it is observed that the latter year exhibits an overall moister environment. It is affirmative to say that there is a change in moisture organization and convergence between the two years, which the revision of the moist physics enhances the capability to reproduce the AEW-precipitation phase relationship.

AEW troughs are identified at the mid-tropospheric level, around 600-700hPa. A positive PV anomaly provides a favourable environment for convective growth. Trough propagation has a higher predictability thanks to the known range of wavelength and lifetime (Burpee, 1972), in comparison to the relatively variable precipitation patterns over tropical West Africa.

Indeed there is a challenge of finding an association through the vortices and wave troughs datasets. The vortex dataset is computed based on velocity gradient tensors of the wind fields while AEW identification and tracking algorithm is following Belanger et al. (2016) which is based on the advection of curvature vorticity anomaly. Due to the different identification and tracking algorithms between the wave troughs and vortices, which might not directly show the direct relationship between the two features within the dynamics, a radius search method was attempted to associate possible vortices centers with the wave trough axis in accordance to the proximity. With reference to Fink and Reiner (2003), as AEW propagates westward, two main tracks of the vortices were observed to be propagating along, namely a northern track at 850hPa and a southern track at 700hPa.

The decision of the radius threshold can be in accordance to the known scale of AEW wavelength. The radius varied from 0 to 2000km and this method aims at giving a binary classification if any vortex center could be associated to this certain wave trough edge (not shown). There could be a few successful cases which could see the vortex centers are associated to certain convective systems along the WT. However the vortex datasets are yielding relatively noisy output. It is uncertain to establish a conclusion while a minor difference of the vortex location relative to WT axis, namely ahead, into or behind WT may also contradict the proposed AEW structure. Therefore the analysis from WT representing the environmental conditions within AEW is yet to be fully explored. In this thesis, the focus has been on the wave trough dataset which is more authentic to represent AEWs, being the targeted synoptic features in this study.

The emphasis of this project is to investigate any observable changes between the ECMWF operational forecast in 2021 and 2022. Regarding the possible future research directions, a bigger sample size composite could also be calculated from the ERA5 datasets, based on the climatological mean from the coupling of overall wave troughs or vortices obtained from the ERA5-derived wind fields, and the related meteorological parameters for all years, as a benchmark with similar methodology in the future. The model physics would be homogeneous for all years in the reanalysis dataset.

Moreover, it would also be worthwhile to look into ensemble forecast datasets so as to understand the overall likelihood of AEW-precipitation phase relationship in the model run. The project can be extended into the investigation over the predictability of AEW and associated rainfall in terms of the phase relationship. This requires wave trough and vortices identification and tracking algorithm over the forecast data , which includes multiple initializations and lead time dimension. In this study, the AEW-precipitation coupling pattern is blurred out with longer lead times since somehow it could be attributed to the drifting of the whole prediction of the dynamics. Their relationship between AEW-precipitation could even be represented for longer forecast length in the model simulation, but yet to be explored. In addition, with the use of other ensemble member forecast, this involves a bigger sampling size and the investigation into the mean pattern and ensemble spread. It could boost the confidence of the pattern observed over the precipitation rate or other variables relative to the wave trough axis. At this point, the statistical significance is yet to be investigated in view of a relatively wiggling curves due to a limited sample size in the composite manipulation.

Potentially, direct subtraction from the distributive curves between 2021 and 2022 would conceal the possible double penalty problem (Davis et al., 2006; Wernli et al., 2008), namely a plausible prediction of the amplitude and size of the precipitation but just slightly wrong positioning of the precipitation, leading to a higher error scores. Instead, other sophisticated spatial verification of precipitation forecast, such as Fraction Skill Score (FSS) or SAL method, meaning Structure (S), Amplitude (A) and Location (L), as one of the novel measures by Wernli et al. (2008) in verifying quantitative precipitation forecasts could be incorporated in this WT-precipitation coupling configuration. This could provide a more holistic approach in evaluating rainfall forecast performances with a rather inclusive criteria through scoring.

Recently, there has been another important upgrade over the horizontal resolution of the ECMWF Integrated Forecasting System Cycle 48r1 in June 2023, namely boosted from 18km to 9km. Even as suggested from (Becker et al., 2021), physical parameterization might still play a bigger role in terms of providing accurate forecast of rainfall than higher horizontal resolution. Thanks to the advancement in computational power, higher horizontal resolution with smaller grids can better simulate more smaller processes but it still does not directly mean an improved capability to explicitly resolve all these underlying processes well. Further investigation in the behaviours of AEW-precipitation phase relationship of 2023 would be worth-exploring.

7 Abbreviations

AEJ   African Easterly Jet

AEW   African Easterly Waves

BL   Boundary Layer

CAPE Convective Available Potential Energy

CIN   Convective Inhibition

CV   Curvature Vorticity

ECMWF European Centre for Medium-Range Weather Forecasts

EPS   Ensemble Prediction System

LCL   Lifting Condensation Level

LFC   Level of Free Convection

IFS   Integrated Forecasting System

IMERG NASA's Integrated Multi-satellitE Retrievals for GPM

ITCZ   Intertropical Convergence Zone

ITD   Intertropical Discontinuity

MCC   Mesoscale Convective Complex

MCS   Mesoscale Convective Systems

NWP   Numerical Weather Prediction

OLR   Outgoing Longwave Radiation

PDF   Probabilistic Density Function

PV   Potential Vorticity

PW   Precipitation Water

Q700   700hPa Specfic Humidity

SAL   Saharan Air Layer

SL   Squall Lines

SHL   Saharan Heat Low

STJ   Subtropical Jet

TCWWV Total Column Water Vapour

TEJ   Tropical Easterly Jet

VIMD Vertically Integrated Moisture Divergence

WAM West African Monsoon

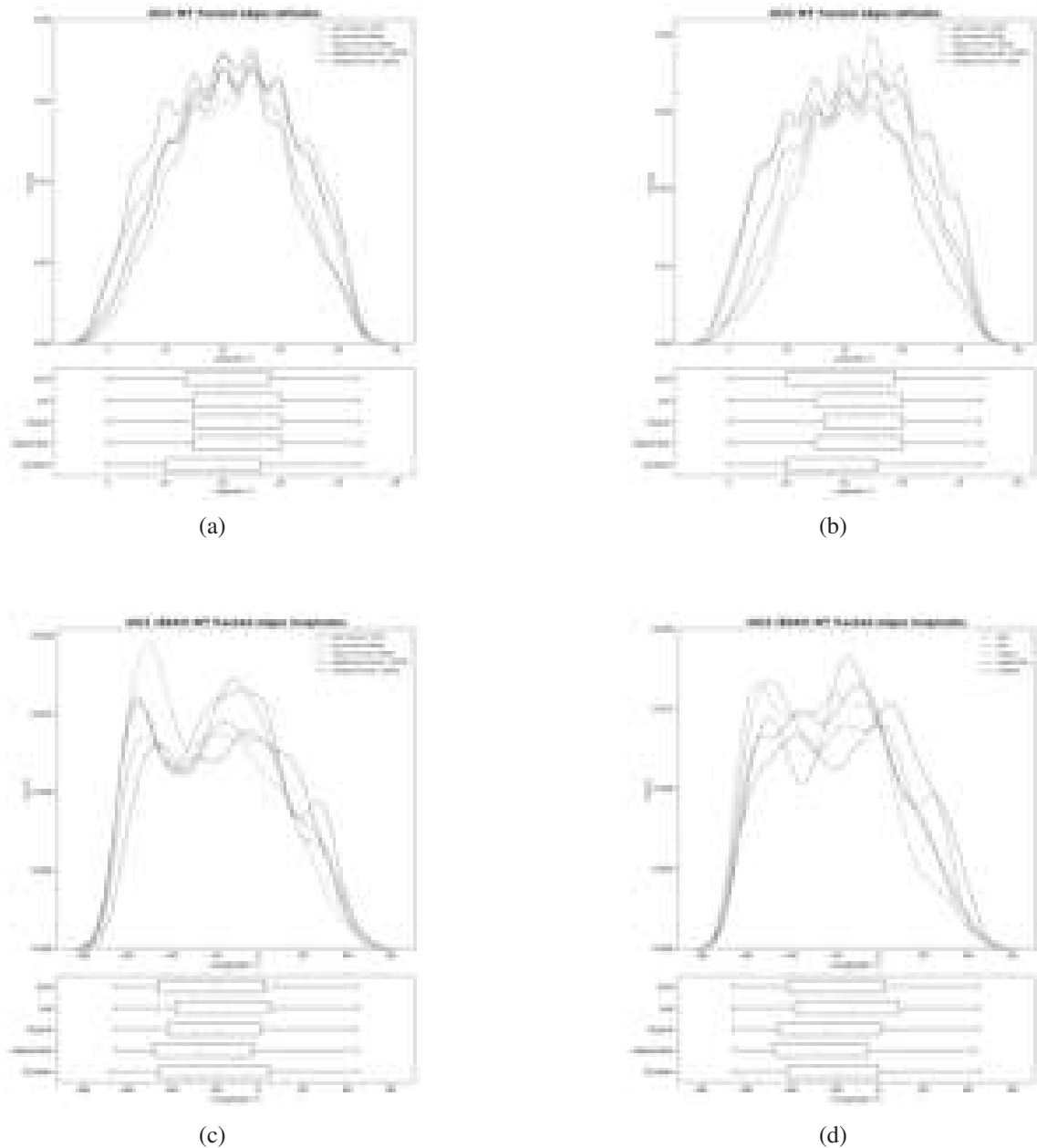**WT**   AEW trough / Wave trough

Appendix

(a)

(b)

(c)

(d)

Figure 7.1: Statistics of the positions of wave trough edges, which indicates the points with zero CVA-advection. (a)-(b) show the latitudinal positions in 2021 and 2022 respectively while (c)-(d) show the corresponding longitudinal positions. In each subplot, the upper panel shows the density plot of edges found in each month, and the bracket has also included the sample size of the counted edges. While the lower panel shows a box plot of the monthly distribution of edges within the corresponding geographical ranges, namely (a)-(b) for latitude and (c)-(d) for longitude for 2021 and 2022.
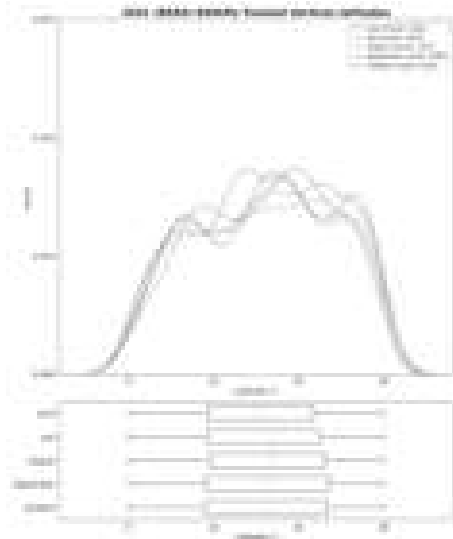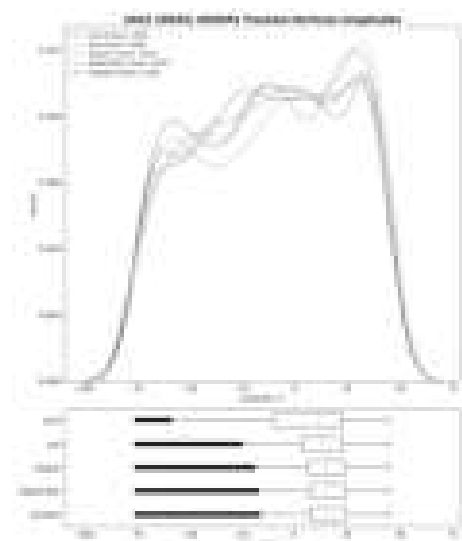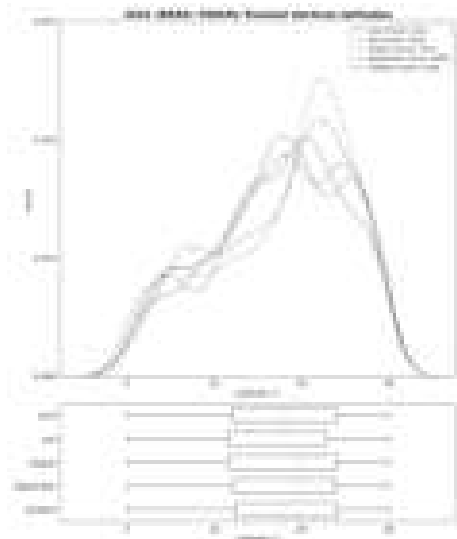
(a)
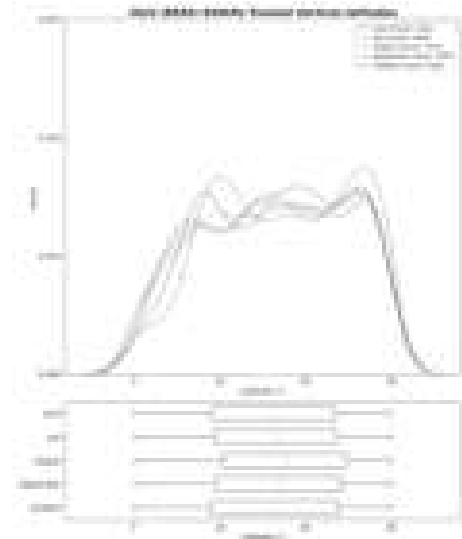
(b) 2022 latitude
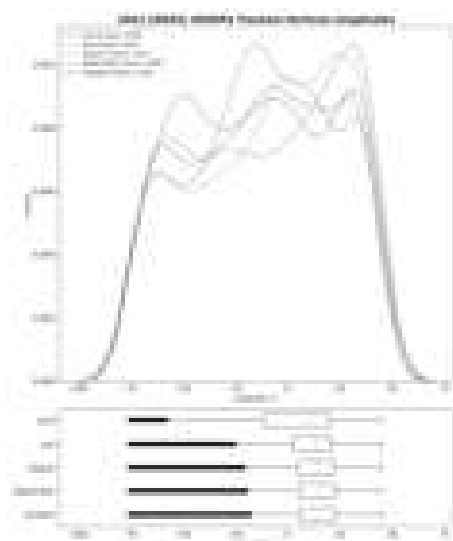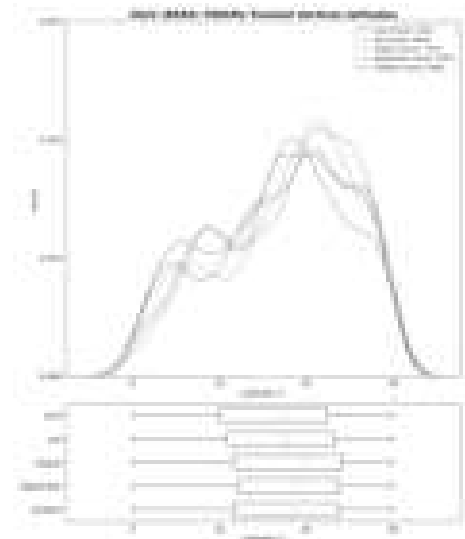

(c) 2021 longitude

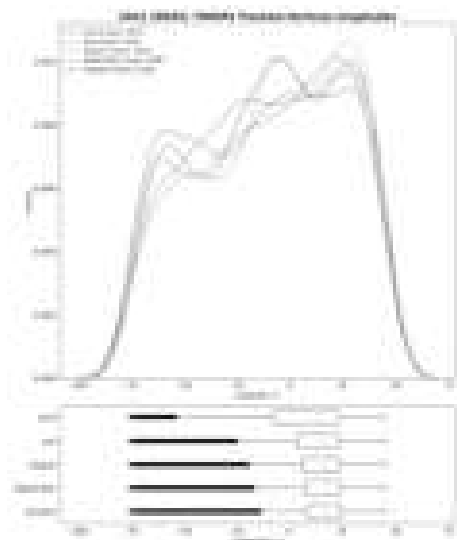(d) 2022 longitude

Figure 7.2: Statistics of the positions of 850hPa vortices centers. The plot setting is similar to Fig. 7.1
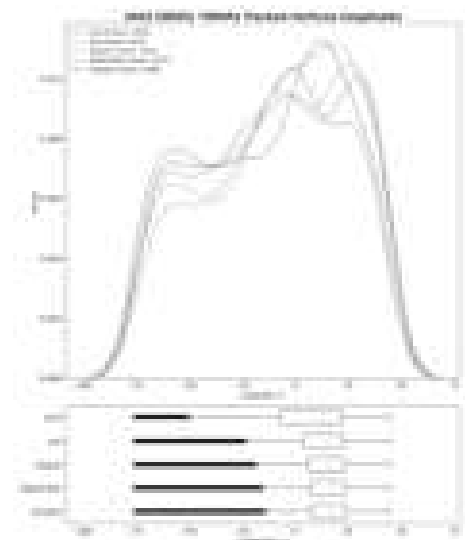
(a)

(b)

(c)

(d)

Figure 7.3: Statistics of the positions of 700hPa vortices centers. The plot setting is similar to Fig. 7.1 (a) 2021 latitude (B) 2022 latitude (c) 2021 longitude (d) 2022 longitude
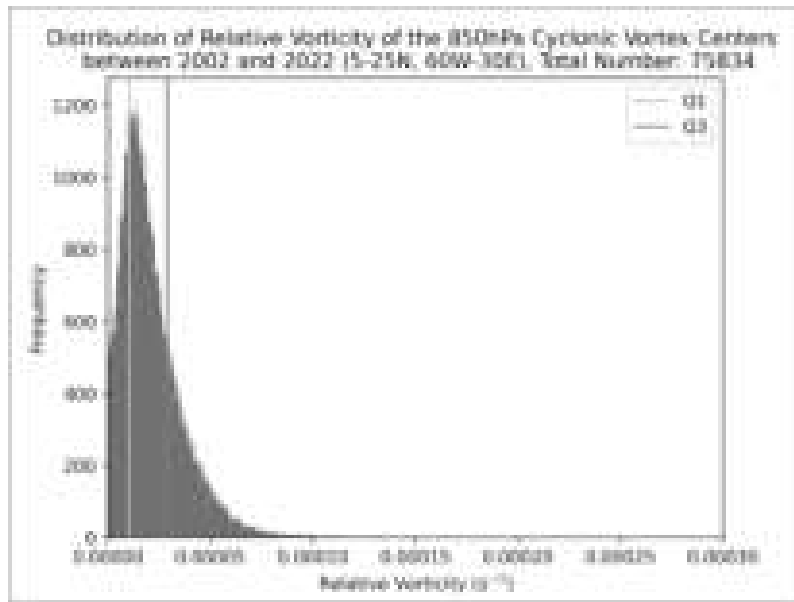
Figure 7.4: Distribution of Relative Vorticity of the 850hPa Cyclonic Vortex Centers between 2002 and 2022 within the tropical domain. The upper (Q1) and lower (Q3) quartiles have been drawn from the curve.
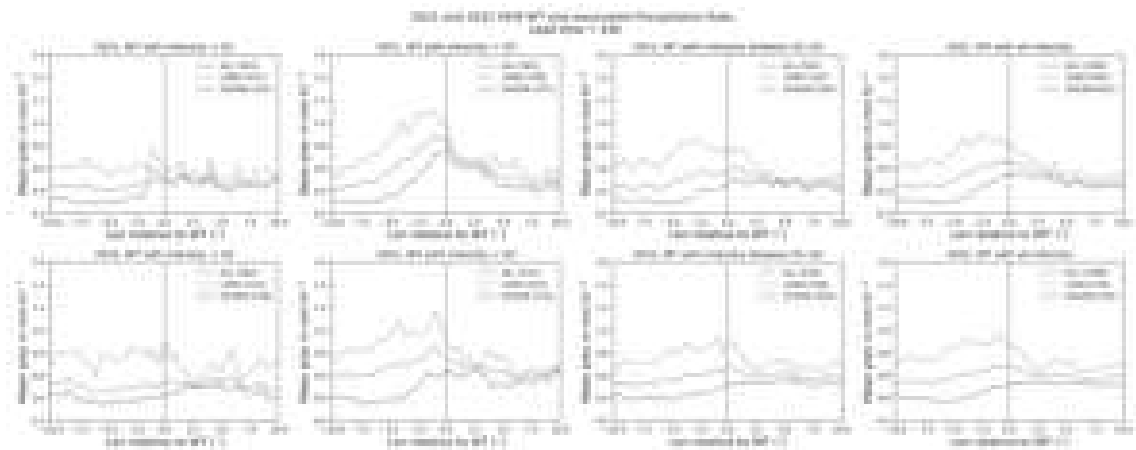
(a) Similar to Fig. 5.3, but with lead time = 24 hours
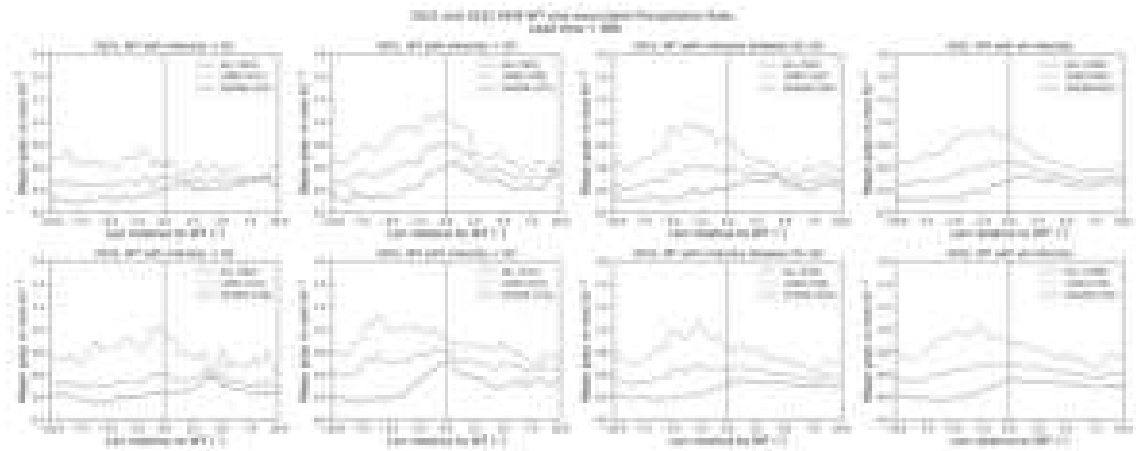
(b) Similar to Fig. 5.3, but with lead time = 48 hours

Figure 7.5: Results of the average precipitation rate aligning to WT axes composite, with lead time (a) 24h (b) 48h, similar to Fig. 5.3

Bibliography

Agudelo, P. A., C. D. Hoyos, J. A. Curry, and P. J. Webster, 2011: Probabilistic discrimination between large-scale environments of intensifying and decaying african easterly waves. *Climate dynamics*, **36**, 1379–1401.

Bechtold, P., R. Forbes, I. Sandu, S. Lang, and M. Ahlgrimm, 2020: A major moist physics upgrade for the IFS.

Becker, T., P. Bechtold, and I. Sandu, 2021: Characteristics of convective precipitation over tropical Africa in storm-resolving global simulations. *Quarterly Journal of the Royal Meteorological Society*, **147 (741)**, 4388–4407.

Belanger, J. I., M. T. Jelinek, and J. A. Curry, 2016: A climatology of easterly waves in the tropical Western Hemisphere. *Geoscience Data Journal*, **3 (2)**, 40–49.

Berry, G. J., and C. Thorncroft, 2005: Case Study of an Intense African Easterly Wave. *Monthly Weather Review*, **133 (4)**, 752–766.

Berry, G. J., and C. D. Thorncroft, 2012: African Easterly Wave Dynamics in a Mesoscale Numerical Model: The Upscale Role of Convection. *Journal of the Atmospheric Sciences*, **69 (4)**, 1267–1283.

Burpee, R. W., 1972: The origin and structure of easterly waves in the lower troposphere of north africa. *Journal of the Atmospheric Sciences*, **29 (1)**, 77–90.

Burpee, R. W., 1974: Characteristics of north african easterly waves during the summers of 1968 and 1969. *Journal of Atmospheric Sciences*, **31 (6)**, 1556–1570.

Carlson, T. N., 1969a: Some remarks on african disturbances and their progress over the tropical atlantic. *Monthly Weather Review*, **97 (10)**, 716–726.

Carlson, T. N., 1969b: Synoptic histories of three african disturbances that developed into atlantic hurricanes. *Monthly Weather Review*, **97 (3)**, 256–276.

Charney, J. G., and M. E. Stern, 1962: On the stability of internal baroclinic jets in a rotating atmosphere. *Journal of the Atmospheric Sciences*, **19 (2)**, 159–172.

Chen, C.-C., J. Richter, C. Liu, M. Moncrieff, Q. Tang, W. Lin, S. Xie, and P. J. Rasch, 2021: Effects of organized convection parameterization on the mjo and precipitation in e3smv1. part i: Mesoscale heating. *Journal of Advances in Modeling Earth Systems*, **13 (6)**, e2020MS002 401.

Cornforth, R., and Coauthors, 2017: Synoptic Systems. *Meteorology of Tropical West Africa, The Forecasters Handbook*, John Wiley & Sons, Ltd, 40–89.

Cornforth, R. J., B. J. Hoskins, and C. D. Thorncroft, 2009: The impact of moist processes on the African easterly jet-African easterly wave system. *Quarterly Journal of the Royal Meteorological Society*, **135 (641)**, 894–913.

Crook, J., C. Klein, S. Folwell, C. M. Taylor, D. J. Parker, R. Stratton, and T. Stein, 2019: Assessment of the representation of west african storm lifecycles in convection-permitting simulations. *Earth and Space Science*, **6 (5)**, 818–835.

Davis, C., B. Brown, and R. Bullock, 2006: Object-based verification of precipitation forecasts. part i: Methodology and application to mesoscale rain areas. *Monthly Weather Review*, **134 (7)**, 1772–1784.

Davis, J., P. Knippertz, and A. H. Fink, 2013: The predictability of precipitation episodes during the west african dry season. *Quarterly Journal of the Royal Meteorological Society*, **139 (673)**, 1047–1058.

Diedhiou, A., S. Janicot, A. Viltard, P. de Felice, and H. Laurent, 1999: Easterly wave regimes and associated convection over West Africa and tropical Atlantic: results from the NCEP/NCAR and ECMWF reanalyses. *Climate Dynamics*, **15 (11)**, 795–822.

Duvel, J. P., 1990: Convection over tropical africa and the atlantic ocean during northern summer. part ii: Modulation by easterly waves. *Monthly Weather Review*, **118 (9)**, 1855–1868.

Elless, T. J., and R. D. Torn, 2018: African Easterly Wave Forecast Verification and Its Relation to Convective Errors within the ECMWF Ensemble Prediction System. *Weather and Forecasting*, **33 (2)**, 461–477.

Elless, T. J., and R. D. Torn, 2019: Investigating the Factors That Contribute to African Easterly Wave Intensity Forecast Uncertainty in the ECMWF Ensemble Prediction System. *Monthly Weather Review*, **147 (5)**, 1679–1698.

Emanuel, K. A., J. David Neelin, and C. S. Bretherton, 1994: On large-scale circulations in convecting atmospheres. *Quarterly Journal of the Royal Meteorological Society*, **120 (519)**, 1111–1143.

Fink, A., D. Vincent, and V. Ermert, 2006: Rainfall types in the west african sudanian zone during the summer monsoon 2002. *Monthly weather review*, **134 (8)**, 2143–2164.

Fink, A. H., and A. Reiner, 2003: Spatiotemporal variability of the relation between African Easterly Waves and West African Squall Lines in 1998 and 1999. *Journal of Geophysical Research*, **108 (D11)**.

Fink, A. H., D. G. Vincent, P. M. Reiner, and P. Speth, 2004: Mean State and Wave Disturbances during Phases I, II, and III of GATE Based on ERA-40. *Monthly Weather Review*, **132 (7)**,

1661–1683.

Fink, A. H., and Coauthors, 2017: Mean Climate and Seasonal Cycle. *Meteorology of Tropical West Africa: The Forecasters Handbook*, John Wiley & Sons, Ltd, 1–39.

Fischer, C., A. H. Fink, E. Schömer, M. Rautenhaus, and M. Riemer, 2023: An objective identification technique for potential vorticity structures associated with african easterly waves. *Geoscientific Model Development Discussions*, **2023**, 1–23, https://doi.org/10.5194/gmd-2023-218, URL https://gmd.copernicus.org/preprints/gmd-2023-218/.

Freitas, S. R., W. M. Putman, N. P. Arnold, D. K. Adams, and G. A. Grell, 2020: Cascading toward a kilometer-scale gcm: Impacts of a scale-aware convection parameterization in the goddard earth observing system gcm. *Geophysical Research Letters*, **47 (17)**, e2020GL087 682.

Glickman, T., and Z. Walter, 2000: Glossary of meteorology. American Meteorological Soc.

Gu, G., R. F. Adler, G. J. Huffman, and S. Curtis, 2004: African easterly waves and their association with precipitation: AFRICAN EASTERLY WAVES AND PRECIPITATION. *Journal of Geophysical Research: Atmospheres*, **109 (D4)**.

Hodges, K. I., B. J. Hoskins, J. Boyle, and C. Thorncroft, 2003: A comparison of recent reanalysis datasets using objective feature tracking: Storm tracks and tropical easterly waves. *Monthly Weather Review*, **131 (9)**, 2012–2037.

Hohenegger, C., L. Kornblueh, D. Klocke, T. Becker, G. Cioni, J. F. Engels, U. Schulzweida, and B. Stevens, 2020: Climate statistics in global simulations of the atmosphere, from 80 to 2.5 km grid spacing. *Journal of the Meteorological Society of Japan. Ser. II*, **98 (1)**, 73–91.

Hopsch, S. B., C. D. Thorncroft, K. Hodges, and A. Aiyyer, 2007: West african storm tracks and their relationship to atlantic tropical cyclones. *Journal of Climate*, **20 (11)**, 2468–2483.

Hopsch, S. B., C. D. Thorncroft, and K. R. Tyle, 2010: Analysis of african easterly wave structures and their role in influencing tropical cyclogenesis. *Monthly Weather Review*, **138 (4)**, 1399–1419.

Hsieh, J.-S., and K. H. Cook, 2007: A Study of the Energetics of African Easterly Waves Using a Regional Climate Model. *Journal of the Atmospheric Sciences*, **64 (2)**, 421–440.

Huffman, G. J., D. T. Bolvin, and E. J. Nelkin, 2015: Day 1 imerg final run release notes. *NASA/GSFC: Greenbelt, MD, USA*, 9.

Janiga, M. A., and C. D. Thorncroft, 2013: Regional differences in the kinematic and thermodynamic structure of African easterly waves. *Quarterly Journal of the Royal Meteorological Society*, **139 (675)**, 1598–1614.

Janiga, M. A., and C. D. Thorncroft, 2016: The Influence of African Easterly Waves on Convection over Tropical Africa and the East Atlantic. *Monthly Weather Review*, **144 (1)**, 171–192.

Kiladis, G. N., C. D. Thorncroft, and N. M. J. Hall, 2006: Three-Dimensional Structure and Dynamics of African Easterly Waves. Part I: Observations. *Journal of the Atmospheric Sciences*, **63 (9)**, 2212–2230.

Klein, C., F. Nkrumah, C. M. Taylor, and E. A. Adefisan, 2021: Seasonality and trends of drivers of mesoscale convective systems in southern west africa. *Journal of Climate*, **34 (1)**, 71–87.

Knippertz, P., and Coauthors, 2017: A meteorological and chemical overview of the dacciwa field campaign in west africa in june–july 2016. *Atmospheric Chemistry and Physics*, **17 (17)**, 10 893–10 918.

Lafore, J. P., and Coauthors, 2017: Deep Convection. *Meteorology of Tropical West Africa, The Forecasters Handbook*, John Wiley & Sons, Ltd, 90–129.

Limbach, S., E. Schömer, and H. Wernli, 2012: Detection, tracking and event localization of jet stream features in 4-D atmospheric data. *Geoscientific Model Development*, **5 (2)**, 457–470.

Lorenz, E. N., 1969: The predictability of a flow which possesses many scales of motion. *Tellus*, **21 (3)**, 289–307.

Maranan, M., A. H. Fink, and P. Knippertz, 2018: Rainfall types over southern West Africa: Objective identification, climatology and synoptic environment. *Quarterly Journal of the Royal Meteorological Society*, **144 (714)**, 1628–1648.

Markowski, P., and Y. Richardson, 2011: *Mesoscale meteorology in midlatitudes*. John Wiley & Sons.

Mathon, V., H. Laurent, and T. Lebel, 2002: Mesoscale convective system rainfall in the sahel. *Journal of Applied Meteorology and Climatology*, **41 (11)**, 1081–1092.

Mekonnen, A., C. D. Thorncroft, and A. R. Aiyyer, 2006: Analysis of Convection and Its Association with African Easterly Waves. *Journal of Climate*, **19 (20)**, 5405–5421.

Moncrieff, M. W., C. Liu, and P. Bogenschutz, 2017: Simulation, Modeling, and Dynamically Based Parameterization of Organized Tropical Convection for Global Climate Models. *Journal of the Atmospheric Sciences*, **74 (5)**, 1363–1380.

Nicholson, S. E., 2018: The itcz and the seasonal cycle over equatorial africa. *Bulletin of the American Meteorological Society*, **99 (2)**, 337–348.

Pante, G., and P. Knippertz, 2019: Resolving Sahelian thunderstorms improves mid-latitude weather forecasts. *Nature Communications*, **10 (1)**, 3487.

Parker, D. J., C. D. Thorncroft, R. R. Burton, and A. Diongue-Niang, 2005: Analysis of the african easterly jet, using aircraft observations from the jet2000 experiment. *Quarterly Journal of the Royal Meteorological Society: A journal of the atmospheric sciences, applied meteorology and physical oceanography*, **131 (608)**, 1461–1482.

Pytharoulis, I., and C. Thorncroft, 1999: The low-level structure of african easterly waves in 1995. *Monthly Weather Review*, **127 (10)**, 2266–2280.

Reed, R., E. Klinker, and A. Hollingsworth, 1988: The structure and characteristics of african easterly wave disturbances as determined from the ecmwf operational analysis/forecast system. *Meteorology and Atmospheric Physics*, **38**, 22–33.

Reed, R. J., D. C. Norquist, and E. E. Recker, 1977: The Structure and Properties of African Wave Disturbances as Observed During Phase III of GATE. *Monthly Weather Review*, **105 (3)**, 317–333.

Roehrig, R., D. Bouniol, F. Guichard, F. Hourdin, and J.-L. Redelsperger, 2013: The present and future of the west african monsoon: A process-oriented assessment of cmip5 simulations along the amma transect. *Journal of Climate*, **26 (17)**, 6471–6505.

Russell, J. O. H., and A. Aiyyer, 2020: The Potential Vorticity Structure and Dynamics of African Easterly Waves. *Journal of the Atmospheric Sciences*, **77 (3)**, 871–890.

Satoh, M., A. T. Noda, T. Seiki, Y.-W. Chen, C. Kodama, Y. Yamada, N. Kuba, and Y. Sato, 2018: Toward reduction of the uncertainties in climate sensitivity due to cloud processes using a global non-hydrostatic atmospheric model. *Progress in Earth and Planetary Science*, **5 (1)**, 1–29.

Schlueter, A., A. H. Fink, P. Knippertz, and P. Vogel, 2019: A systematic comparison of tropical waves over northern africa. part i: Influence on rainfall. *Journal of Climate*, **32 (5)**, 1501–1523.

Stephens, G. L., and Coauthors, 2010: Dreary state of precipitation in global models. *Journal of Geophysical Research: Atmospheres*, **115 (D24)**.

Stevens, B., and Coauthors, 2019: Dyamond: the dynamics of the atmospheric general circulation modeled on non-hydrostatic domains. *Progress in Earth and Planetary Science*, **6 (1)**, 1–17.

Thorncroft, C., and K. Hodges, 2001: African Easterly Wave Variability and Its Relationship to Atlantic Tropical Cyclone Activity. *Journal of Climate*, **14 (6)**, 1166–1179.

Thorncroft, C., and B. Hoskins, 1994: An idealized study of african easterly waves. i: A linear view. *Quarterly Journal of the Royal Meteorological Society*, **120 (518)**, 953–982.

Thorncroft, C. D., N. M. J. Hall, and G. N. Kiladis, 2008: Three-Dimensional Structure and Dynamics of African Easterly Waves. Part III: Genesis. *Journal of the Atmospheric Sciences*, **65 (11)**, 3596–3607.

Torn, R. D., 2010: Ensemble-Based Sensitivity Analysis Applied to African Easterly Waves. *Weather and Forecasting*, **25 (1)**, 61–78.

Vogel, P., P. Knippertz, A. H. Fink, A. Schlueter, and T. Gneiting, 2018: Skill of Global Raw and Postprocessed Ensemble Predictions of Rainfall over Northern Tropical Africa. *Weather and Forecasting*, **33 (2)**, 369–388.

Wedi, N. P., and Coauthors, 2020: A baseline for global weather and climate simulations at 1 km resolution. *Journal of Advances in Modeling Earth Systems*, **12 (11)**, e2020MS002 192.

Wernli, H., M. Paulat, M. Hagen, and C. Frei, 2008: Sal—a novel quality measure for the verification of quantitative precipitation forecasts. *Monthly Weather Review*, **136 (11)**, 4470–4487.

Acknowledgments

Doing research seems to be an overwhelming task to me at the beginning when there might be a lot of unforeseeable circumstances. It requires the researcher to navigate a puzzle of complex concepts, which is important for comprehending a lot of literature so as to perform a sound scientific analysis. While this journey can sometimes make me feel daunting, I believe my thesis year has been a precious opportunity for me to practise my skills in research. At this point, I am deeply thankful for all the helpful advice from my esteemed research supervisors for their support, guidance, and insightful feedback throughout my research process.

First of all, I am grateful to Prof. Andreas H. Fink for his invaluable mentorship in my master thesis project. Prof. Fink's expertise has not only given me with a comprehensive understanding of the complexities of research on African Easterly Waves dynamics but has also suggested me with many practical strategies to overcome the challenges inherent in academic writing. For example, the way of doing a scientific writing is not directly like being an engineer writing a documentation. It is important to practise how to integrate manifold concepts throughout the whole piece of writing. This is helpful in shaping my problem-solving approach, and also appreciating the growth of State of the Art in this research area. Other than that, I have been gaining a lot of inspirations from Prof. Peter Knippertz every time through our conversations. He has always been encouraging so that I can confidently raise my questions up and also express my ideas in the working group. This is very useful in fostering an effective and progressive workplace communication among colleagues. This assures my aspiration to further enhance this communication skill and conviction to the colleagues I am going to meet in my future career.

Furthermore, I would like to express my sincere appreciation to Dr. Marlon Maranan for his invaluable advice and steadfast support in maintaining momentum throughout my research process all the way. Marlon's guidance has been essential in keeping my progress focused and on track, particularly during moments of uncertainty or complexity. There have been multiple long discussions with Marlon at the institute. These sessions have not only taught me to express my thoughts about the research findings and better interpret them, but also learn how to critically analyze the results and underlying challenges in depths. In addition, I would like to extend my gratitude to Christoph Fischer for his generous assistance in data handling techniques. This project is an extension from Christoph's PhD work and I have received a lot of help from his contribution on the wavetrough and vortex datasets. He has always been supportive whenever I had questions to ask him or some technicalities that I was unsure of.

As I reflect on the progress made thus far, I am humbled by the collective contributions of scholars, including my supervisors, in the field of tropical meteorology. I have truly enjoyed different rounds

of interactions with Prof. Fink, Prof. Knippertz, Marlon and all other colleagues in my working group. It has been inspiring that I can witness how different PhD students in my working group have made it through the strenuous journey in finishing their individual big research projects, and listen to their sharing at their final stages. Their pioneering efforts, particularly investigating the intricate patterns embedded within tropical climatic variability, serve as a constant source of driving force.

All in all, I am immensely grateful for the mentorship, guidance, and support to me by everyone who has supported me throughout my project work. As I proceed to the next phase of my journey, I am confident that the lessons learned and insights gained under their supervision will continue to grow in further more applications, which lead me to the new horizons of discovery and innovation in the meteorology and climate research areas.

Erklärung

Ich versichere wahrheitsgemäß, die Arbeit selbstständig verfasst, alle benutzten Hilfsmittel vollständig und genau angegeben und alles kenntlich gemacht zu haben, was aus Arbeiten anderer unverändert oder mit Abänderungen entnommen wurde sowie die Satzung des KIT zur Sicherung guter wissenschaftlicher Praxis in der jeweils gültigen Fassung beachtet zu haben.

Karlsruhe, den 27.03.2024

Chun Cheong Nicolas Lo